

University of Windsor

## Scholarship at UWindor

---

Electronic Theses and Dissertations

Theses, Dissertations, and Major Papers

---

2014

# Weld Distortion Prediction With Virtual Analysis For Practical Applications

Francesca Folchi  
*University of Windsor*

Follow this and additional works at: <https://scholar.uwindsor.ca/etd>

---

### Recommended Citation

Folchi, Francesca, "Weld Distortion Prediction With Virtual Analysis For Practical Applications" (2014). *Electronic Theses and Dissertations*. 5229.  
<https://scholar.uwindsor.ca/etd/5229>

This online database contains the full-text of PhD dissertations and Masters' theses of University of Windsor students from 1954 forward. These documents are made available for personal study and research purposes only, in accordance with the Canadian Copyright Act and the Creative Commons license—CC BY-NC-ND (Attribution, Non-Commercial, No Derivative Works). Under this license, works must always be attributed to the copyright holder (original author), cannot be used for any commercial purposes, and may not be altered. Any other use would require the permission of the copyright holder. Students may inquire about withdrawing their dissertation and/or thesis from this database. For additional inquiries, please contact the repository administrator via email ([scholarship@uwindsor.ca](mailto:scholarship@uwindsor.ca)) or by telephone at 519-253-3000ext. 3208.

# WELD DISTORTION PREDICTION WITH VIRTUAL ANALYSIS FOR PRACTICAL APPLICATIONS

By

**FRANCESCA FOLCHI**

A Thesis  
Submitted to the Faculty of Graduate Studies  
through the Department of Mechanical, Automotive and Material Engineering  
in Partial Fulfillment of the Requirements for  
the Degree of Master of Applied Science  
at the University of Windsor

Windsor, Ontario, Canada

2014

© 2014 Francesca Folchi

# WELD DISTORTION PREDICTION WITH VIRTUAL ANALYSIS FOR PRACTICAL APPLICATIONS

by

**Francesca Folchi**

APPROVED BY:

---

R. Bowers  
Department of Mechanical, Automotive & Materials Engineering

---

D. Ting  
Department of Mechanical, Automotive & Materials Engineering

---

V. Stoilov, Advisor  
Department of Mechanical, Automotive & Materials Engineering

September 3, 2014

## **DECLARATION OF ORIGINALITY**

I hereby certify that I am the sole author of this thesis and that no part of this thesis has been published or submitted for publication.

I certify that, to the best of my knowledge, my thesis does not infringe upon anyone's copyright nor violate any proprietary rights and that any ideas, techniques, quotations, or any other material from the work of other people included in my thesis, published or otherwise, are fully acknowledged in accordance with the standard referencing practices. Furthermore, to the extent that I have included copyrighted material that surpasses the bounds of fair dealing within the meaning of the Canada Copyright Act, I certify that I have obtained a written permission from the copyright owner(s) to include such material(s) in my thesis and have included copies of such copyright clearances to my appendix.

I declare that this is a true copy of my thesis, including any final revisions, as approved by my thesis committee and the Graduate Studies office, and that this thesis has not been submitted for a higher degree to any other University or Institution.

## **ABSTRACT**

The reduction in time and facilities involved in the partial elimination or mitigation of welding distortion is one of the key points for manufacturers. Welding distortion is influenced by the sequence and position of joints, the clamping configuration and the design of the assembly. For large complex assemblies, the range of these options may be large. Therefore the use of numerical simulations at an early stage of the product development process is valuable to enable a wide range of these factors to be explored with the aim of minimizing welding distortions before production commences. This thesis investigates two techniques for simulation of welding distortions based on shrinkage analysis and transient analysis. Both techniques are evaluated for an automotive assembly. The shrinkage simulations were built and solved using the Weld Planner, whereas the transient simulations were solved with Sysweld. The rapid simulation speed enabled a wide range of welding materials and clamping positions to be explored, leading to recommendations for reduction of the distortions. The solution times were found to be significantly lower for the shrinkage analysis than the transient analysis.

**DEDICATION**

*To Nonna Mafalda, I miss you.*

## ACKNOWLEDGEMENTS

First of all, I would like to thank my advisors Dr. Vesselin Stoilov and Prof. Giovanni Belingardi for their useful suggestions and remarks through the difficult thesis process. I would like also to thank my committee members, Dr. Randy Bowers and Dr. David Ting.

I would like to express my appreciation to my Chrysler tutor Greg Medler and my Chrysler supervisor Mohammed Malik for the assistance provided. A special thank goes to Jeffrey Stewart from the Chrysler Welding group for the big help provided in the weld lab.

It has been a year full of emotions and for this reason I would like to thank all the amazing people that helped me through this journey:

First of all, my friends Giuseppe, Marco, Federico, the two Luca, Ashley, Tom, Kyle, Felicia, Steven, Antonio and Kathleen for the great times spent together here in Windsor.

All my Italian friends, for reminding me that friendship is stronger than distance.

My best friend, sister and “snowflake”, Marianna, for the amazing support that she gave me through these years, she has always been beside me in every adventure.

My boyfriend and best friend, Nicola, for standing by my side in every choice I made.

My grandmother and my uncles, in particular Zia Patrizia for her unconditional support.

I want to reserve the most important thank to my parents, Enzo and Flora, for believing in me and for being my guide.

Last but not least, I would like to thank my brother, Stefano, for being one of the most important people in my life. Even though we spent years far away, we always found a way to help each other. I love you.

## TABLE OF CONTENTS

DECLARATION OF ORIGINALITY .....	iii
ABSTRACT.....	iv
DEDICATION.....	v
ACKNOWLEDGEMENTS.....	vi
LIST OF TABLES.....	x
LIST OF FIGURES .....	xii
LIST OF APPENDICES.....	xvi
LIST OF ABBREVIATIONS/SYMBOLS.....	xvii
NOMENCLATURE .....	xviii
CHAPTER 1 INTRODUCTION AND LITERATURE REVIEW .....	1
1.1 Introduction .....	1
1.2 Literature Review.....	2
1.2.1 Numerical simulation approach .....	2
1.2.2 Statistical approaches.....	13
1.2.3 Empirical approach.....	15
1.2.4 Industrial relevance for welding distortion prediction.....	16
CHAPTER 2 THEORY BEHIND WELD DISTORTION AND NUMERICAL APPROACH.....	18
2.1 Theory behind weld distortion .....	18
2.1.1 Fundamentals and general technology of welding.....	18
2.1.2 Complex coupling in welding modeling.....	24
2.1.3 Residual stresses and distortions calculations.....	34
2.2 Numerical approach .....	38



CHAPTER 3 EXPERIMENTAL SETUP .....	41
3.1 Definition of geometry and welding process parameters.....	41
3.2 Distortion measurement .....	44
3.3 Results and discussion.....	45
CHAPTER 4 NUMERICAL SIMULATION OF ARC WELDING.....	49
4.1 Model development for Transient analysis-SYSWELD .....	50
4.2 Model development for Shrinkage method-WELD PLANNER.....	53
4.3 Results and discussions for transient analysis-SYSWELD .....	55
4.4 Results and discussion for shrinkage method- WELD PLANNER .....	66
4.5 Validation of transient analysis and shrinkage method with data from the literature review.....	68
4.5.1 Model development and results for transient analysis-SYSWELD..	69
4.5.2 Model development and results for shrinkage method - WELD PLANNER	72
4.5.3 Comparison between transient and shrinkage analysis approach for the validation test.....	76
CHAPTER 5 COMPARISON BETWEEN NUMERICAL RESULTS AND EXPERIMENTAL RESULTS.....	78
5.1 Comparison between transient analysis results and experimental results	78
5.2 Comparison between shrinkage method and experimental results .....	87
CHAPTER 6 OPTIMIZATION WITH WELD PLANNER .....	88
CHAPTER 7 CONCLUSIONS AND RECOMMENDATIONS .....	95
7.1 Conclusions .....	95
7.2 Future work and recommendations .....	96
APPENDICES .....	98
Appendix A - A guide to welding process in Sysweld Environment.....	98

Appendix B - A guide to welding process in WELD PLANNER .....	106
Appendix C- Wire filler properties .....	110
REFERENCES .....	111
VITA AUCTORIS .....	117

## LIST OF TABLES

Table 1.1- Comparison between the common modeling-optimization techniques [26]...	15
Table 3.1- Coupon dimensions .....	41
Table 3.2- Requirements for Chemical Composition(% by Mass) of MS 67.....	42
Table 3.3- Minimum Mechanical properties of mild steels in transverse direction- Chrysler standard for MS 67.....	42
Table 3.4- Minimum Mechanical Properties of high strength steel MS 264 05 XK in transverse direction .....	42
Table 3.5- Welding parameters.....	42
Table 3.6- Materials and clamping condition used for the six tests.....	43
Table 3.7-Distance results [mm] in experimental tests.....	46
Table 3.8-Displacement [mm] in experimental tests .....	46
Table 4.1- Chemical composition (%by mass) of low carbon steel S355J2G3-EN 10025 [21].....	51
Table 4.2-Minimum Mechanical Properties of S355J2G3 (EN 10025) or st52(DIN 17100) [21] [57].....	51
Table 4.3-Chemical composition (% by mass) for plain carbon steel DC 04-AISI 1006 [58].....	51
Table 4.4-Minimum Mechanical properties of DC 04-AISI 1006 .....	51
Table 4.5- Heat source parameters used in the simulations.....	52
Table 4.6-Simulation measurement [mm] and displacement [mm] results for T-joint Test #1.....	56
Table 4.7- Simulation measurement [mm] and displacement [mm] results for T-joint Test #2.....	57
Table 4.8- Simulation measurement [mm] and displacement [mm] results for T-joint Test #3.....	59
Table 4.9- Simulation measurement [mm] and displacement [mm] results for T-joint Test #4.....	60
Table 4.10- Simulation measurement [mm] and displacement [mm] results for T-joint Test #5.....	62
Table 4.11- Simulation measurement [mm] and displacement [mm] results for T-joint Test #6.....	63
Table 4.12-Von Mises stress [MPa] among the six tests and relative average value and standard deviation .....	66
Table 4.13-Welding parameters used in Sulamain et al. research .....	68
Table 4.14-Experimental results of the validation test .....	69
Table 4.15- Heat source parameters used in the simulation for validation.....	70
Table 4.16-Comparison of Angular distortion results between simulation and experiment for t-joint validation test.....	72

Table 4.17- Comparison of Angular distortion results [mm] between simulation and experiment for t-joint validation case (WELD PLANNER).....	75
Table 4.18- Comparison between transient analysis results and shrinkage analysis results for t-joint for the validation test.....	76
Table 5.1- Displacement results and error between simulation and experimental results for Test #1.....	78
Table 5.2- Average errors along the lines for Test #1.....	78
Table 5.3-- Displacement results and error between simulation and experimental results for Test #2-uncontrolled condition.....	80
Table 5.4- Average errors along the lines for Test #2.....	80
Table 5.5-- Displacement results and error between simulation and experimental results for Test #3-uncontrolled condition.....	81
Table 5.6- Average errors along the lines for Test #3.....	81
Table 5.7-- Displacement results and error between simulation and experimental results for Test #4-uncontrolled condition.....	82
Table 5.8- Average errors along the lines for Test #4.....	83
Table 5.9-- Displacement results and error between simulation and experimental results for Test #5-uncontrolled condition.....	84
Table 5.10- Average errors along the lines for Test #5.....	84
Table 5.11-- Displacement results and error between simulation and experimental results for Test #6-uncontrolled condition.....	85
Table 5.12- Average errors along the lines for Test #6.....	86
Table 6.1-Material combination for Case #1 and Case #2.....	88
Table 6.2-Influence of thickness on the maximum displacement in case of arc bead width of 5 mm.....	90
Table 6.3- Influence of thickness on the maximum displacement in case of arc bead width of 6 mm.....	90
Table 6.4- Influence of thickness on the maximum displacement in case of arc bead width of 6.8 mm.....	90
Table 6.5-Maximum displacement results for base clamping configuration and configuration A.....	93
Table 6.6-Maximum displacement results for base clamping configuration and configuration A.....	94

## LIST OF FIGURES

Figure 1.1- Longitudinal shrinkage in 2.5mm and 3 mm thick plate [4].....	3
Figure 1.2- Longitudinal shrinkage in 2.5mm and 3 mm thick plate [4].....	4
Figure 1.3- Example of optimization [13] .....	7
Figure 1.4-Full transient analysis (displacements) [20].....	9
Figure 1.5-Shrinkage analysis (displacement) [20] .....	10
Figure 1.6-Comparison of distortion in the transient model and in the shrinkage model [12].....	11
Figure 1.7-Example of the procedure for setting up welding models: (a) shrinkage analysis; (b) transient analysis [12].....	12
Figure 1.8-Developed ANN architecture for the residual stress prediction [24].....	14
Figure 1.9- Share of lightweight materials in aviation, wind and automotive field [30]..	17
Figure 1.10-Illustration of door hinge assembly [33] .....	17
Figure 2.1- Principal zones in a cross section of a welded joint [35] .....	19
Figure 2.2- Basic arc welding configuration [36].....	19
Figure 2.3- Gas metal arc welding (GMAW) basic configuration [35].....	21
Figure 2.4-Gas tungsten arc welding (GTAW) [35].....	22
Figure 2.5-(a) Butt joint, (b)Corner joint and (c) Lap joint [35].....	23
Figure 2.6- (d) Tee joint and (e) Edge joint [35] .....	23
Figure 2.7- Different types of welding distortion [11] .....	25
Figure 2.8-Coupling welding process [39] .....	26
Figure 2.9- Double ellipsoid heat source [44] .....	27
Figure 2.10- Variation of material properties with the temperature for 5052-H32 aluminum alloy (a) thermal properties, (b) mechanical properties [47] .....	30
Figure 2.11- Body centered cubic crystal structure [49]- $\alpha$ phase .....	31
Figure 2.12-Face centered cubic crystal structure [49]- $\gamma$ phase .....	32
Figure 2.13- HAZ and equilibrium diagram [50] .....	32
Figure 2.14-Example of visual appearance of hydrogen cracking [51].....	33
Figure 2.15- Strain gauge rosette [52] .....	35
Figure 2.16- Bonded metallic strain gauge [56] .....	38
Figure 2.17-Models of shrinkage forces and moments for butt joint (left) and T-Joint (right) [21].....	40
Figure 3.1- Tee joint geometry- measurements in mm.....	41
Figure 3.2-T-joint setup .....	44
Figure 3.3- Position of 12 Points on Coupon#3-Top view .....	45
Figure 3.4-Position of the 6 points on Coupon #1 and 12 distances measured (in red) ...	45
Figure 3.5-Experimental displacement [mm] for Test #1 and Test #2.....	47
Figure 3.6- Experimental displacement [mm] for Test #3 and Test #4 .....	48
Figure 3.7- Experimental displacement [mm] for Test #5 and Test .....	48
Figure 4.1- Workflow of the research.....	49

Figure 4.2- T-joint mesh for transient analysis .....	50
Figure 4.3- Software section (left) and real section (right) of the T-joint for transient analysis.....	50
Figure 4.4- 3D skin for cooling condition .....	52
Figure 4.5-Position of the clamps for simulation Test#3 and Test #4 .....	53
Figure 4.6- T-joint mesh for controlled clamping condition .....	54
Figure 4.7- T-joint filler geometry in WELD PLANNER.....	54
Figure 4.8-Clamping condition for Test #3 WELD PLANNER .....	55
Figure 4.9- Weld Plan T-joint for simulation Test #3 and Test#4 in WELD PLANNER	55
Figure 4.10-Displacement [mm] trend in z-direction obtained with transient analysis for T-joint Test #1.....	56
Figure 4.11-Von Mises stress [MPa] trend obtained with transient analysis for T-joint Test #1.....	57
Figure 4.12- Displacement [mm] trend in z-direction obtained with transient analysis for T-joint Test #2.....	58
Figure 4.13- Von Mises Stress [MPa] trend obtained with transient analysis for T-joint Test #2.....	58
Figure 4.14- Displacement [mm] trend in z-direction obtained with transient analysis for T-joint Test #3.....	59
Figure 4.15- Von Mises Stress [MPa] trend obtained with transient analysis for T-joint Test #3.....	60
Figure 4.16- Displacement [mm] trend in z-direction obtained with transient analysis for T-joint Test #4.....	61
Figure 4.17- Von Mises Stress [MPa] trend obtained with transient analysis for T-joint Test #4.....	61
Figure 4.18- Displacement [mm] trend in z-direction obtained with transient analysis for T-joint Test #5.....	62
Figure 4.19- Von Mises Stress [MPa] trend obtained with transient analysis for T-joint Test #5.....	63
Figure 4.20- Displacement [mm] trend in z-direction obtained with transient analysis for T-joint Test #6.....	64
Figure 4.21- Von Mises Stress [MPa] trend obtained with transient analysis for T-joint Test #6.....	64
Figure 4.22-Comparison between simulation displacements between Test #1 and Test #2 .....	65
Figure 4.23- Comparison between simulation displacements between Test #3 and Test #4 .....	65
Figure 4.24- Comparison between simulation displacements between Test #5 and Test #6 .....	66
Figure 4.25- Distortion [mm] in z-direction [mm] for Test #1 and Test #2 .....	67

Figure 4.26- Distortion [mm] in z-direction [mm] for Test #3 and Test #4 .....	67
Figure 4.27- Distortion [mm] in z-direction [mm] for Test #5 and Test #6 .....	67
Figure 4.28- T-joint clamping condition [21] .....	69
Figure 4.29- T-joint mesh for the t-joint validation test .....	70
Figure 4.30-Software section (left) and real section (right) of the T-joint validation test	70
Figure 4.31- Displacement [mm] trend in z-direction for t-joint validation test at 3600s (view of the 1 <sup>st</sup> welded side) .....	71
Figure 4.32- Displacement [mm] trend in z-direction for t-joint validation test at 3600s (view of the 2 <sup>nd</sup> welded side) .....	71
Figure 4.33- Von Mises stress [MPa] for T-joint validation test at 3600s .....	72
Figure 4.34-T-joint mesh validation test.....	73
Figure 4.35-T-joint filler geometry-validation test.....	73
Figure 4.36-CLAMP_01 and CLAMP_02 position.....	74
Figure 4.37-Weld Plan t-joint validation test.....	74
Figure 4.38-Displacement [mm] in z-direction t-joint validation test(WELD PLANNER) .....	74
Figure 4.39- Magnification 10x of the deformed T-joint validation case (WELD PLANNER).....	75
Figure 4.40- Qualitative distortion trend comparison between transient analysis (left) and shrinkage analysis (right) for the first welded side .....	77
Figure 4.41- Qualitative distortion trend comparison between transient analysis (left) and shrinkage analysis (right) for the second welded side .....	77
Figure 5.1- Displacements T-joint Test#1 for uncontrolled clamping condition .....	79
Figure 5.2- Displacements T-joint Test#2 for uncontrolled clamping condition .....	80
Figure 5.3- Displacements T-joint Test#3 for uncontrolled clamping condition .....	82
Figure 5.4- Displacements T-joint Test#4 for uncontrolled clamping condition .....	83
Figure 5.5 -Displacements T-joint Test#5 for uncontrolled clamping condition .....	85
Figure 5.6- Displacements T-joint Test#6 for uncontrolled clamping condition .....	86
Figure 5.7-Example of distance for transient analysis model (left) and shrinkage analysis model (right) .....	87
Figure 6.1-Geometry and dimensions of the T-joint used for the optimization .....	88
Figure 6.2-Base Clamping configuration for both Case #1 and Case #2.....	89
Figure 6.3-Different arc bead widths used in the simulations .....	89
Figure 6.4-Influence of different arc bead width on Max Displacement.....	91
Figure 6.5-Influence of different material thicknesses on maximum displacement.....	92
Figure 6.6- Difference between base clamping configuration and clamping configuration A.....	93
Figure 6.7- Difference between base clamping configuration and clamping configuration B .....	94
Figure 8.1-Example of Sysweld Workflow [59].....	98

Figure 8.2-Example of Step1-Project description.....	99
Figure 8.3-Different types of welding processes included in Welding Advisor.....	100
Figure 8.4- Trajectory and reference path using for the moving heat source .....	101
Figure 8.5-Parameters require for the welding process (Step 4) .....	101
Figure 8.6- Penetration, width and length of the heat source .....	102
Figure 8.7-Example of cooling condition (Step 5) .....	102
Figure 8.8-Example of Clamping Condition (Step 6).....	103
Figure 8.9-Example of Step 7 and Step 8 .....	103
Figure 8.10-Example of Solution Parameter (Step 9).....	104
Figure 8.11-Contours definition.....	105
Figure 8.12-Weld Planner workflow [60].....	106
Figure 8.13-Example of material database in Weld Planner .....	107
Figure 8.14-Example of weld parameters in Weld Planner .....	107
Figure 8.15-Example of clamping definition in Weld Planner .....	108
Figure 8.16-Example of weld plan definition in Weld Planner .....	108
Figure 8.17- Result analysis panel in Weld Planner .....	109



## LIST OF APPENDICES

Appendix A - A guide to welding process in Sysweld Environment .....	98
Appendix B - A guide to welding process in WELD PLANNER.....	106
Appendix C- Wire filler properties.....	110

## LIST OF ABBREVIATIONS/SYMBOLS

ANN	Artificial Neural Network
AW	Arc Welding
DOE	Design of Experiment
EGW	Electro-gas Welding
EW	End of Welding
FCAW	Flux-Cored Arc Welding
FEM	Finite Element Method
GA	Genetic Algorithm,
GMAW	Gas Metal Arc Welding
GTAW	Gas Tungsten Arc Welding
HAZ	Heat Affected Zone
PAW	Plasma Arc Welding
RSM	Response Surface Methodology
SAW	Submerged Arc Welding
SMAW	Shielded Metal Arc Welding
SW	Start of Welding

## NOMENCLATURE

$\bar{p}_2$	Phase proportion after an infinite time at temperature T
$h_c$	Heat transfer coefficient
$A_W$	Cross sectional area
$B_i$	Sum of the body forces
$E_h$	Heat energy per unit length
$H'$	Material strain hardening
$R_a$	Arc resistance
$T_{ref}$	Reference temperature
$T_s$	Surface temperature
$T_s$	Ambient temperature
$V_H$	Volume of the heat source
$c_p$	Specific heat
$f_f$	Fraction of heat deposited in the front
$f_r$	Fraction of heat deposited in the rear
$n_d$	Number of divisions in the welding
$\bar{p}$	Phase proportion obtained at an infinitely low temperature
$q_{cond}$	Conduction heat
$q_{conv}$	Convective heat
$q_f$	Front heat flow
$q_i$	Rate of internal heat generation
$q_r$	Rear heat flow
$q_{rad}$	Radiation heat
$v_w$	Welding speed
$\delta_T$	Transverse shrinkage
$\varepsilon_0$	Emissivity
$\varepsilon_e$	Elastic strain vector
$\varepsilon_p$	Plastic strain vector
$\varepsilon_t$	Thermal strain vector

$\sigma_0$	Stefan-Boltzman constant
$\sigma_L$	Longitudinal residual stress
$\sigma_T$	Transverse residual stress
$\sigma_{ij}$	Cauchy stress tensor
$\tau_R$	Delay time
D	Material stiffness matrix
E	Elastic modulus
F	Equivalent shrinkage force
I	Welding current
K	Thermal conductivity
K	Equivalent shrinkage stiffness
L	Length of the weld seam
M	Equivalent bending moment
n	Exponent related to the reaction speed
p	Phase proportion
Q	Electrical energy consumed
r	Initial root gap
s	Thickness of the plate
T	Temperature
$\nu$	Poisson ration
V	Voltage
x	Shrinkage value
z	Unfused depth of root
$\eta$	Efficiency of heat source
$d\varepsilon^p$	Increment of plastic strain
$d\sigma_Y$	Increment of yield strength
$\alpha$	Thermal expansion
$\varepsilon$	Strain vector
$\theta$	Angular distortion
$\rho$	Density
$\tau$	Lag factor

## CHAPTER 1

### INTRODUCTION AND LITERATURE REVIEW

#### 1.1 Introduction

Prediction of weld distortion has become an important issue in many manufacturing processes. The prediction of the weld distortion can partially or fully eliminate the post processes needed to mitigate the distortion. In this way, an early stage of study of the distortion can lead to a reduction in manufacturing costs due to extra labor time and facilities consumption. The disadvantage of post welding correction is to add another work step that decreases the productivity.

In the arc welding process, the heat is used to fuse the metal, and filler can be added to the molten pool in order to join two or more parts. The heating and the consequent cooling cycles of this process lead to a non-uniform contraction and expansion of the material. Three main zones can be distinguished after the welding process: the base metal, the weld metal and the heat affected zone. The base metal is not involved in the welding process and it remains near room temperature, whereas fusion zone is the part of the metal that completely melted by the welding heat. During the cooling process, the weld metal contracts to the volume it occupied at room temperature. This contraction is limited by the base metal, which acts as a holding vice. For this reason the weld deposit tends to accumulate tensile stresses, which can cause distortion. The mechanical behavior of welds is strongly related to the heat transfer, the microstructure evolution and thermal stress. As a consequence, the theory behind welding is very complex and difficult to fully understand. Mechanical, metallurgical and thermal analyses are key factors that need to be studied in order to understand the complex coupling of the welding process.

Nowadays the distortion can be predicted using numerical analysis or statistical analysis. Numerical analysis for welding can be divided into transient analysis and shrinkage approach. Transient analysis takes into account the numerous parameters such as shape, size, heat source, melt pool and metal, temperature and rate-dependent phase transformation of the material; whereas the shrinkage approach takes into account just the

linear thermal contraction without the need of temperature and phase transformation material properties.

The main goal of this research is to provide a quick prediction of weld distortion. The objectives focus on the development of a model of distortions after arc welding and validation of the results obtained in virtual analysis with experimental data and data found in the open literature.

## **1.2 Literature Review**

The changes in mechanical, metallurgical and thermal properties of the material characterized the complex coupling of the welding process. Welding is a complex non-linear process that presents a significant challenge to theoretical description [1]. In order to predict the distortion of the material after welding, different methods can be applied. Some of these methods are direct numerical simulation, statistical, empirical and semi-empirical models, and experimental characterization.

### **1.2.1 Numerical simulation approach**

Numerical simulation can be divided into the following categories:

- Transient analysis;
- Shrinkage analysis;
- Local-global analysis.

#### **1.2.1.1 Transient analysis**

The most complex and advanced level of simulation is the transient analysis because physical phenomena such as shape, size, heat source, melt pool and metal, temperature and rate-dependent phase transformation and material properties are required in order to evaluate the distortion and the final microstructure of the metal.

#### **ABAQUS Finite element analysis**

The heat transfer analysis and the consequent distortion of the material can be analyzed with ABAQUS software, which is able to simulate multi-pass welding sequentially coupling the thermal and mechanically analyses and calculating the residual stress and deformation [2]. With ABAQUS, boundary conditions can be added. An example can be

found in the analysis of the arc welding induced residual stresses in butt-joint by Kohandehghan and Serajzadeh [3], where two different conditions including unconstrained and constrained simulations were performed. The simulation results were compared with experimental data showing good correlations. The results showed how constraints affect the thermal and the mechanical response of the plate and how they influenced the final distortion. Long et al. [4] investigated the longitudinal and transverse distortions on a butt joint GMAW welding of a thin plate, using a double-ellipsoid moving heat source with ABAQUS software. The results showed that the FE simulations were able to predict the distortions reasonably well compared to the experimental results. High values of longitudinal shrinkage were found in the weld rather than in the outer rim of the plate (Figure 1.1) and the longitudinal shrinkage increased with the decreasing welding speed.

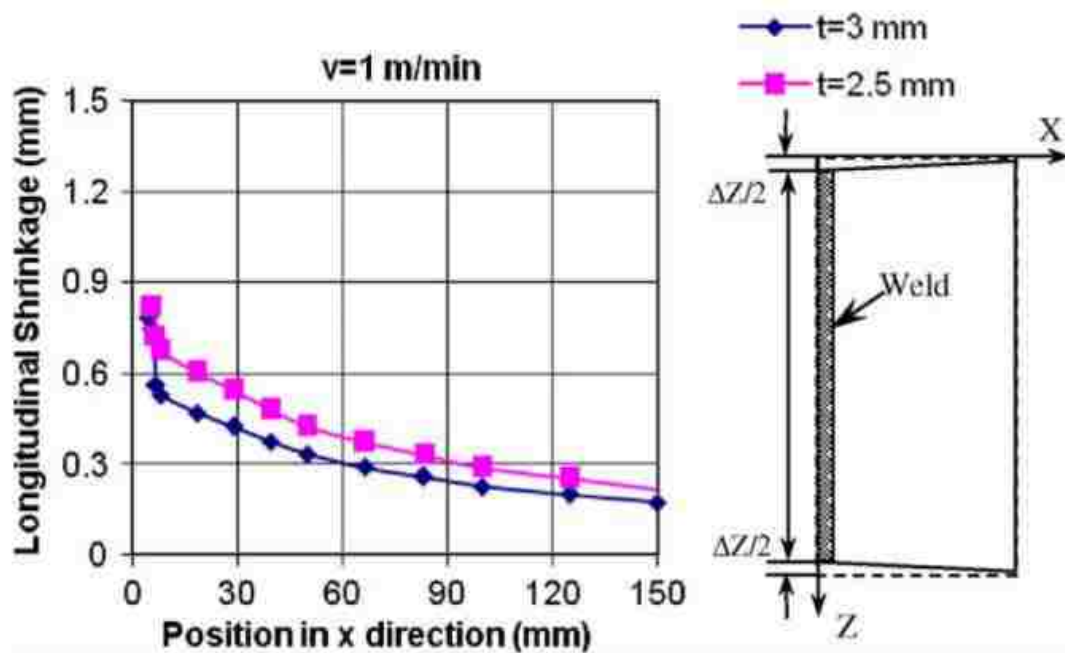


Figure 1.1- Longitudinal shrinkage in 2.5mm and 3 mm thick plate [4]

In addition the highest transverse shrinkage values were found in the middle section along the length the plate (Figure 1.2).

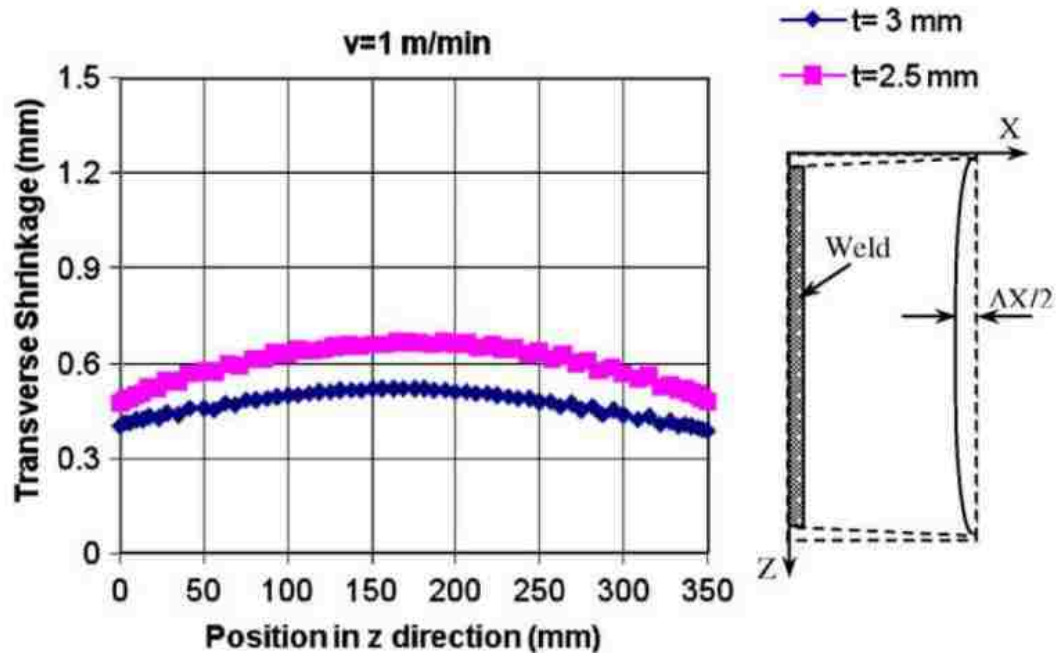


Figure 1.2- Longitudinal shrinkage in 2.5mm and 3 mm thick plate [4]

As for the longitudinal and transverse shrinkages, both increased with lower welding speeds. In general it was observed that the FE simulation yields better results at higher speeds. This can be attributed to the use of the same heat source parameters with different welding speeds and also to the lack of details of the material properties. The simulation slightly underestimated the distortion, whereas the empirical predictions (Section 1.2.3) showed a significant underestimation.

Michaleris and DeBiccari [5] introduced a decoupled approach combining a two dimensional welding simulation and a tridimensional structural simulation. The two dimensional simulations assure a correct welding load prediction on the structure. Since residual stresses can lead large structure to buckle, the stress distribution is fundamental. The welding simulations were performed with ABAQUS and the nonlinear transient heat flow analyses were carried out in a plane perpendicular to the welding direction. In addition, heat conduction, quadratic and quadrilateral elements were used. In order to achieve a better simulation, the heat losses to the support were also assumed and supports with gap conductivity elements were introduced to the model. The double ellipsoid heat source was taken as a reference for each fillet in the welding process, radiation and convection boundary conditions were specified for each free surface. As for the



mechanical analysis plane strain quasi static finite element analyses were accomplished using quadrilateral elements; the mesh was the same as the one in the thermal analysis. The residual stress field from thermal simulation is applied as a load in the mechanical analysis. Results were compared with the experimental data, and in general good agreement is achieved with only the exception of the temperature in the weld region. This behaviour can be attributed to the two dimensional model that does not take into account the heat flow in the welding direction. The plain strain assumption was confirmed by the experimental results that showed that the residual stresses were independent from the panel size. The critical buckling load was compared to the applied load using continuum and structural models in the three finite element methods. At the end, the decoupling of the weld simulation was showed to be efficient and time saving; it also allowed quick changes of the geometries.

Even though ABAQUS has the ability to provide an accurate welding simulation, the building of the model and consecutive calculations require significant amount processing time. For instance, an 80 pass welding simulation using ABAQUS would require a setup of 240 steps, with the assumption of 3 steps per pass, and the need to insert all the step time and initial temperatures. The amount of data required for the setup of the inputs is significant. For this reason, the Abaqus Welding Interface (AWI) is available as an ABAQUS/CAE plug-in. It improves the two-dimensional welding simulations; moreover the setup time for the previous example of an 80 pass model is approximately one hour compared to days with the standard simulation [6].

### **ANSYS-Finite Element Analysis**

The commonly used software, ANSYS-FEA, simulates the main phenomena occurring in the welding process, starting from the transient heat transfer and finishing with the structural thermal-mechanical analysis using axisymmetric and nonlinear analysis [7]. The study of the distortion of the welding of two double endplates of a calandria vessel is performed with the use of ANSYS-FEA [7]. Small scale and large scale welding tests were carried and the results were compared with the simulations that included the heat flow and the elastic plastic analysis. Some simplifications were introduced in order to reduce the complexity of the simulation. ANSYS was also used in a study for the GMAW

welding assembly on auto-body high-strength steel panel and door hinge [8]. In this study, moving ellipsoid heat source and birth-death element method were used in order to obtain the complex transient temperature distribution and the mechanical residual stresses. The simulation showed good agreement and the method was used to optimize a number of parameters. In Sattari-Far's research [9], the ANSYS software was used to determine the effect of nine different welding sequences on an AISI 304 stainless steel pipe. In the 3D modeling, birth-death element method was introduced, whereas in the experimental model, the diameters of the pipes were measured before and after the welding. In order to find a suitable and more appropriate welding sequence, two criteria were introduced: the maximum diameter variation and the average diameter variation. The results showed that the simulation results were in good agreement with the experimental results. The pipe diameter distortions were negative within the weld zone and became positive far from the welding center line. In this research it is observed that a welding sequence made of four segments can lead to higher distortions compared to a two segment welding sequence.

### **VRWELD**

Software called **VRWELD** is able to simulate the transient behavior of the temperature and the microstructure evolution after the welding process. A validation of this software was conducted by Goldak and Asadi [10]. They compared the results of the simulation conducted with VRWELD with the experiments conducted by Masabuchi [11].

### **SYSWELD**

The most commonly used and purpose-built finite element package for transient simulation is SYSWELD [12]. It enables the users to control the welding process without deep knowledge of the computational methods since the thermo-mechanical simulations are already built into the software. It is useful to find the optimum process parameters (Figure 1.3).

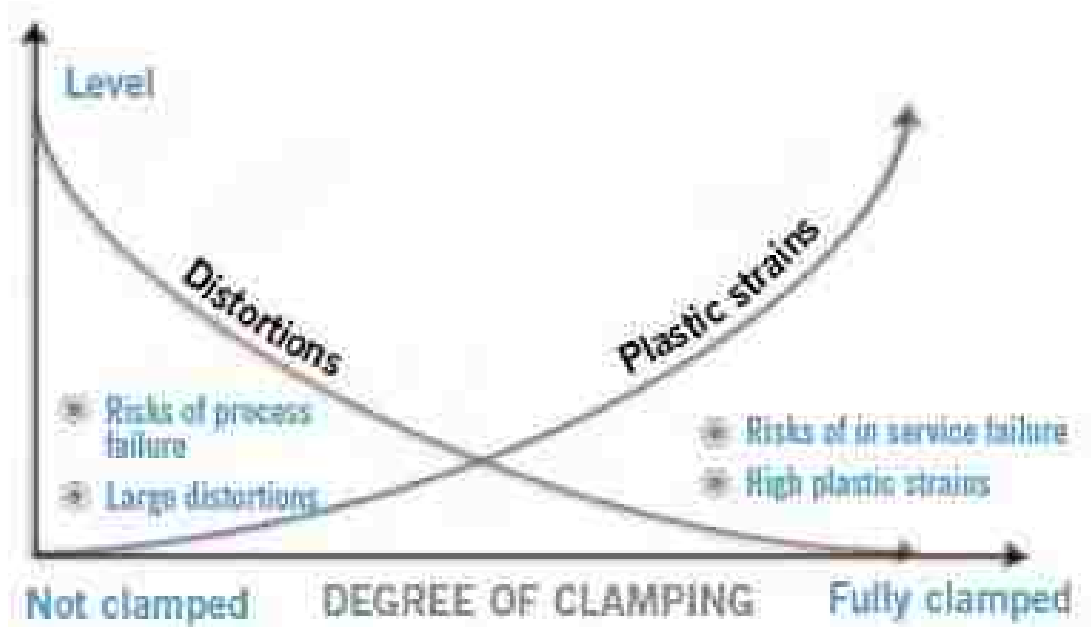


Figure 1.3- Example of optimization [13]

The phase composition can be easily simulated with the input of the phase-dependent material properties. Even though this is the most accurate software in the welding distortion field, the time required to model large assemblies can be enormous. In order to decrease the time of the simulation different strategies can be applied. For example, in Feulvarch's research [14], multi-pass welding was simulated with SYSWELD in 2D and in 3D. The results showed that even though the 3D model is required in order to show the phenomena in the HAZ and the overlapping region, the 2D axisymmetric simulation enables an understanding of the stress distribution in the HAZ with a drastically reduced computational time. The reduction was accomplished with the assumption of the one-time deposition of the heat input. In addition, the 2D model showed good correlation with the experimental data collected with deep hole drilling and neutron diffraction. With the use of numerical simulations, some inputs can be changed in order to study the different residual stresses and distortions in the material. For example in Nazemi's research [15] a 3D welding model was developed with SYSWELD in order to study the effect of each temperature dependent material property on the transient temperature of the welding process. The study successfully calculated the microstructure of the heat affected zone and the residual stresses. The results obtained with the software were compared with different sets of experimental data. In addition some parameters were varied during the

simulation, such as welding speed, welding current, welding voltage and thickness. The results showed that the effect of the welding speed was the most influential compared to the other parameters.

In welding there is a strong coupling between thermodynamics, mechanics and microstructure properties. For this reason Heinze et al. [16] studied the thermal model using experimental data to configure equivalent heat sources which were input for the thermal model. The work concentrated on the equivalent heat sources such as conical Gauss or double-ellipsoid Goldak heat source. SYSWELD was used to run the simulations, varying the heat source parameters and the thermal conductivity. In addition, this software made it possible to introduce the metallurgical phase transformation in the simulation. Even though the pulsed GMA welds led to complex weld pool shapes, the challenge of this characteristic could be overcome using SYSWELD to simulate the experimental weld geometry.

In the research of Lidam et al. [17], the angular distortion analysis of a multipass welding process on combined joint types was studied using SYSWELD. The multipass welding advisor included in SYSWELD was used to evaluate the angular distortion produced by GMAW process. The goal of the research was to analyze the angular distortion of a combined butt and t-joint using SYSWELD and experimental results. The experiments were carried using a fully automated welding process with GMAW power source and shielding gas composition of Ar/CO<sub>2</sub> (80/20). The specimen of low carbon steel was clamped during the whole welding process.

The experiments were simulated with 2D and 3D models and an extensive study was made in order to calibrate the heat source of the GMAW to be equal to the molten zone of the specimen. The angular distortion was calculated using a coordinate measuring machine, and measurements were conducted before and after the welding process at 12 different points. Based on the results, the 3D model showed better correlation with an error of 14-17% compared with the 2D model with an error of 38-40%. On the other hand, the 2D simulation was significantly faster (20 min) compared with the 3D simulation (30hrs).

In Kumari and Sairam work [18], the thermal and mechanical analysis of EBW for a butt joint is performed with the use of SYSWELD. Specific attention was dedicated to study of

the effect of the clamp releasing time on angular distortion and residual stresses. Three different clamping conditions were evaluated: unclamped, clamped until the end of the welding process and clamped until cool down at ambient temperature. The analysis showed that the clamping condition with cold release induces less distortion compared to the other clamping conditions, but at the same it increases the residual stresses.

### 1.2.1.2 Shrinkage approach

The shrinkage volume approach is the fastest and least complex method due to the fact that neither temperature nor phase dependent material data are required for the prediction of the welding distortion [12]. The shrinkage approach assumes that a linear thermal contraction is responsible for the distortion; the elements shrink with a value that is equal and opposite to the thermal expansion that would have occurred if the material was heated up to its melting temperature [12] [19]. This method is useful in the design stage of welded parts because it is less time consuming compared to the transient analysis. The software WELD PLANNER is dedicated to identify distortions, critical weld joints, clamping conditions and weld sequences using the shrinkage method [20]. ESI group compared the full transient analyses and the shrinkage method in a T-joint configuration [20]. The transient simulation had similar level of distortion compared to the shrinkage method [20] as shown in the Figure 1.4 and Figure 1.5.

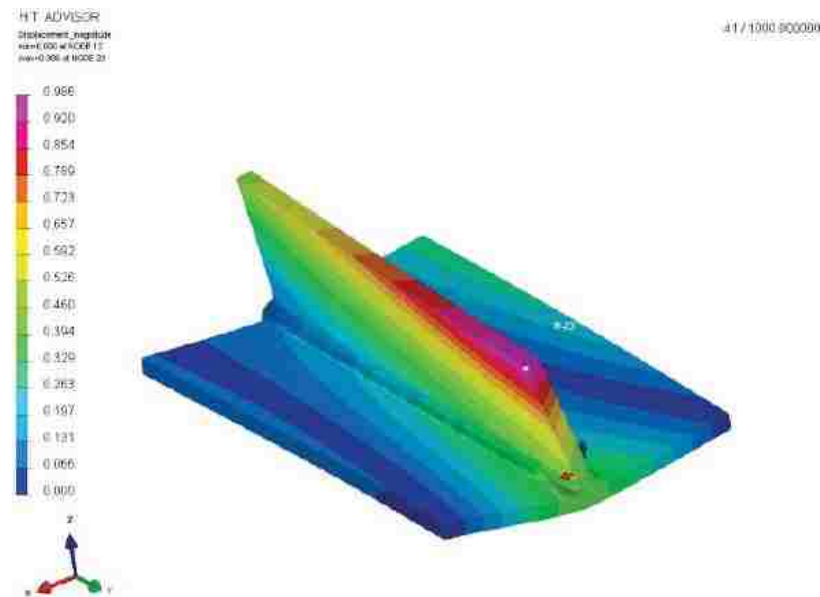
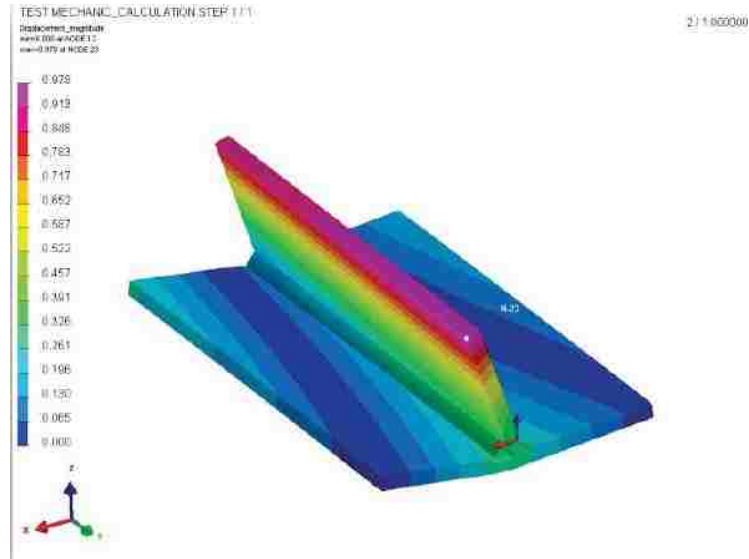


Figure 1.4-Full transient analysis (displacements) [20]



**Figure 1.5-Shrinkage analysis (displacement) [20]**

Jackson and Darlington [12] studied the shrinkage method using WELD PLANNER for the distortion evaluation of an aero-engine assembly. They compared the results with the distortion values found by the transient analysis using SYSWELD with the goal to introduce new optimization for the distortion reduction. The comparison showed that the maximum distortion for the shrinkage method was 4% lower compared with the transient analysis (Figure 1.6). Additionally, the shrinkage approach was faster, and it allowed performing numerous simulations with different welding sequences that would not have been feasible using the transient analysis. The procedure used for the setup is introduced in the following chart (Figure 1.7).

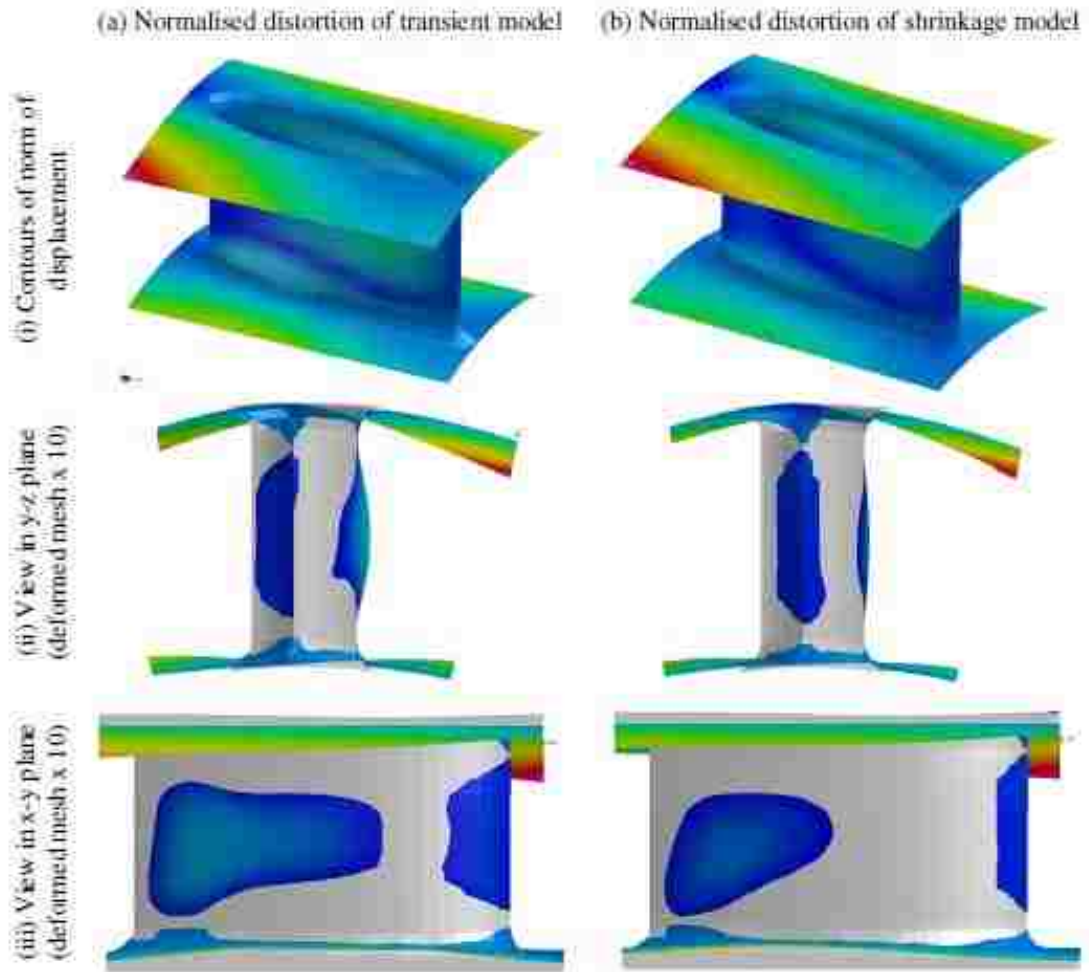


Figure 1.6-Comparison of distortion in the transient model and in the shrinkage model [12]

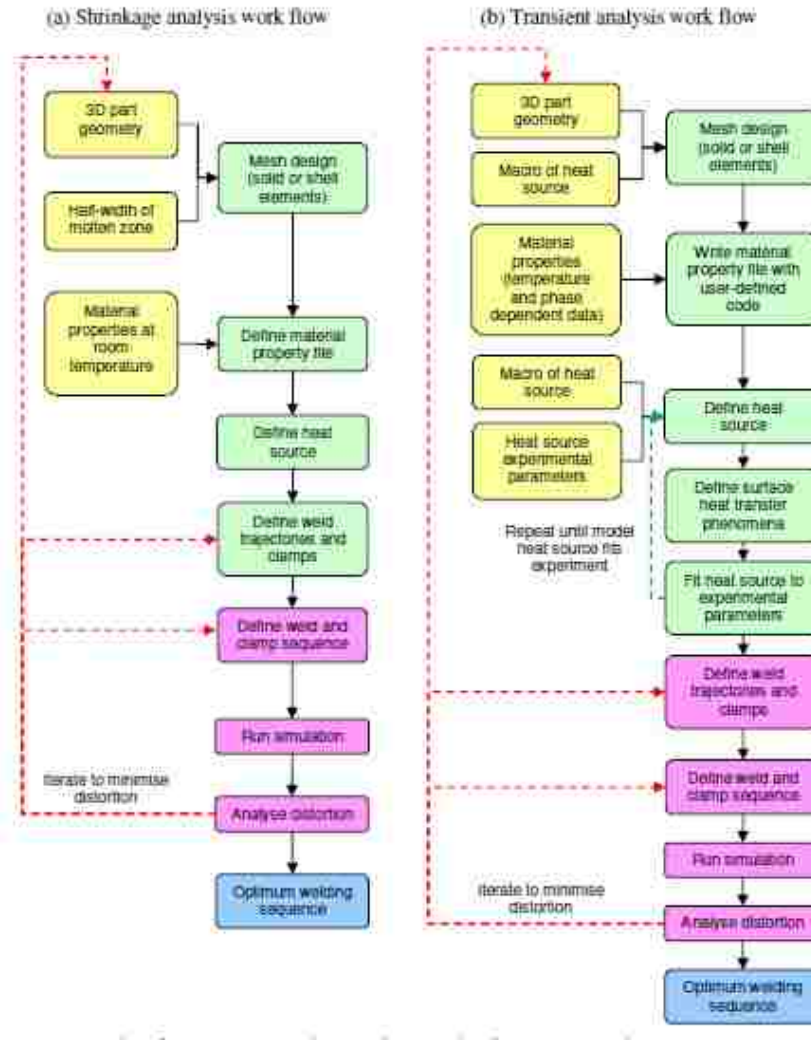


Figure 1.7-Example of the procedure for setting up welding models: (a) shrinkage analysis; (b) transient analysis [12]

Sulaiman et al. [21] studied the welding deformation of a butt joint and T-joint made with 4mm thick low carbon steel using WELD PLANNER. For the verification, experiments were performed using an automated welding system with GMAW power source. In the simulations of both butt and T-joint, different clamping sequences were performed. In the linear elastic analysis, only thermal and mechanical analyses were taken into consideration. The finite element analysis with the shrinkage method showed good correlation with the experiment; the errors were 19.6% and 20.9%.



### **1.2.1.3 Local-global analysis**

Distortion prediction in large structures can be very difficult; for this reason, the projection method is introduced. It consists of studying the global process starting from a smaller sub-process. If this procedure is composed of two length scales, the method is called local-global analysis [22]. The model consists of applying the distortions found in the local simulation in the whole structure. This approach is implemented in the PAM-ASSEMBLY software. It has the advantage of reducing the simulation time compared to the full transient analysis. However, it still requires SYSWELD for the simulation of the local analysis [12].

### **1.2.2 Statistical approaches**

Various methods can be used to define the input values required to produce the desired output variables through the development of mathematical models. Surrogate models can be used when the output cannot be easily calculated. In the field of welding distortion, the surrogate models can help to avoid the non-linearity of the process. In addition, this type of model can decrease the simulation time and find the solution with all the possible combinations. Surrogate models were studied by Goldak and Asadi [23]. They demonstrated how a model was able to minimize the distortion in a girth weld of a pipe with 6 sub-passes by analyzing just 14 sequences.

Interesting results were obtained by Dhas and Kumanan [24]. They proposed the weld residual prediction methodology in four different stages: data collection by FEM, building ANN (Artificial Neural Network) and fuzzy logic models, training the models and the development of the models. The proposed models are able to handle uncertain, nonlinear and time-varying processes. An example of the ANN architecture for the residual stress prediction is shown in Figure 1.8. Both methods were implemented using dedicated Matlab Toolbox, and the results showed a good correlation between the simulations and the experimental data.

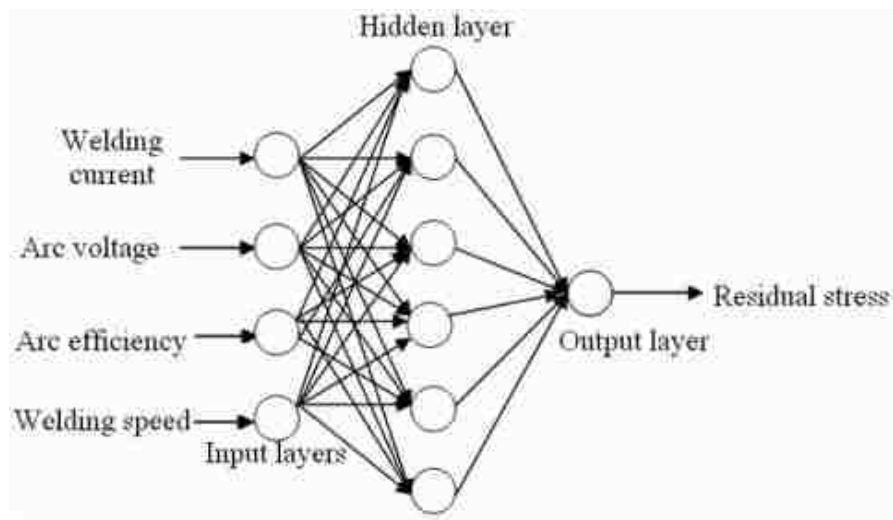


Figure 1.8-Developed ANN architecture for the residual stress prediction [24]

Tian et al. [25] developed an ANN model to predict the transverse and angular distortion of an S304 material using gas-tungsten arc welding. The experiments were bead-on-plate welds. The angular and transverse distortions were calculated across a certain range of welding parameters. Additionally a finite element method was developed in ABAQUS. The simulation consisted of a step of non-linear transient thermal analysis and a step of temperature history needed to calculate the distortion. The results showed the non-linearity between the input welding parameters and the final distortion. For this reason, an artificial neural network was used to solve the non-linearity problem. A BP network, which consists of one or more hidden layers and an output layer, was used and trained using a Matlab Toolbox. The accuracy of the BP network was verified by comparison to the experimental results with a correlation coefficient of 0.99.

Other methods such as Genetic Algorithm (GA), Response Surface Methodology (RSM), Taguchi Method and Factorial design can be used in order to obtain the desired output. The following Table 1.1 compared the different methods.

**Table 1.1- Comparison between the common modeling-optimization techniques [26]**

Technique Comparison	ANNs	GA	RSM	Taguchi	Factorial Designs
Computational time	Long	Very long	Short	Medium	Short
Experimental domain	Regular or irregular	Regular or irregular	Regular only	Regular or irregular	Regular only
Model developing	Yes*	No	Yes	No	Yes†
Optimization	Through model	Straight	Through model	Straight	Through model
Understanding	Moderate	Difficult	Easy	Normal	Easy
Availability in software	Available	Available	Available	Available	Available
Optimization Accuracy level	High	High	Very high	Normal	Very high
Application	Frequently	Rarely	Frequently	Rarely	Frequently

\*) No factors interaction effects. †) No factors quadratic effects.

### 1.2.3 Empirical approach

In the literature review, it is possible to find empirical equations that approximate the longitudinal and transverse distortion already discussed in the paragraph 2.2.

For the transverse shrinkage, Sparagen [27] introduced an empirical equation for a butt weld:

$$\delta_T = \frac{0.2A_w}{s} + 0.05r, \quad (1.1)$$

where  $A_w$  ( $mm^2$ ) is the cross sectional area of the weld,  $s$  ( $mm$ ) is the thickness of the plate and  $r$  is the initial root gap ( $mm$ ).

For a single pass butt weld White [28] developed the following equation:

$$\delta_T = \frac{3\eta \left(\frac{Q}{v_w}\right) \left(1 - \frac{z}{2s} + 0.2r\right)}{s}, \quad (1.2)$$

where  $z$  ( $mm$ ) is the unfused depth of root,  $s$  ( $mm$ ) is the thickness of the plate,  $Q$  ( $J$ ) is the energy,  $v_w$  ( $\frac{mm}{s}$ ) is the welding speed. The previous equation 1.2 can be implemented in cases where  $z$  and  $r$  are unknown and where the penetration is not complete.

Another example of transverse shrinkage is given by Capel's formula [11](Equation 1.3) calculated on butt welds in 6.4mm thick plate for carbon steels:

$$\delta_T = \frac{17.4Q}{sv_w} \times 10^{-3}, \quad (1.3)$$

where  $s(mm)$  is the thickness of the plate and  $v_w \left(\frac{mm}{s}\right)$  is the welding speed. As for the longitudinal shrinkage, Okerblom [29] introduced the formula (Equation 1.4) for the distortion prediction in case of fast welding speeds:

$$\delta_T = \frac{0.335Q}{A_w v_w} \frac{\alpha}{\rho c_p}, \quad (1.4)$$

where  $\alpha$  is the coefficient of thermal expansion,  $c_p$  is the specific heat,  $v_w \left(\frac{mm}{s}\right)$  is the welding speed and  $s(mm)$  is the thickness of the plate. In Long's research [4], the empirical results showed considerable underestimation of the welding distortion compared to the FE simulations.

#### **1.2.4 Industrial relevance for welding distortion prediction**

The use of lightweight structures is a key point in the reduction of fuel consumption and operating costs in automotive and ship building industries. The use of lightweight materials is widely shared in aviation field. It will grow significantly in the automotive field from 30 to 70 percent by 2030, as it is possible to observe in the Figure 1.9 [30].

High strength steels are considered lightweight materials and a large number of companies are focusing their research on them. Currently, not all welding techniques are able to reach satisfactory shape distortions. The US Navy Office of Naval Research [31] states that several distortions have emerged as a major obstacle to the cost-effective fabrication of lightweight structures.

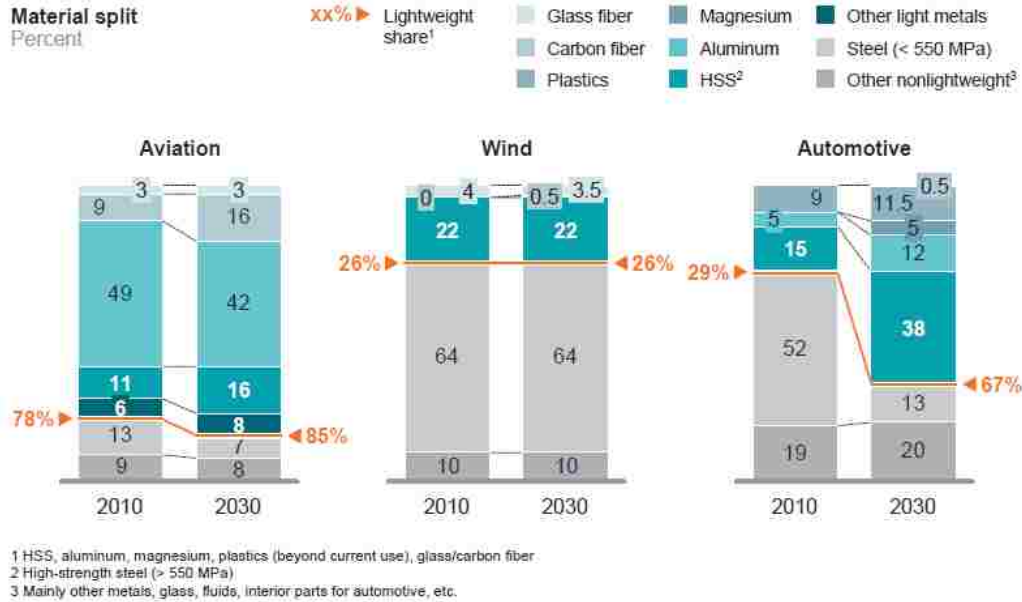


Figure 1.9- Share of lightweight materials in aviation, wind and automotive field [30]

According to Volkswagen, the use of software for welding prediction can save one or two potential loops, meaning 10-20 k€ per part reduction [32]. In automotive assembly, doors are assembled to auto-body side-frame through hinges by GMAW (Figure 1.10). Distortion of the hinges can seriously affect the position of the door, which can lead to poor sealing and abnormal sounds during closing and opening [8].

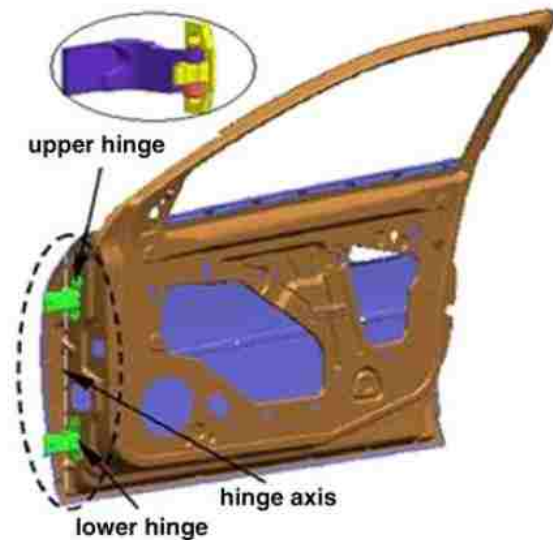


Figure 1.10-Illustration of door hinge assembly [33]

## CHAPTER 2

### THEORY BEHIND WELD DISTORTION AND NUMERICAL APPROACH

#### 2.1 Theory behind weld distortion

##### 2.1.1 Fundamentals and general technology of welding

Welding is a process in which two parts can be joined together at their contact surface using heat and/or pressure. Welding is widely employed in fabrication due to its good reliability, cost-effectiveness and high efficiency [25]. The welded joint can be stronger than the parental metal, and it is an economical way to join materials. In theory, continuity between the two parts should be observed, and the joint area should be indistinguishable from the parent metal of the individual parts [34]. Unfortunately, the ideal conditions cannot be achieved. For this reason, different types of welds should be performed for different materials. In some welding processes, filler is added in order to facilitate the coalescence of the two materials. However, there are some drawbacks in welding processes, such as the high energy required, inconvenient disassembly and quality defects in welded joints.

The welding process can be divided in two categories: fusion welding and solid state welding. The former one is the most important and widely used category and includes arc welding, resistance welding, oxy-fuel gas welding processes.

In fusion welding, the heat is used to fuse the metal; and usually filler is added to the molten pool to facilitate the process and provide bulk and strength to the welded joint [35]. The fusion welded point consists of three different zones (Figure 2.1):

1. Fusion zone: filler metal and base metal that have completely melted. This zone presents a high degree of homogeneity and an epitaxial grain growth, in which atoms from the molten pool solidify on preexisting lattice sites of the adjacent solid metal base [35]. In this way the crystallographic orientation can be minimized near the heat-affected zone, whereas a preferred orientation can be found further inside the fusion zone in which grains are perpendicular to the weld interface;

2. Weld interface: the boundary that divides the fusion zone from the heat-affected zone. This interface is relatively thin due to the fast solidification that occurred before any mixing with the metal in the fusion zone;
3. Heat-affected zone (HAZ): in this zone the metal has experienced temperatures that are below its melting point, but were high enough to cause a microstructural changes inside the solid metal [35].

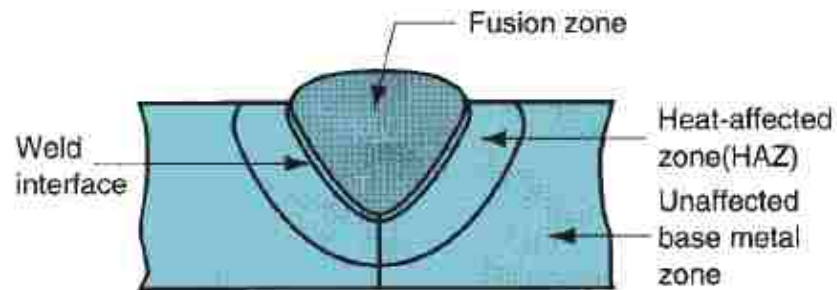


Figure 2.1- Principal zones in a cross section of a welded joint [35]

Arc welding (AW) is a fusion welding process where two parts are coalesced using an electric arc between an electrode and the work pieces. The electric arc is a discharge of current across a gap in a circuit, it is sustained by the presence of a thermally ionized column of gas (plasma) through which a current flows [35].

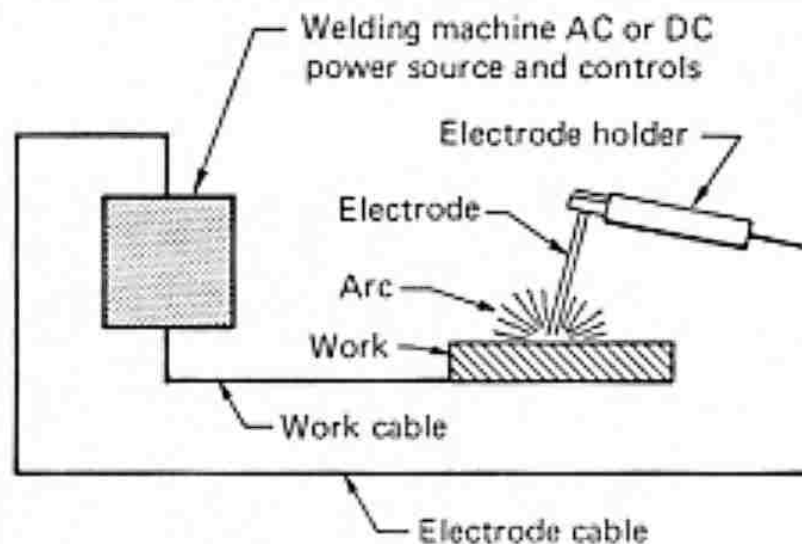


Figure 2.2- Basic arc welding configuration [36]

Two types of electrodes are used in arc welding: consumable electrodes and non-consumable electrodes. The former ones provide filler metal during the process; because they are consumable, they need to be changed during the weld process. The latter ones are made with tungsten which resists melting during the operation; in this case the filler has to be supplied separately.

Another important feature in arc welding is the arc shielding. At high temperatures, molten metal is chemically reactive with the surrounding air, which can negatively affect the quality of welding. For this reason, the electrode tip, arc and molten pool have to be covered with a blanket of flux or gas to prevent the exposure of the molten metal with the air [35].

The energy supplied by the power supply to the electrode is directly proportional to the welding current [34] as can be obtained by the equations 2.1 and 2.2:

$$Q = I * V, \quad (2.1)$$

$$Q = I^2 R_a, \quad (2.2)$$

where  $Q$  is the electrical energy consumed ( $J/s$ ),  $I$  is the welding current (A),  $V$  is arc voltage (V), and  $R_a$  is the arc circuit resistance ( $\Omega$ ). The welding current plays an important role in the quality of the welding because it affects the electrode melting rate and enhances the deposition rate, the depth of the penetration and the amount of the base metal melted [34]. Moreover, if the current is too high increased penetration may result in burn through, if the current is too low it may result in a lack of fusion. The arc voltage is the voltage between the electrode and the work during welding [34]. The arc length and the electrodes influence the arc voltage.

Welding speed is the linear rate at which the arc moves along the weld joints [34]. Because it controls the actual time of the welding, the welding speed is usually kept constant while the other parameters such as the current and the voltage are varied in order to control the weld quality. Moreover, in order to properly determine the welding speed, it is important to take into consideration that at high welding speed, the filler cannot be



perfectly deposited, thereby reducing the reinforcement. In addition, if the welding speed is too low the weld bead gets wider and more convex.

Arc welding can be classified by the type of electrodes used in the process. There are two methods: arc welding with consumable electrodes and arc welding with non-consumable electrodes.

Arc welding with consumable electrodes can be divided into different categories:

- Shielded Metal arc welding (SMAW): also known as manual welding, is a welding process that uses an electrode that consists of a filler metal rod that conducts the welding current from the electrode holder to the work. When the arc is melted, a portion of the coating of the electrode melts into the weld. The coating breaks down to become protection from the atmosphere during the process.
- Gas metal arc welding (GMAW): uses a continuous electrode feed that is shielded by a gas (Figure 2.3) [37]. This process is very fast and economical; in addition it is widely used for fabrication due to its versatility to weld different metals [38]. Since it uses continuous wire, there are advantages in terms of arc time and the utilization of the electrode material [35].

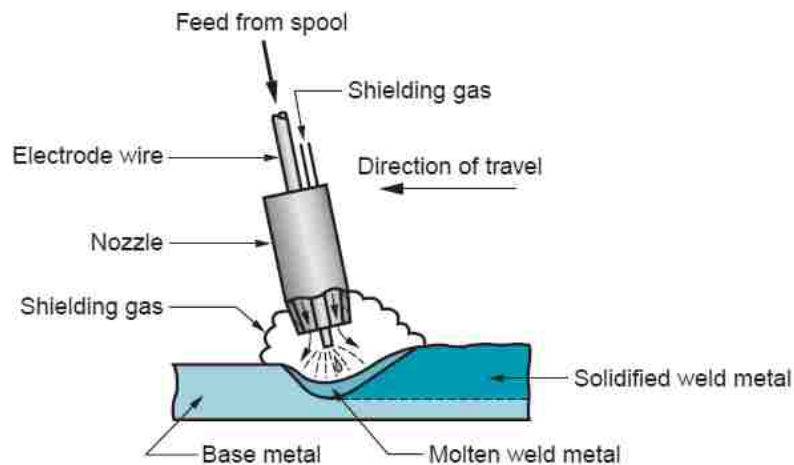


Figure 2.3- Gas metal arc welding (GMAW) basic configuration [35]

- Flux-Cored arc welding (FCAW): is similar to GMAW in that it uses a flux core electrode that can be continuously fed from the spool. There are two methods for the FCAW: self-shielded (FCAW-S) and gas shielded (FCAW-G), these methods differ from each other by the method of shielding.
- Electrogas Welding (EGW): uses an arc between a continuous filler electrode and the weld pool with a vertical progression.
- Submerged arc welding (SAW): uses a continuous wire electrode. The arc is shielded are by a cover of a granular flux, which fills the joint ahead of the arc [35].

As for welding with non-consumable electrodes, the following types are introduced:

- Gas tungsten arc welding (GTAW): uses a tungsten electrode and an inert gas for arc shielding (Figure 2.4) [35]. The process can be applied with or without a filler material. When a filler is used, it has to be added to the weld pool in a separately way. The choice of tungsten is due to its high melting temperature. The application of GTAW is suitable for every metal and for the joining of different materials. It is more expensive compared to the arc welding with consumable electrodes due to its lower speed and arc efficiency [35].

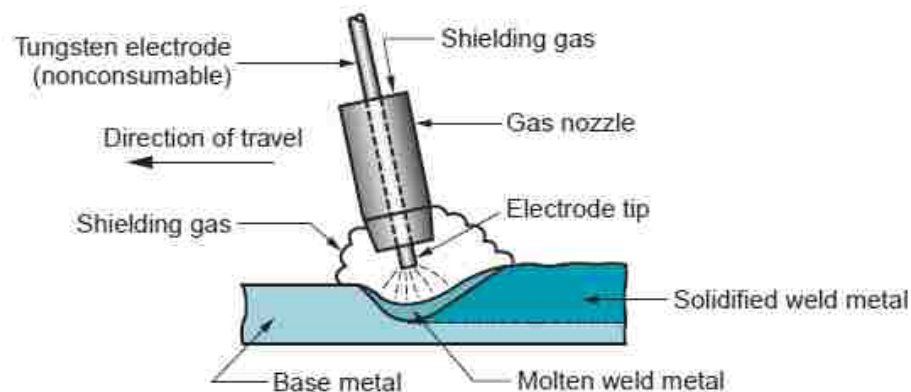


Figure 2.4-Gas tungsten arc welding (GTAW) [35]

- Plasma arc welding (PAW): is a variant of GTAW welding that employs a plasma arc directly on the weld pool. In recent uses, PAW has replaced to GTAW due to its better welding speed and lower cost [35].

Moreover, five different types of weld joints are classified to joint two parts together as shown in Figure 2.5 and Figure 2.6:

- (a) Butt joint: the two parts are in the same plane and the joint occurs along the edge;
- (b) Corner joint: the two parts form a 90 degree angle and the joint occurs along the corner;
- (c) Lap joint: two parts are overlapped;
- (d) Tee joint: one part is perpendicular to the other one, forming a T shape;
- (e) Edge joint: the two parts have at least a common parallel side and the joint occurs along the common edge.

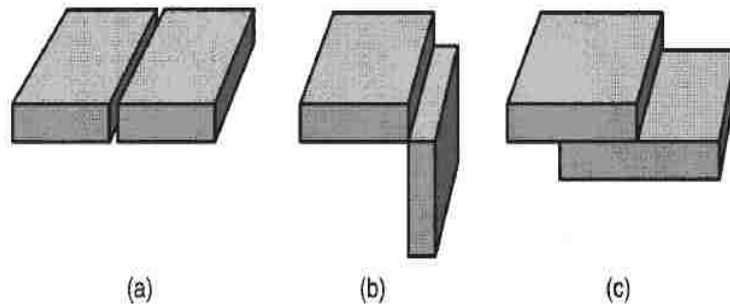


Figure 2.5-(a) Butt joint, (b)Corner joint and (c) Lap joint [35]

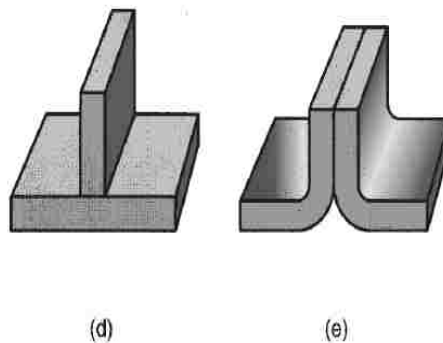


Figure 2.6- (d) Tee joint and (e) Edge joint [35]

### **2.1.2 Complex coupling in welding modeling**

The welding process also induces undesired aspects, such as distortions due to residual stresses, which reduce the reliability of the material. The complexity and non-uniformity of the temperature, as well as the subsequent rapid cooling in the welding process, lead to significant changes in the thermal, mechanical and material properties of the welded metals. In order to better predict the distortion and the residual stresses inside the welded material, some models have to be introduced.

The complexity of the welding process can be studied from both macroscopic and microscopic point of view. Macroscopically, the weld is considered to be a thermo-mechanical problem; whereas microscopically it is considered to be a metallurgical problem, which includes phase transformation, grain growth, dissolution and precipitation [39].

The heating and the cooling cycles of the welding process lead to a non-uniform contraction and expansion of the weld metal and the base metal, whereby strains occur. Since the base metal is not involved in the welding process and it is far away from the molten zone, it remains at room temperature. This “cold” part acts as a vice holding the welded zone and the adjacent base metal restricting the expansion and contraction. When the weld metal cools down, it tries to contract to the volume it would have occupied at room temperature; but because it is restrained by the base metal it cannot do so. For this reason, after the weld, the base metal is cooled down and the weld deposit tends to lock-in tensile stresses of the near yield point magnitude. These stresses are balanced with compressive stresses in the adjacent base metal [40]. These high stresses promote fracture, fatigue and distortion. There are different types of distortion.

Shrinkage: it can take place both in the transverse direction perpendicular to the welding line and in the longitudinal direction parallel to the welding line (Figure 2.7). From previous experiments, it is observed that the transverse shrinkage is much higher compared to the longitudinal shrinkage, and that the transverse shrinkage is mostly due to the base metal contraction [11].

For this type of distortion the linear elastic shrinkage volume method can be introduced. The original analysis method, the steady state finite element approach, assumes that the main distortion is a result of the contraction of the weld metal after the cooling. The linear shrinkage volume approach predicts the magnitude of these distortions reasonably well. Therefore it is a very useful tool in the prediction of large and complex structures [19].

The shrinkage forces lead to different types of weld distortion. Depending on the kind of forces, angular, rotation and buckling can take place.

- Angular: it is the result of different shrinkage forces across the plate thickness;
- Rotational: it is affected by both, heat input and welding speed [40];
- Buckling: the stresses in locations far from the weld zone produce plastic deformation that can lead to buckling during cooling. Because buckling has much more severe distortion compared with angular deformation, it is important to properly select structural and welding parameters in order to avoid buckling.

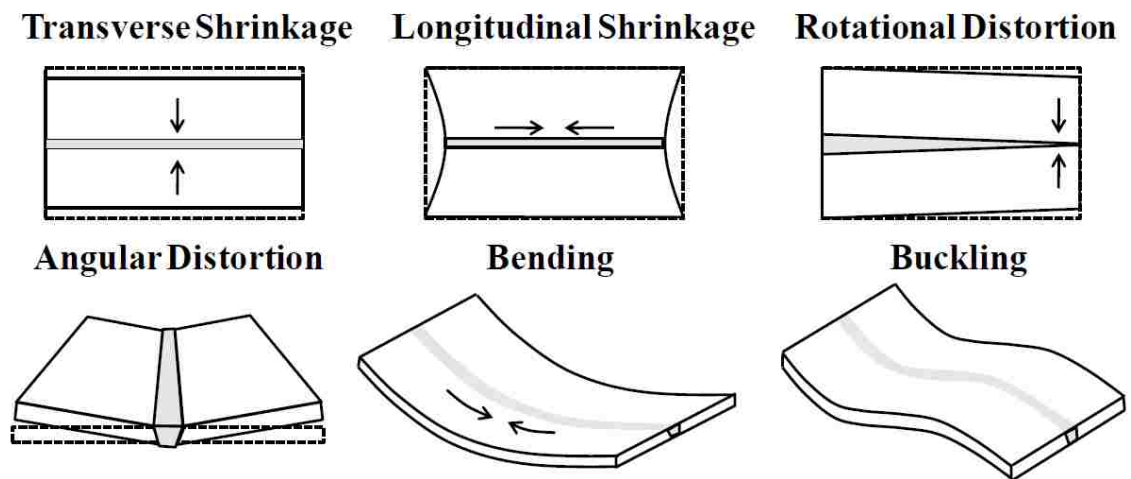


Figure 2.7- Different types of welding distortion [11]

The mechanical behaviour of welds is strongly related to the heat transfer, the microstructural evolution and thermal stress as highlighted previously. Figure 2.8, describes how the coupling works in the welding process.

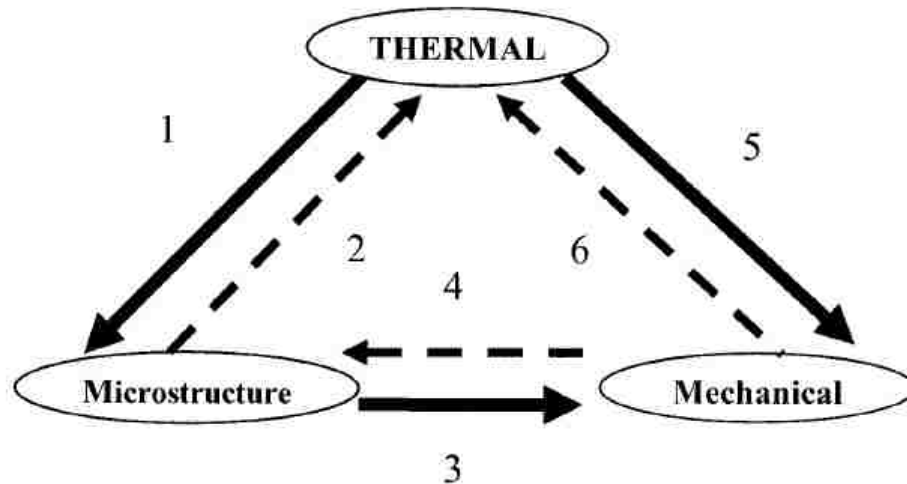


Figure 2.8-Coupling welding process [39]

The coupling can be explained in the following way [39]:

1. Transformation rate: the microstructure evolution depends on the temperature;
2. Latent heats: they act as heat sinks on heating and an heat source on cooling;
3. Phase transformations: volume changes with the phase changes and consequent microstructure changes;
4. Transformation rate: mechanical stresses can lead to microstructural changes;
5. Thermal expansion: temperature drives the mechanical deformation
6. Plastic work.

In the last years several methods were introduced in order to solve this complex coupling, but the finite element method (FEM) is widely used to predict the thermal, material and mechanical effect of welding.

In the following sections the main phenomena that take part in the welding process are introduced.

### 2.1.2.1 Thermal modeling

The thermal history plays an important role for an adequate prediction of the welding distortions. For this reason heat source parameters must to be known. The heat flow of a moving heat source problem was first introduced by Rosenthal in 1935. Rosenthal used the quasi-stationary principle, which stated that a stationed observer at the point source cannot notice any temperature changes around it as the source moves [41]. Moreover, a Rosenthal-type numerical model based on both analytical and experimental measurements was developed by Hess et al. [42]. Rosenthal's model exhibited errors in presentation of the fusion zone and in the heat-affected zone. An improved model was later introduced by Pavelic, whose approach showed more accurate temperature distribution [43]. In order to better predict the temperature distribution, Goldak introduced a double ellipsoid configuration heat source model (Equations 2.1 and 2.2) [44], which is a combination of two different ellipsoids in Figure 2.9.

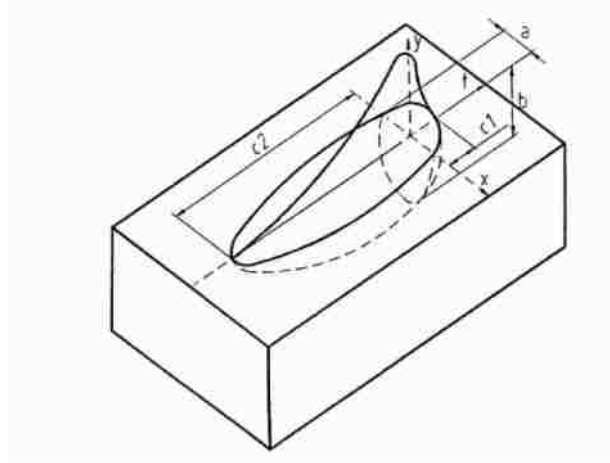


Figure 2.9- Double ellipsoid heat source [44]

$$q_f(x, y, z, t) = \frac{6\sqrt{3}Qf_f}{abc_1\pi\sqrt{\pi}} e^{-\left(\frac{3x^2}{a^2} + \frac{3y^2}{b^2} + \frac{3[z+v_w(\tau+t)]^2}{c^2}\right)} \quad (2.1)$$

$$q_r(x, y, z, t) = \frac{6\sqrt{3}Qf_r}{abc_2\pi\sqrt{\pi}} e^{-\left(\frac{3x^2}{a^2} + \frac{3y^2}{b^2} + \frac{3[z+v_w(\tau+t)]^2}{c^2}\right)} \quad (2.2)$$

where:

- $q_f$  and  $q_r$ : front and rear heat flow or internal rate of heat generation  $\left(\frac{W}{m^3}\right)$ ;
- $v_w$ : welding speed  $\left(\frac{m}{s}\right)$ ;
- $\tau$ : lag factor necessary to find the position of the heat source at time  $t=0$ ;
- $Q$ : electric power of the arc in the ellipsoid that is transferred to the welding part;
- $f_f$ : fraction of heat deposited in the front part of the heat source,;
- $f_r$ : fraction of heat deposited in the rear part of the heat source. (Fractions are specified to be  $f_f + f_r=2$ ):
- $a, b, c_1, c_2$  are parameters that denote the semi-axes of the ellipsoid. These parameters must be determined and they correspond to the radial dimension of the molten zone. If precise data does not exist, it is reasonable to take the distance in front of the source equal to one half the weld width, and the distance behind the source equal to two times the weld width.

In the previous equations, the electric power arc can be expressed in the following way (Equation 2.3):

$$Q = \eta VI \quad (2.3)$$

where  $\eta$  is the efficiency of the heat source in the arc welding, which has a value greater than zero and lower than one;  $V$  is the arc voltage (V); and  $I$  is the arc current (A).

The welding process parameters, such as welding speed and welding current, have a great influence on the weld pool. Once the moving heat source has been calculated, the temperature histories can be computed with Equation 2.4 [3] for transient non-linear heat transfer analyses in case the weld is in the  $y$  direction:

$$\frac{\partial}{\partial x} \left( k(T) \frac{\partial T}{\partial x} \right) + \frac{\partial}{\partial y} \left( k(T) \frac{\partial T}{\partial y} \right) + \frac{\partial}{\partial z} \left( k(T) \frac{\partial T}{\partial z} \right) + q_i = \rho c \left( \frac{\partial T}{\partial t} + v_w \frac{\partial T}{\partial y} \right) \quad (2.4)$$

where:



- $k$  is the thermal conductivity which depends on the temperature;
- $T$  is the temperature;
- $q_i$  is the rate of internal heat generation;
- $\rho$  is density;
- $c$  is the specific heat capacity;
- $v_w$  is the welding speed.

With the thermal history, it is possible to calculate the transfer of thermal energy. When the temperature of the affected material is different from the surrounding material, the heat transfer occurs in order to let the material reach thermal equilibrium. Heat transfer can occur in three ways, by conduction, convection and radiation.

Conduction is the transfer of heat transfer from a region of high temperature to a region of low temperature by the interaction of molecules. The heat transfer occurs when high energy molecules get in touch with low energy molecules, which absorb energy and increase their temperature [45]. Thermal conductivity depends on different parameters such as the temperature, the density and the metal phase. The Fourier's Law (Equation 2.5) can be applied to this type of conduction:

$$q_{cond} = -k \frac{\Delta T}{\Delta x} \quad (2.5)$$

where  $q_{cond}$  is the local heat flux,  $k$  is the material conductivity, and  $\Delta T/\Delta x$  is the temperature gradient.

Convection is the mode of heat transfer in which energy is transported by moving fluid particles [45]. Convection can occur by a diffusion mechanism or an advection mechanism. The former one consists of energy transfer by microscopic fluid motion, whereas the latter one consists of energy diffusion through random molecular motion. The convection can be expressed with the following equation.

$$q_{conv} = -h_c A_s (T_s - T_0) \quad (2.6)$$

where  $q_{conv}$  is the convective heat transfer,  $h_c$  is the heat transfer coefficient,  $T_s$  is the surface temperature of the weld, and  $T_0$  is the ambient temperature.

Finally radiation, which is the transfer of heat when no material is present, can be described according to the following equation:

$$q_{rad} = -\varepsilon_0 \sigma_0 (T_s - T_0)^4 \quad (2.7)$$

where  $\varepsilon_0$  is the emissivity,  $\sigma_0$  is the Stefan-Boltzman constant,  $T_s$  is the surface temperature of the weld, and  $T_0$  is the ambient temperature.

Most significant thermal properties, such as the specific heat, thermal conductivity and density, are temperature dependent, and their variation must be taken into consideration during welding [46] [3]. An example of the material properties variation is shown in the Figure 2.10.

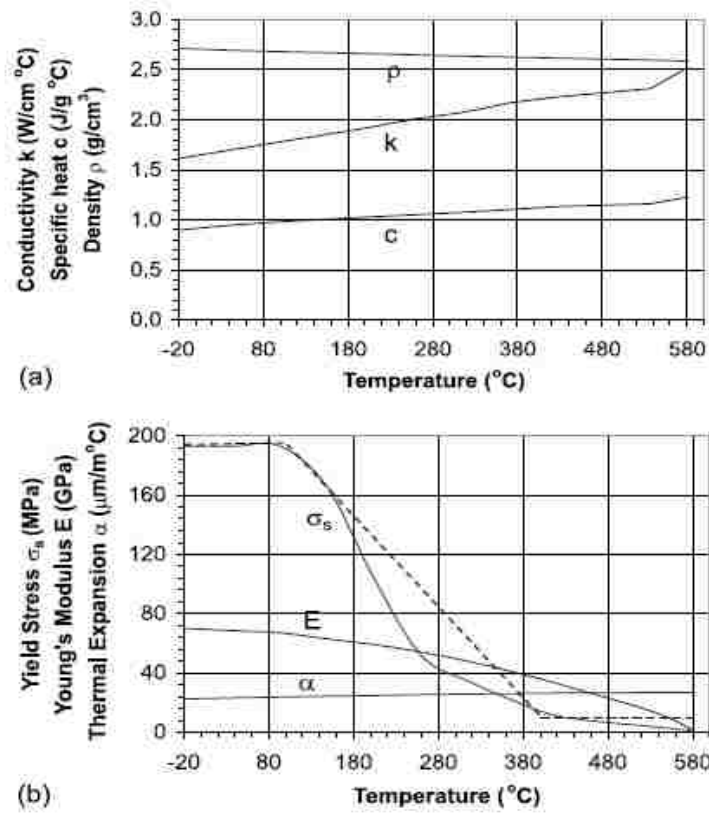


Figure 2.10- Variation of material properties with the temperature for 5052-H32 aluminum alloy (a) thermal properties, (b) mechanical properties [47]

Thermal properties depend also on the composition of the material phases, which in steel are austenite ferrite/pearlite, martensite, tempered martensite and bainite. For instance the thermal conductivity differs between the face-centered cubic austenite and the body-centered cubic ferrite phases. Furthermore the transient temperature field is affected by the latent heat, which has to be taken into consideration in the case of any microstructure transformations and melting or solidification.

### 2.1.2.2 Mechanical modeling

The mechanical properties also change during the welding processes. Yield stress plays an important role in welding because it significantly affects the residual stresses and distortions. In order to achieve adequate results in welding simulations the yield stress and the corresponding plastic deformation should to be taken into account [47]. As briefly introduced in the previous section, melting, solidification and the addition of material induce structural and mechanical transformations. The contraction and the transformation strain during cooling affects the final state of stress [48]. For the welding of steel component, additional microstructure phenomena become relevant. First, microstructural changes lead to volume changes in hardened steels. Second, the transformation of existing phases will have significant influence on the material properties. For instance, after an austenizing heat treatment, steel transforms from body-centered cubic (Figure 2.11) to face-centered cubic (Figure 2.12), and after cooling back to body-centered cubic. The volume change has a definitive impact on the distortions and the residual stresses in the material [48].

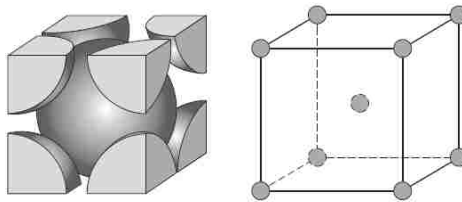


Figure 2.11- Body centered cubic crystal structure [49]-  $\alpha$  phase

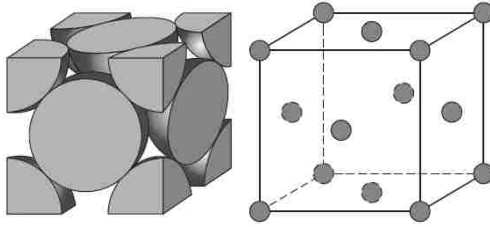


Figure 2.12-Face centered cubic crystal structure [49]- $\gamma$  phase

### 2.1.2.3 Metallurgical modeling

The metallurgical aspects of welding are important in order to study the thermal transformation associated with each zone as shown in Figure 2.13.

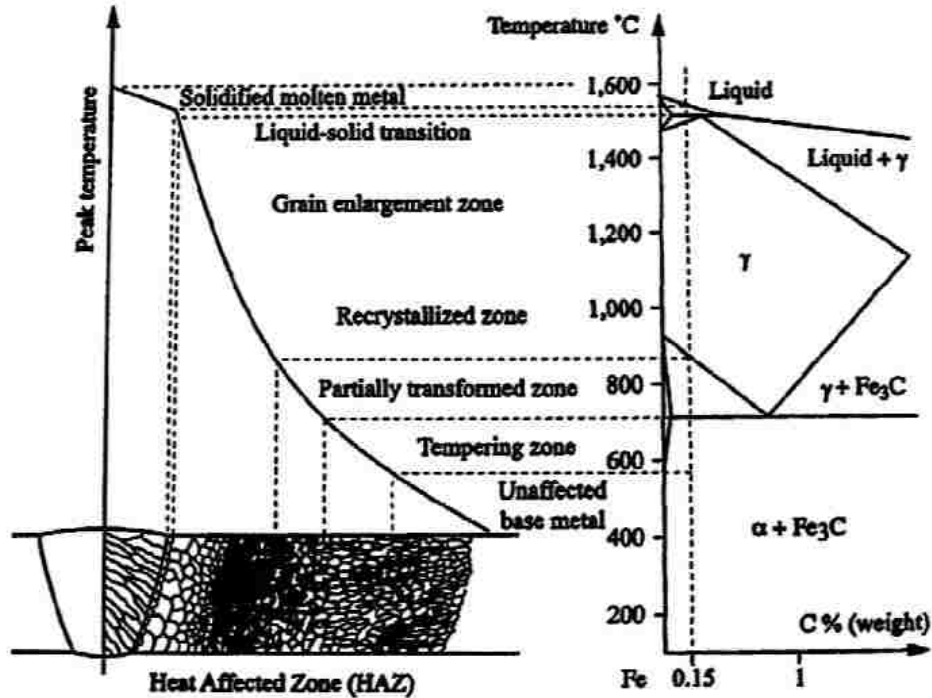


Figure 2.13- HAZ and equilibrium diagram [50]

In addition, an important role is played by the cooling conditions. In general, the phase transformations occur in the heat affected zone. Heating causes the parent structure to transform into austenite, followed by austenite transforming to martensite or ferrite plus pearlite upon cooling. In welding, fast cooling rates restrict the motion of the carbon atoms therefore the formation of martensite is very likely. Nevertheless, ferrite and

cementite phases can be found in the heat affected zone if the alloying percentage is low. The presence of martensite affects the local material properties. It increases the hardness of the material, but can make the material relatively brittle. The presence of coarse, hard grains of martensite in the HAZ near the fusion zone makes the region susceptible to cracking in the presence of martensite and residual stresses, Figure 2.14.

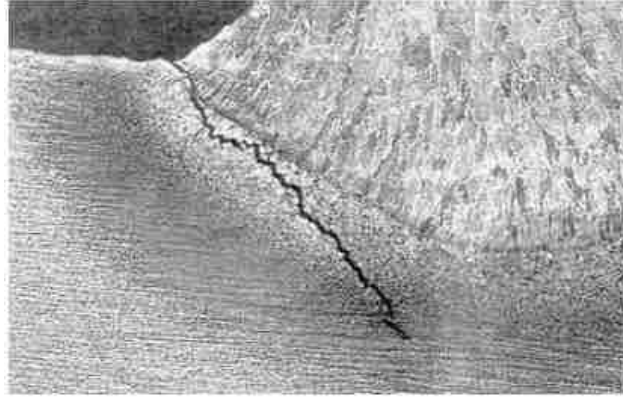


Figure 2.14-Example of visual appearance of hydrogen cracking [51]

An overview of the calculation of the phase transformation in steel is provided by Lidam et al. [17]. The diffusion type transformation from phase 1 to phase 2 is described with Leblond model in following equation 2.8:

$$\dot{p}_2 = n_{1 \rightarrow 2}(T) \frac{\bar{p}_2(T) - p_2}{\tau_{1 \rightarrow 2}(T)} \left( \ln \left( \frac{\bar{p}_2(T)}{\bar{p}_2(T) - p_2} \right)^{\frac{n_{1 \rightarrow 2}(T) - 1}{n_{1 \rightarrow 2}(T)}} \right) \quad (2.8)$$

where  $\bar{p}_2$  is the phase proportion obtained after an infinite time at temperature T;  $\tau_R$  is a delay time; and  $n$  is an exponent related to the reaction speed. The parameters need to be extrapolated from the continuous cooling transformation diagram.

As for the martensitic transformation the Koistinen-Marburger law is introduced in Lidam's [17] research in the following equation 2.9

$$p(T) = \bar{p} \cdot (1 - \exp(-b \cdot (Ms - t))) \text{ with } T \leq Ms \quad (2.9)$$

where  $\bar{p}$  is the proportion obtained at an infinitely low temperature;  $M_s$  and  $b$  are parameters that characterize the initial transformation temperature and evolution of the transformation process taking into consideration the temperature.

### 2.1.3 Residual stresses and distortions calculations

Once all the fundamental phenomena are taken into account, the residual stresses can be calculated (or at least estimated). Different methods can be found in the literature. Kohandehghan and Serajzadeh [3] studied the effect of welding fixtures on distributions and values of residual stresses during GTAW process. The butt joint was investigated using thermo mechanical analysis performed by the finite element program ABAQUS. The model of the arc welding was divided into two steps: the first one was the heat transfer, and the second one was the mechanical analysis. The thermal analysis was studied with the double ellipsoid heat source of Goldak, in which the parameters were calculated from microscopic observation of the cross-section of the weld pools. As for the mechanical analysis, it included non-linear geometry due to the deformation of the plate. Since the inertia was not relevant in the mechanical response, only the static stress was taken into consideration. The mechanical analysis was described by the static equilibrium in the Lagrangian reference frame (Equation 2.10):

$$\frac{\partial \sigma_{ij}}{\partial x_j} + B_i = 0 \quad (2.10)$$

where  $\sigma_{ij}$  is the Cauchy stress tensor and  $B_i$  is the sum of the body forces. The total strain vector (Equation 2.11) was decomposed in the following equation:

$$\varepsilon = \varepsilon_e + \varepsilon_p + \varepsilon_t \quad (2.11)$$

where  $\varepsilon_t$  is the thermal strain vector (Equation 2.12);  $\varepsilon_p$  is the plastic strain vector; and  $\varepsilon_e$  is the elastic strain vector.

$$\varepsilon_t = \alpha_t(T - T_{ref}) - \alpha_{T_0}(T_0 - T_{ref}) \quad (2.12)$$

where  $T$  is the temperature;  $\alpha_t$  and  $\alpha_{T_0}$  are the thermal expansion coefficients at the temperature  $T$  and  $T_0$ ; and  $T_{ref}$  is the reference temperature at which thermal strain is considered zero. The constitutive equation 2.13 was expressed as follows:

$$\sigma = D\varepsilon_e = D(\varepsilon - \varepsilon_p - \varepsilon_t) \quad (2.13)$$

where  $D$  is the material stiffness. The stresses were calculated with three different temperatures and strains rate with ABAQUS. The numerical solution was compared with a plate, which was semi-automated machine welded. The measurement of the residual stresses on the real weld was performed by hole drilling method. The comparison showed a reasonable correlation between the numerical simulation and the physical results.

The hole drilling method is a non-destructive method, similar to the strain gauge, but in this method a three-element strain gauge (Figure 2.15) rosette is installed in the component in the point where the residual stresses are calculated. When a hole is drilled and after the material is removed from the component, the material relaxes and the residual stresses are calculated [52].

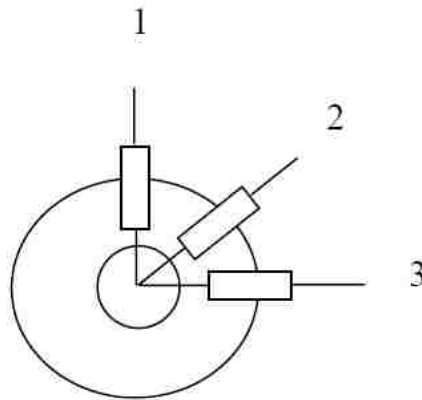


Figure 2.15- Strain gauge rosette [52]

In order to better simulate the residual stress prediction in the simulation, the birth-death element method can be introduced. An example can be shown in the study on the finite element analysis of a GMAW welding assembly of an auto-body steel panel and door hinge [8], where the moving heat source and the birth-death element method are adopted

in the coupled thermal-structural analysis in order to obtain the temperature and mechanical behaviour with ANSYS-ADPL.

The birth-death method was used to better simulate the deposition of the filler material and the pre-melting of the coating. It consisted of setting the initial nodes of the model with a status of deactivated as if they became dead. During the cycle of thermal analysis all nodes at first are applied with the boundary constraint temperature. As soon as deactivated elements or nodes are under the influence of the welding arc they are reactivated. In the structural analysis birth activation is dependent on the solidification temperature. The temperature decides if the elements can take part in the whole process or not. In addition in this study the galvanized coating surface was simulated using the birth-element method, so the status of the element was determined by its temperature. For example, if the surface element temperature is below the melting point of the galvanization layer, the element is a living one. When the temperature is higher, the elements are killed, so they do not have any influence on the calculation. The thermal and mechanical activation are separated. In this way the element can be heated but cannot contribute to the mechanical stiffness [53]. As a result this method showed good comparison with the physical weld.

For the simulation of the filler material, another method called “quiet elements”, can be used. In the previous method, the elements are activated during the whole analysis but they have been assigned with a low conductivity and stiffness [53], even though decreasing the stiffness too much can lead to ill-conditioned problems. The two methods of activation and deactivation were compared in the study of Lindgren et al. [54] and the two approaches gave similar results. However, the birth and death method is more accurate and more effective with respect to computational cost.

In the case of multi-pass welding, additional computations are needed. In the study of the residual stress distribution near weld start/end locations using GTAW [46], the strain components were calculated; also the longitudinal residual stress (Equation 2.14) and the transverse residual stress (Equation 2.15) were calculated with the following equations:

$$\sigma_L = -\frac{E}{1-\nu^2}(\varepsilon_L + \nu\varepsilon_T) \quad (2.14)$$



$$\sigma_T = -\frac{E}{1-\nu^2}(\varepsilon_T + \nu\varepsilon_L) \quad (2.15)$$

where E is the Young's Modulus;  $\nu$  is the Poisson's ratio; and  $\varepsilon_L$  and  $\varepsilon_T$  are the released strains in the longitudinal and transverse directions. In this study, the division in two steps (thermal analysis and mechanical analysis) previously discussed is maintained and the temperature histories obtained from the first step using Quick Welder are taken as thermal loads in the second step. The non-linear heat transfer analysis is used and the heat source was treated as a volumetric heat source. In this case, however, because more welding passes were present, the volumetric heat flux of each pass was introduced in equation 2.16:

$$q_i = \frac{\eta VI}{V_H} \quad (2.16)$$

where V is the arc voltage; I is the welding current;  $V_H$  is the volume of heat source; and  $\eta$  is the arc efficiency. The heating time can be calculated by equation 2.17:

$$t_h = \frac{L}{v_w n_d} \quad (2.17)$$

where L is the length of the weld seam;  $v_w$  is the welding speed of each weld pass; and  $n_d$  number of divisions in the welding direction. The heat losses and the total strain increment were taken into account using equations 2.5, 2.6 and 2.7. In this study, the plastic behaviour, a rate-independent plastic model and yield criterion of Von Mises surface were employed. The material strain-hardening behavior and bilinear isotropic models were considered with the following equation 2.18:

$$H' = \frac{d\sigma_Y}{d\varepsilon^p} \quad (2.18)$$

where  $d\sigma_Y$  is the increment of the yield strength and  $d\varepsilon^p$  is the increment of plastic strain.

A similar approach is found in a study on welding residual stress in a penetration nozzle [55]. Also in this case it is outlined the importance of the annealing temperature in the simulation. In case the temperature of the material exceeds the value of the annealing temperature, the material will lose all the strain-hardening. If the temperature is below the annealing temperature, the material can be work hardened again. In the studies [55] and [46] the comparison between simulation and experiment was favorable.

In order to find the residual stresses in the experiment, many methods were introduced, such as hole drilling (Section. 2.2.1), strain gauges, and x-ray diffraction.

As for the strain gauge method it is a non-destructive measurement method used to measure the level of strain on a surface in Figure 2.16. A common type of strain gauge consists of attaching a flexible foil on the surface. When the metal is deformed the resistance in the foil changes and the signal from the gauge is recorded.

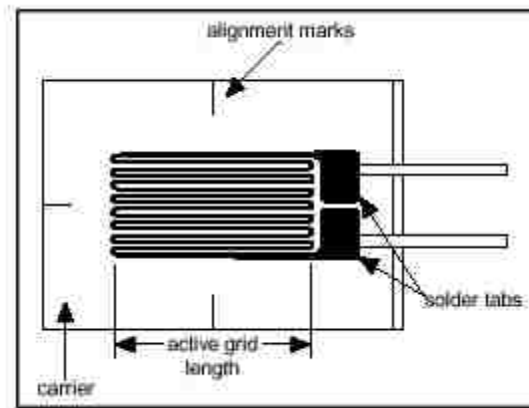


Figure 2.16- Bonded metallic strain gauge [56]

Another method used to calculate residual stresses is the X-ray diffraction which determines the lattice spacing [52] and compares it to an unstressed value.

## 2.2 Numerical approach

Considering all the distortion prediction approaches introduced in Section 1.2, the numerical approach demonstrated the best ability to simulate the complex coupling that characterizes arc weld distortion.

The first step in the transient analysis is to replicate the temperature history during the welding process. In order to do so, the energy heat input can be simulated taking into consideration the heat source models studied in Section 2.1.2.1. Phase transformation data and material properties are necessary to obtain a reliable thermal analysis. Once the temperature analysis is completed, coupling with the mechanical analysis can take place. In this way, the temperature history acts as an input for the mechanical analysis. The metallurgical study is considered during both thermal and mechanical analysis. As introduced in Section 1.2.1.1, different software are available for the transient analysis such as SysWeld, Abaqus, VrWeld, Ansys-Fea and LsDyna.

The shrinkage approach is the least complex among all the numerical approaches and it is based on elastic analysis. In linear elastic analysis, only the thermal and mechanical analyses are taken into consideration whereas some other welding processes are neglected, such as the welding speed and welding time.

The relationship between loading force and shrinkage deformation (Figure 2.17) in the simplified approach was proposed in the following equation 2.19 by Sulaiman et al. [21]:

$$\{x\} = [K]^{-1}\{F\} \quad (2.19)$$

where  $x$  is the shrinkage value( $mm$ ) and  $K$  is the equivalent shrinkage stiffness of the weld-affected zone ( $N/mm$ ).  $F$  is the equivalent shrinkage force ( $N$ ) which can be found with equation 2.20:

$$F = Eq \alpha / c\rho \quad (2.20)$$

where:

- $E$  is the elastic modulus( $N/mm^2$ );
- $q$  is the heat input per unit length( $J/mm$ );
- $\alpha$  is the thermal expansion coefficient( $^{\circ}C^{-1}$ );
- $c$  is the specific heat capacity ( $J/Kg^{\circ}C$ );
- $\rho$  is the density( $Kg/mm^3$ ).

Also the relationship between the distortion and the loading moment is introduced in equation 2.21:

$$\{\theta\} = [K]^{-1}\{M\} \quad (2.21)$$

where  $\theta$  is the angular distortion (*rad*), and  $M$  is the equivalent bending moment (*Nmm*).

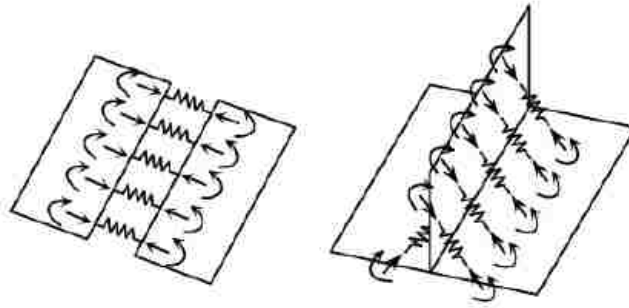


Figure 2.17-Models of shrinkage forces and moments for butt joint (left) and T-Joint (right) [21]

## CHAPTER 3

### EXPERIMENTAL SETUP

#### 3.1 Definition of geometry and welding process parameters

The geometry taken into consideration is the Tee-joint which is composed of Coupon #1 and Coupon #3 (Figure 3.1).

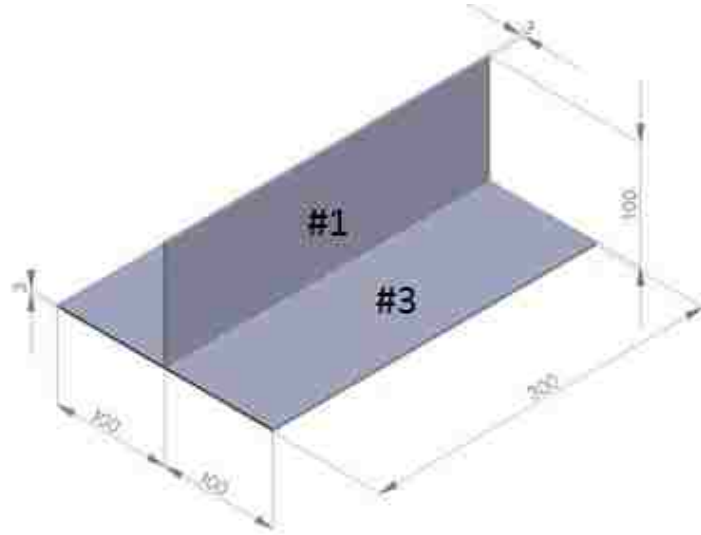


Figure 3.1- Tee joint geometry- measurements in mm

Dimensions of each coupon are reported in the Table 3.1:

	COUPON #1	COUPON #3
Length	300 mm	300 mm
Width	100 mm	200 mm
Thickness	3 mm	3 mm

Coupon #1 is available in two different materials MS 67 low-carbon, cold-rolled steel, and MS 264 050XK high-strength, low-alloy steel, Coupon #3 is made of MS 264 050XK high-strength, low alloy steel. MS 67 low-carbon, cold-rolled steel as per the Chrysler standard has to be compliant with the following chemical composition (Table 3.2) and minimum mechanical properties (Table 3.3).

**Table 3.2- Requirements for Chemical Composition(% by Mass) of MS 67**

<b>Carbon</b>	<b>Manganese</b>	<b>Phosphorus</b>	<b>Sulfur</b>
0.13 max	0.6 max	0.03 max	0.030 max

**Table 3.3- Minimum Mechanical properties of mild steels in transverse direction- Chrysler standard for MS 67**

<b>Tensile Strength (MPa)</b>	<b>Yield Strength (MPa)</b>	<b>Total Elongation (%)</b>
270-410	140-280	28

The High strength steel MS-264-050XK conforms to SAE-J1392. As for the chemical composition, there is not a specific requirement. It has to be compliant to the mechanical properties showed in Table 3.4.

**Table 3.4- Minimum Mechanical Properties of high strength steel MS 264 05 XK in transverse direction**

<b>Tensile Strength (MPa)</b>	<b>Yield Strength (MPa)</b>	<b>Total Elongation (%)</b>
414	345-449	22

GMAW was performed to join the two coupons by an automatic welding robot. The following process parameters in Table 3.5 were used. The chemical composition of the filler material can be found in the Appendix C.

**Table 3.5- Welding parameters**

<b>Arc Robot</b>	<b>FANUC ROBOT ARC MATE 120iC</b>
<b>Wire</b>	fabCOR F6 75% Ar/ 25% CO2
<b>Wire Diameter</b>	0.99 mm
<b>Wire feed speed</b>	8.89 m/min
<b>Travel speed</b>	10.58 mm/s
<b>Voltage</b>	20V
<b>Current</b>	160A

All the experimental procedures were carried in Chrysler facilities. Welding of the T-joint is performed with a single pass one side. Even though this is not the most common

procedure used in the T-joint, one welding pass is faster and it requires less setup time. Different clamping conditions are exploited as summarized in Table 3.6.

**Table 3.6- Materials and clamping condition used for the six tests**

<b>TEST #</b>	<b>COUPON #1</b>	<b>COUPON #3</b>	<b>CLAMPING CONDITION</b>
<b>TEST 1</b>	Mild steel	High strength steel	Fully clamped along the length
<b>TEST 2</b>	High strength steel	High strength steel	Fully clamped along the length
<b>TEST 3</b>	Mild steel	High strength steel	One clamp near each edge of one side of Coupon #3, one clamp near each edge of one side of coupon #1
<b>TEST 4</b>	High strength steel	High strength steel	One clamp near each edge of one side of Coupon #3, one clamp near each edge of one side of coupon #1
<b>TEST 5</b>	Mild steel	High strength steel	Fully clamped in z directions for coupon #3 and fully clamped in x direction for coupon #1 along the lengths
<b>TEST 6</b>	High strength steel	High strength steel	Fully clamped in z directions for coupon #3 and fully clamped in x direction for coupon #1 along the lengths

The setups for the T-joint are complex because no tacks are performed before the welding. In addition, the orthogonality between the two coupons is ensured by using a vertical level as shown in the following Figure 3.2.



**Figure 3.2-T-joint setup**

As soon as the welding process ends, the setup was removed, and the plates were cooled down to ambient temperature.

### **3.2 Distortion measurement**

The first step in calculating the distortion was to mark twelve points on Coupon #3 (Figure 3.3) and six points on Coupon #1 (in black in Figure 3.4). Once all the points have been identified, twelve distances can be measured with the use of a caliper as shown in red in Figure 3.4. In this way the measurements are not constrained to a fixed reference system and they can be compared to the results obtained with the simulations in the next chapter. In Figure 3.4, SW and EW stand respectively for start of welding and end of welding. Four lines can be identified along the same direction of the welding:

- Line A: Distances # 1-2-3:
- Line B: Distances # 4-5-6:
- Line C: Distances #7-8-9:
- Line D: Distances #10-11-12.



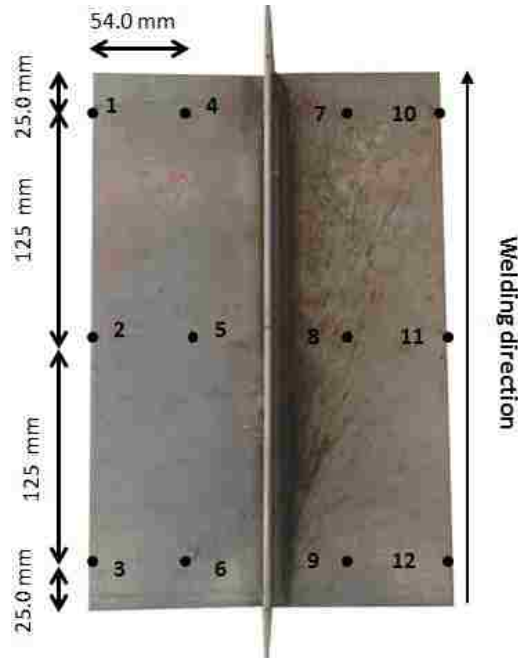


Figure 3.3- Position of 12 Points on Coupon#3-Top view

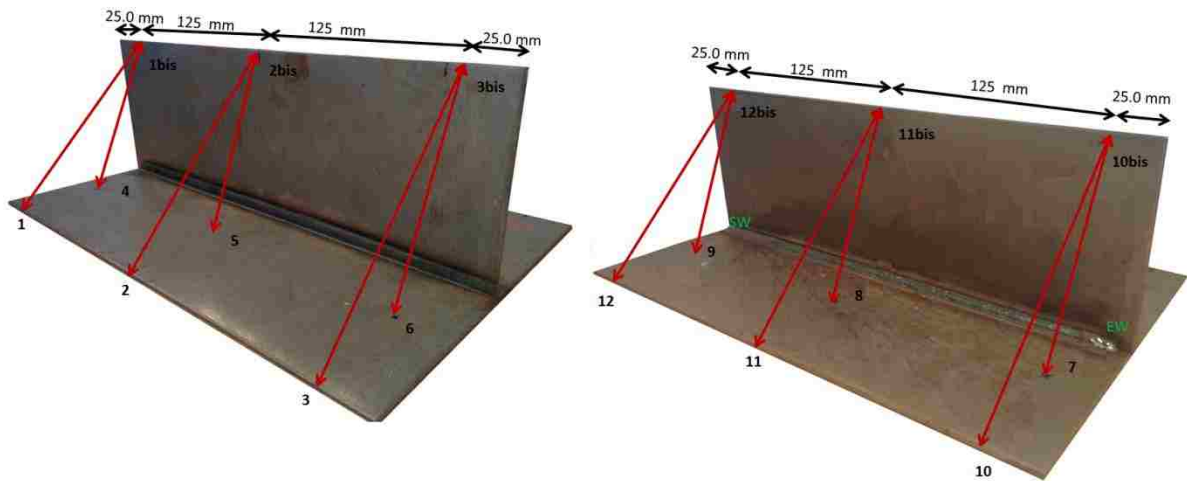


Figure 3.4-Position of the 6 points on Coupon #1 and 12 distances measured (in red)

### 3.3 Results and discussion

The twelve distances measured for each test are reported in Table 3.7. Before the welding process the distance # 1-2-3-10-11-12 was 140.36 mm, whereas the distance #4-5-6-7-8-9 was 109.45 mm.

Table 3.8 shows the displacement between the distance measurement before the welding process and the measurement after the welding process for all six tests.

The twelve distances measured for each test are reported in Table 3.7. Before the welding process the distance # 1-2-3-10-11-12 was 140.36 mm, whereas the distance #4-5-6-7-8-9 was 109.45 mm.

**Table 3.7-Distance results [mm] in experimental tests**

<b>Distance#</b>	<b>Test #1 Distance [mm]</b>	<b>Test #2 Distance [mm]</b>	<b>Test #3 Distance [mm]</b>	<b>Test #4 Distance [mm]</b>	<b>Test #5 Distance [mm]</b>	<b>Test #6 Distance [mm]</b>
<b>1</b>	139.92	139.99	139.8	140.13	139.85	140.06
<b>2</b>	139.88	139.73	139.84	140.11	139.94	140.03
<b>3</b>	139.52	139.88	139.77	140.52	139.87	139.96
<b>4</b>	108.96	108.97	108.96	109.09	108.86	109.12
<b>5</b>	108.69	108.9	108.97	109.06	108.99	109.09
<b>6</b>	108.83	108.76	108.98	109.02	109.07	109.08
<b>7</b>	109.18	109.15	108.54	108.63	108.67	108.64
<b>8</b>	109.36	109.19	108.7	108.72	108.77	108.73
<b>9</b>	109.32	109.17	108.73	108.94	109.11	108.87
<b>10</b>	140.65	140.33	139.33	139.11	139.33	139.16
<b>11</b>	140.49	140.41	139.4	139.01	139.78	139.78
<b>12</b>	140.52	140.34	139.81	139.07	139.99	139.94

**Table 3.8-Displacement [mm] in experimental tests**

<b>Displacement #</b>	<b>Test #1 Displacement [mm]</b>	<b>Test #2 Displacement [mm]</b>	<b>Test #3 Displacement [mm]</b>	<b>Test #4 Displacement [mm]</b>	<b>Test #5 Displacement [mm]</b>	<b>Test #6 Displacement [mm]</b>
<b>1</b>	0.44	0.37	0.56	0.23	0.51	0.30
<b>2</b>	0.48	0.63	0.52	0.25	0.42	0.33
<b>3</b>	0.84	0.48	0.59	-0.16	0.49	0.40
<b>4</b>	0.49	0.48	0.49	0.36	0.59	0.33
<b>5</b>	0.76	0.55	0.48	0.39	0.46	0.36
<b>6</b>	0.62	0.69	0.47	0.43	0.38	0.37
<b>7</b>	0.27	0.30	0.91	0.82	0.78	0.81
<b>8</b>	0.09	0.26	0.75	0.73	0.68	0.72
<b>9</b>	0.13	0.28	0.72	0.51	0.34	0.58
<b>10</b>	-0.29	0.03	1.03	1.25	1.03	1.20
<b>11</b>	-0.13	-0.05	0.96	1.35	0.58	0.58
<b>12</b>	-0.16	0.02	0.55	1.29	0.37	0.42

Figure 3.5, Figure 3.6 and Figure 3.7 display the trend of the displacement found for each distance. Taking into consideration the tests with the same clamping condition but with different materials, it can be observed that the tests that had same material in both

coupons showed a higher displacement in Line C and D, whereas they show a lower displacement in Lines A and B compared to tests with different coupon materials.

Error bars % are introduced in the following figures .Each error bar is related to single measurement.

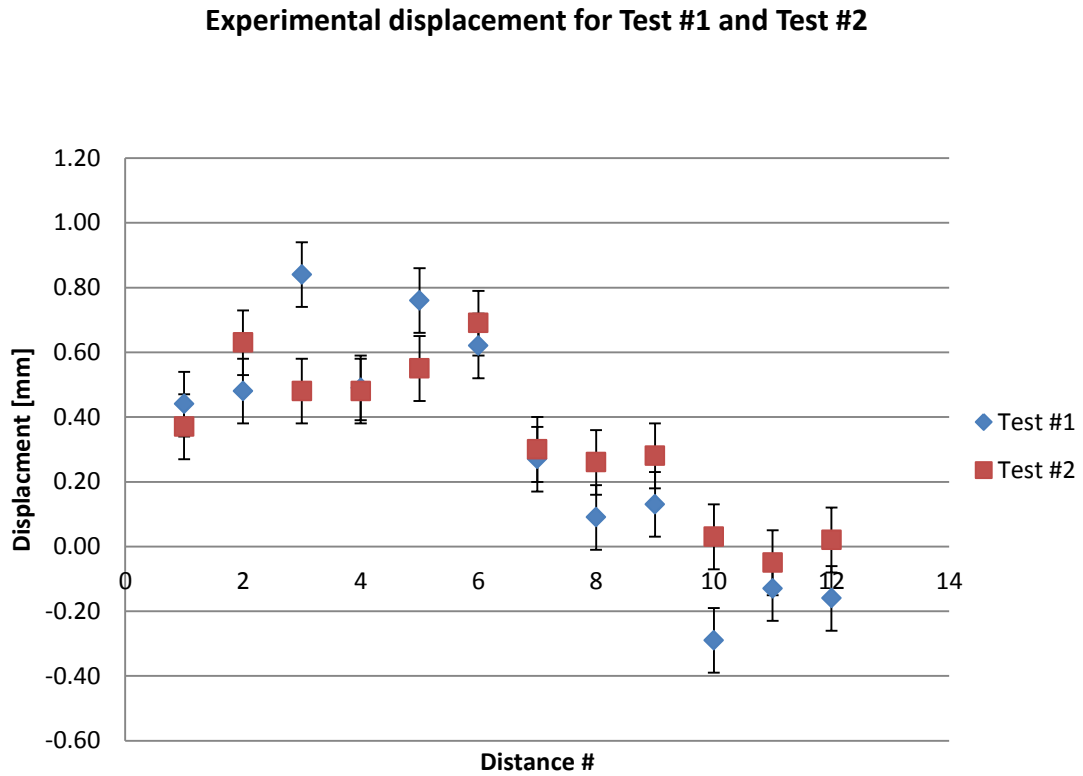


Figure 3.5-Experimental displacement [mm] for Test #1 and Test #2

Experimental displacement for Test #3 and Test #4

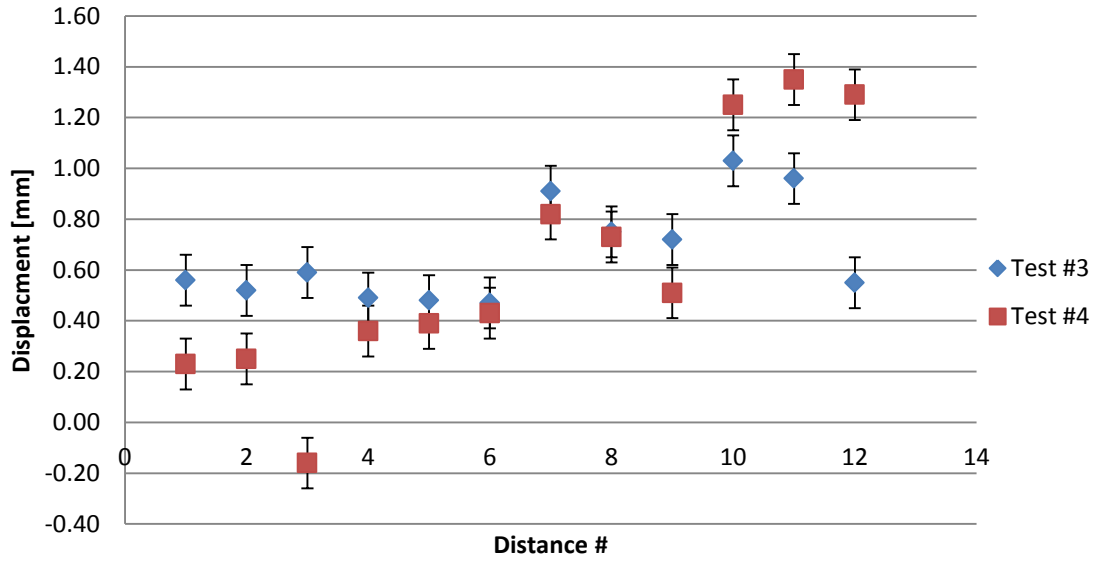


Figure 3.6- Experimental displacement [mm] for Test #3 and Test #4

Experimental displacement for Test #5 and Test #6

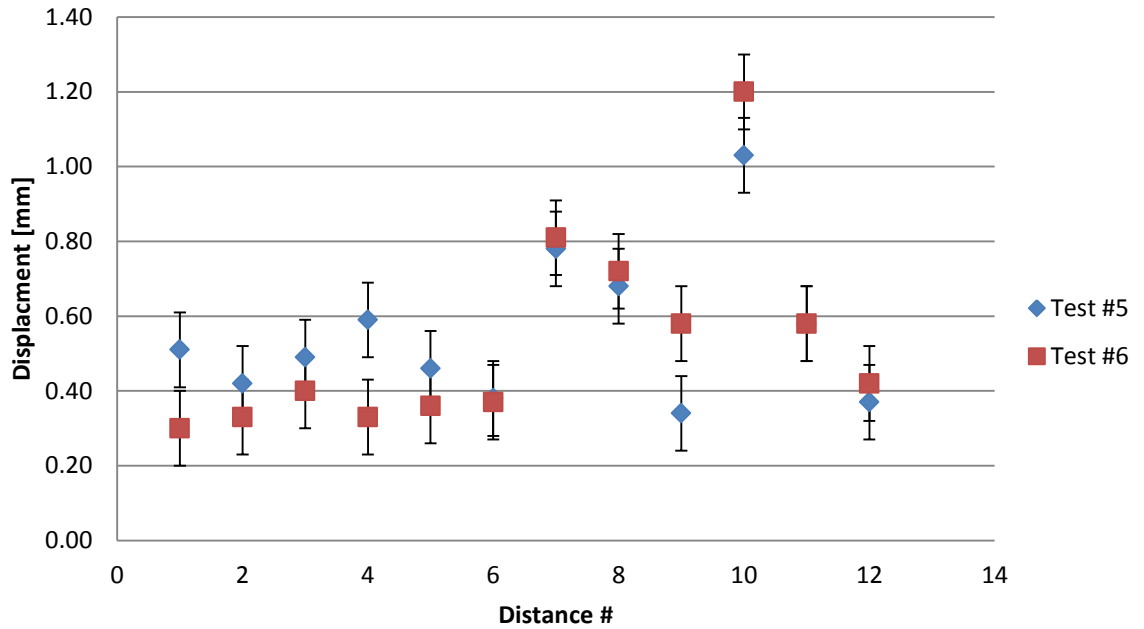


Figure 3.7- Experimental displacement [mm] for Test #5 and Test

## CHAPTER 4

### NUMERICAL SIMULATION OF ARC WELDING

After the review of all commercial software available, SYSWELD and WELD PLANNER have been chosen for this research. The main goal of this research is to provide a quick prediction of the weld distortions using numerical simulation for practical applications. The main objectives are to develop a model of distortion of arc welding, compare the distortion obtained in the two different simulation methods with experimental data, validate the model and minimize the distortion by varying some of the characteristic parameters of the welding process.

The following scheme explains the research workflow. The first step is the definition of the geometry and the welding parameters. The second step is the welding of the geometries for the experimental tests. The third is the simulation with SYSWELD and WELDPLANNER. The last step is the comparison of the results obtained with the simulations and experiments.

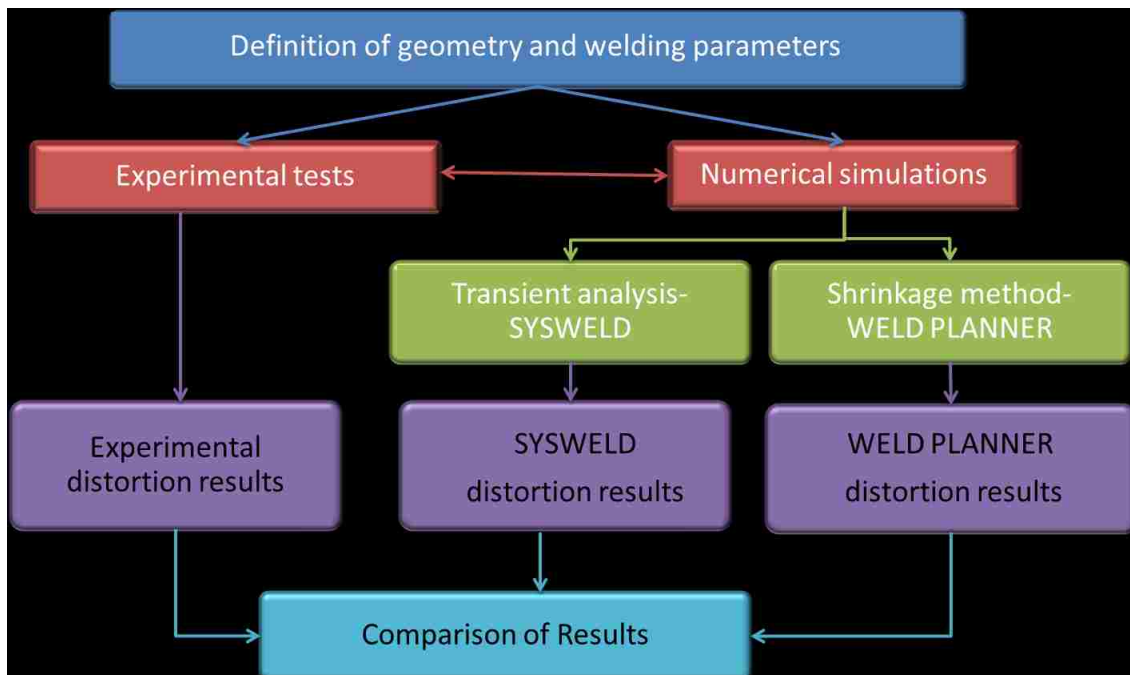


Figure 4.1- Workflow of the research

#### 4.1 Model development for Transient analysis-SYSWELD

The geometry of the T-joint for transient analysis is shown in Figure 4.2. The deposition of the filler material was taken into consideration, and the dimensions were reproduced using the data obtained from the test section shown in Figure 4.3.

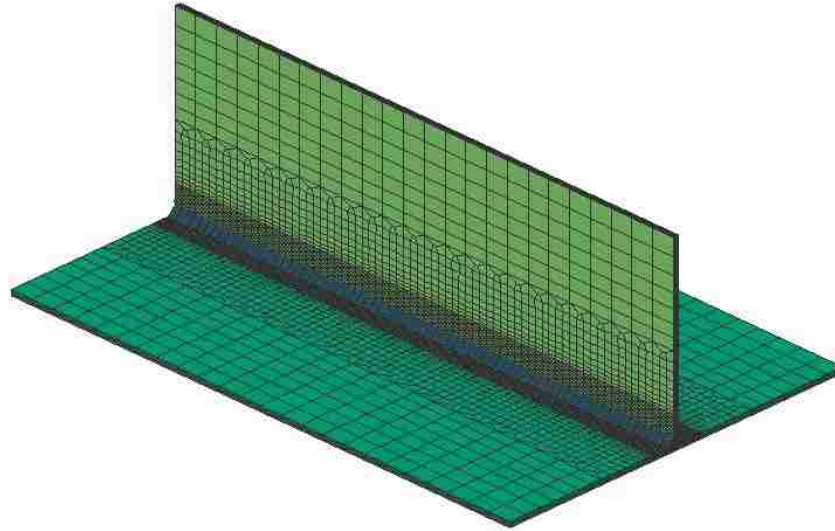


Figure 4.2- T-joint mesh for transient analysis



Figure 4.3- Software section (left) and real section (right) of the T-joint for transient analysis

The number of 3D elements required for the T-joint model for transient analysis was 27504.

Material definitions are applied to every component that has been created in the geometry. Materials are assigned using a designated database provided by the solver. Different material can be assigned for the component and the filler. S355J2G3 and DC 04

material were used in these simulations and they were chosen considering the materials used in the experimental tests.

These materials are already present in the software database. Chemical composition and minimum mechanical properties for these materials are listed in the following tables.

**Table 4.1- Chemical composition (%by mass) of low carbon steel S355J2G3-EN 10025 [21]**

<b>Carbon</b>	<b>Manganese</b>	<b>Phosphorus</b>	<b>Sulfur</b>
0.2 max	1.6 max	0.035 max	0.035 max

**Table 4.2-Minimum Mechanical Properties of S355J2G3 (EN 10025) or st52(DIN 17100) [21] [57]**

<b>Tensile Strength (MPa)</b>	<b>Yield Strength (MPa)</b>	<b>Total Elongation (%)</b>	<b>Poisson's ratio</b>	<b>Modulus of elasticity (GPa)</b>
485	355	20%	0.33	210

**Table 4.3-Chemical composition (% by mass) for plain carbon steel DC 04-AISI 1006 [58]**

<b>Carbon</b>	<b>Manganese</b>	<b>Phosphorus</b>	<b>Sulfur</b>
0.08	0.25-0.4 max	0.04 max	0.05 max

**Table 4.4-Minimum Mechanical properties of DC 04-AISI 1006**

<b>Tensile Strength (MPa)</b>	<b>Yield Strength (MPa)</b>	<b>Total Elongation (%)</b>	<b>Poisson's ratio</b>	<b>Modulus of elasticity (GPa)</b>
330	285	20%	0.29	205

As highlighted in Section 2.1.2.1, changes in thermal properties need to be taken into consideration in the transient analysis due to the non-linearity of the process and the phase-dependent physical properties.

Moreover, it is necessary to define the parameters of heat source. The estimated length, width and penetration of the heat source can be deduced from the weld pool study of a section of the welded part introduced in Figure 4.3. The parameters for the heat source of the T-joints are described in Table 4.5.

**Table 4.5- Heat source parameters used in the simulations**

<b>Parameter</b>	<b>Value</b>
Length	11.30 mm
Width	5.65 mm
Penetration	3.00 mm
Energy/length	302 J/mm

The length, width and penetration of the heat source are compliant with the Goldak double ellipsoid (Section 2.1.2.1 and Appendix A).

One of the main problems in the transient analysis of a welding process is the heat transfer from the weld plate to the surrounding environment. It is possible to create a 3D skin on the geometry that exchanges heat with the outside environment. The 3D skin generated for the T-joint is shown in Figure 4.4.

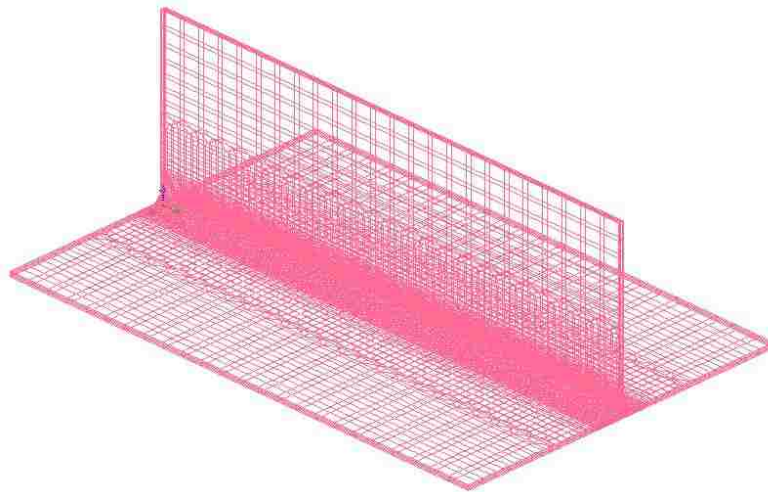


**Figure 4.4- 3D skin for cooling condition**

Also the time and position of the clamps need to be introduced. For the considered systems, only rigid clamps in all directions and unclamped boundary conditions were used. The position of the clamps reflects the experimental setup. An example for Test #3 and Test #4 is shown in Figure 4.5. The clamps were held for 45 seconds. The chosen time was an approximation due to the fact that the setup required different amount of



time for each of the six configurations. The unclamped condition was simulated for 1800 seconds. This amount of time was required in order to allow the plate to reach the ambient temperature.

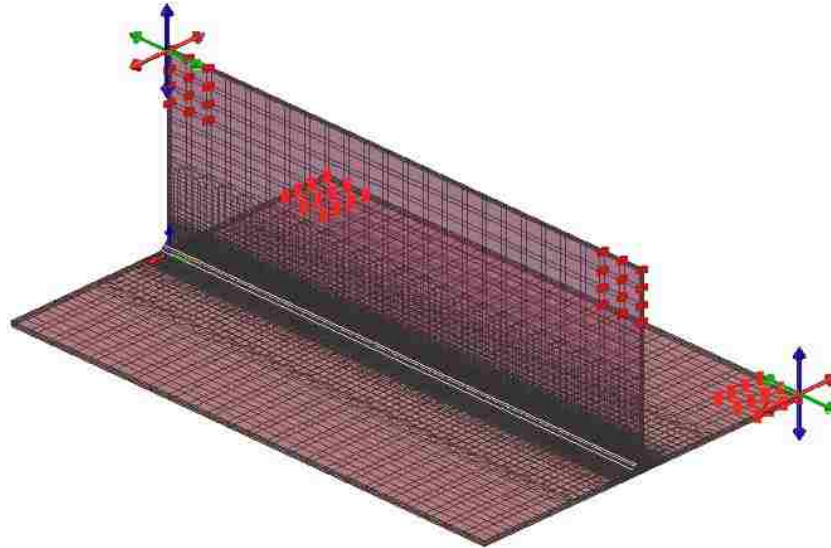


Figure 4.5-Position of the clamps for simulation Test#3 and Test #4

## 4.2 Model development for Shrinkage method-WELD PLANNER

The main goal of Weld Planner is to reduce the time for the simulation, which it is one of the problems of the transient analysis. For this reason, the geometries are built with shell elements, so that also the time for prototyping is remarkably decreased.

The T-joint for the shrinkage method was modeled as in Figure 4.6 with 7056 total number of shell elements. The materials used for the shrinkage method are S355J2G3 and DC 04, the chemical composition and minimum mechanical properties have been already introduced in the previous section.

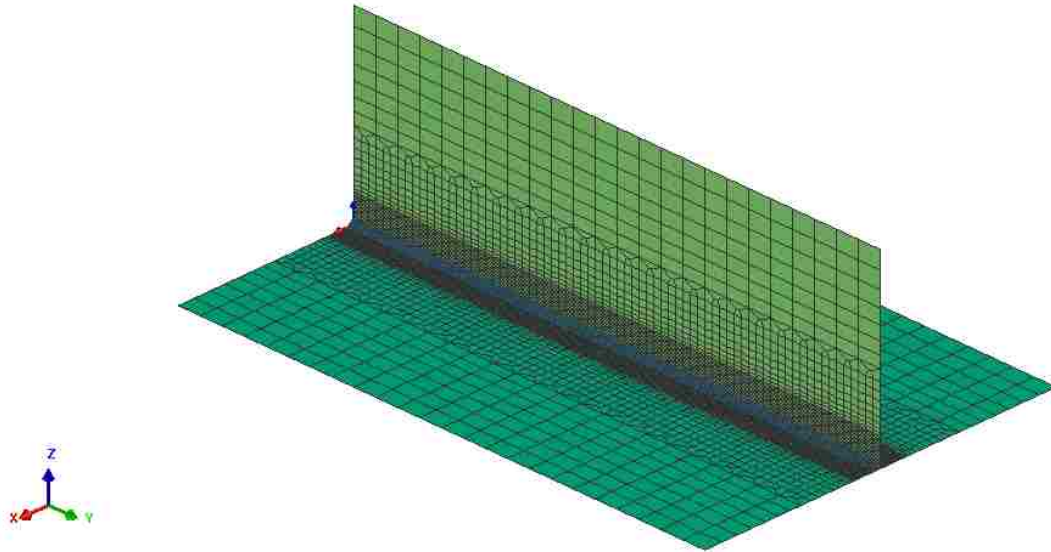


Figure 4.6- T-joint mesh for controlled clamping condition

The weld bead has a significant role in the distortion of the weld specimens, so it is necessary to calibrate the T-joint geometry considering the section of the weld pool as shown in Figure 4.7. In the six simulations, the arc bead width (Appendix B) is set to 6 mm.

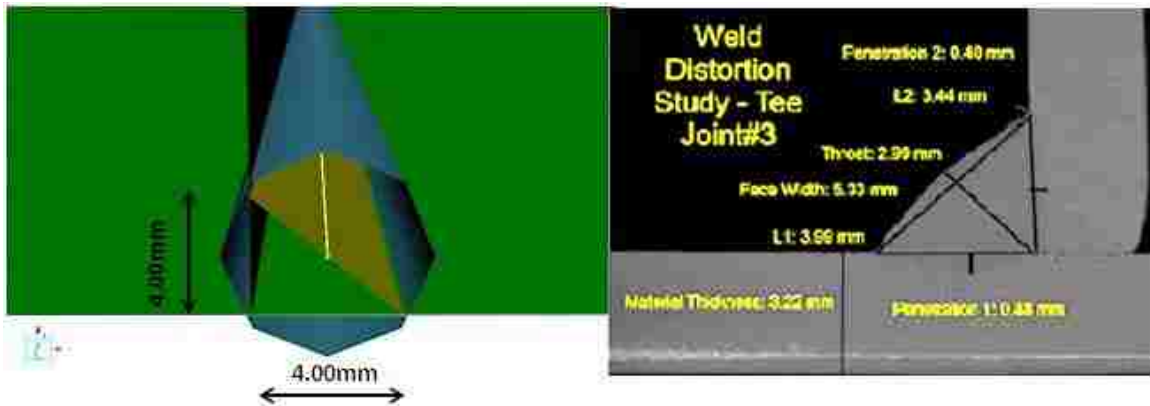


Figure 4.7- T-joint filler geometry in WELD PLANNER

The weld plan is divided into two steps. In the first step the weld takes place and in the same time the clamps are positioned. In the second step no weld happens, but the clamps remain in position. Examples of the clamping condition simulated and the weld plans for Test #3 and Test #4 are shown in Figure 4.8 and Figure 4.9.

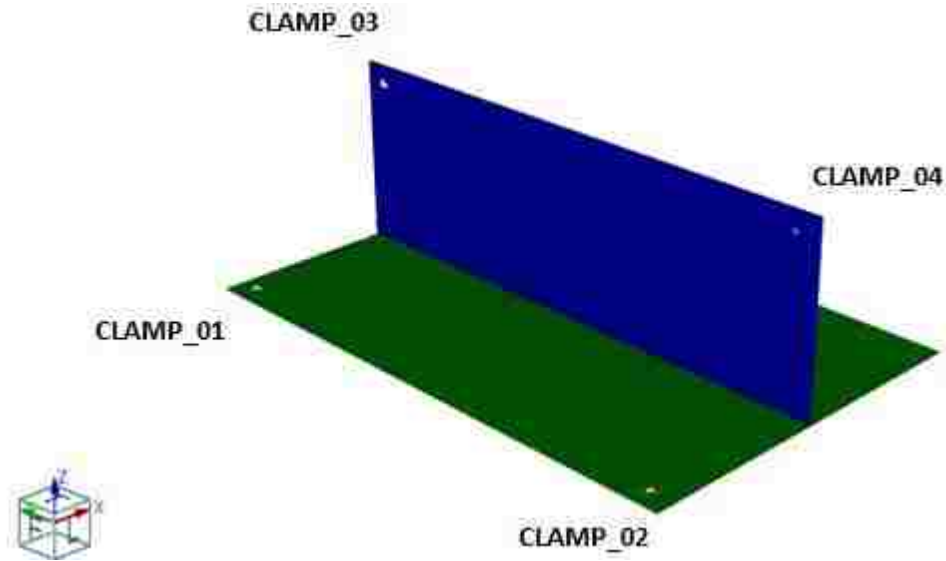


Figure 4.8-Clamping condition for Test #3 WELD PLANNER

Objects	c	#	Steps		
			1	2	3
JOINT_01		1	1	0	0
CLAMP_01		1			
CLAMP_02		2			
CLAMP_03		2			
CLAMP_04		2			

Figure 4.9- Weld Plan T-joint for simulation Test #3 and Test#4 in WELD PLANNER

### 4.3 Results and discussions for transient analysis-SYSWELD

The results from the simulations were collected measuring the twelve distances (Figure 3.4) introduced in Section 3.2. Then, the relative displacements are calculated between these distances before the welding process and after the simulation.

The simulation of the T-joint Test #1 showed the following displacement in Table 4.6. In the following table the first column shows the number of the distance used to calculate the distortion, the second column shows the value of each distance obtained with the software at the end of the arc welding process, and the third column presents the simulation displacements. The same type of table will be used to present the results for the other tests.

**Table 4.6-Simulation measurement [mm] and displacement [mm] results for T-joint Test #1**

Test 1		
Distance #	Simulation distance measurement [mm]	Simulation Displacement [mm]
1	139.63	0.73
2	139.70	0.66
3	139.65	0.71
4	108.80	0.65
5	108.83	0.62
6	108.82	0.63
7	109.29	0.16
8	109.32	0.13
9	109.29	0.16
10	140.49	-0.13
11	140.55	-0.19
12	140.50	-0.14

In the following Figure 4.10, the displacement trend in z direction is presented, the negative value of the displacements are due to the fact that in the simulation the T-joint was not constrained to any reference systems for a certain period of time. Maximum displacement can be found on the side opposite to where the weld took place.

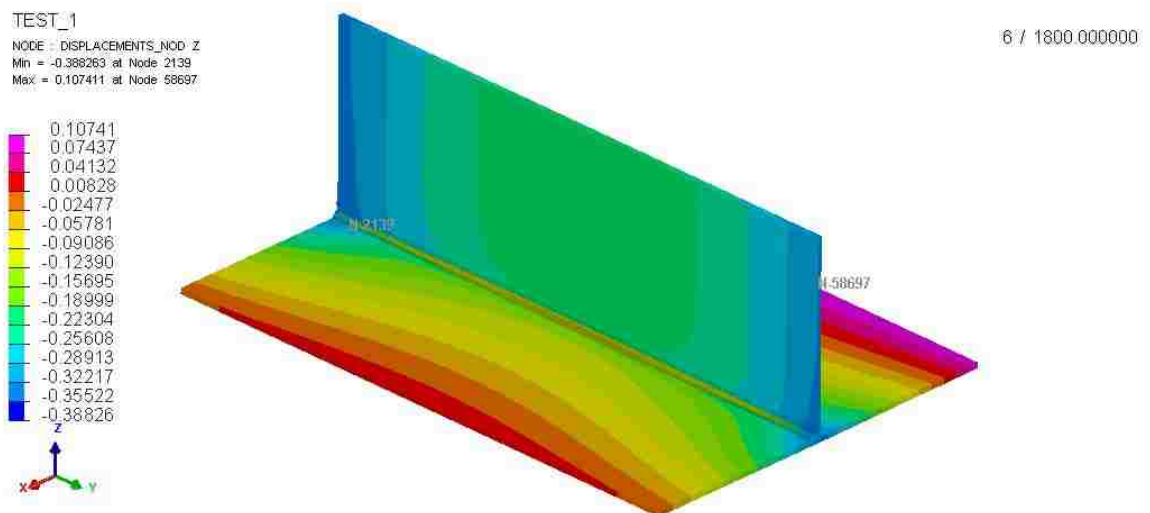


**Figure 4.10-Displacement [mm] trend in z-direction obtained with transient analysis for T-joint Test #1**

Von Mises Stress (Figure 4.11) is higher near the welded area with a maximum value of 629 MPa, whereas the areas far from the arc bead showed really low values of Von Mises stress after the welding process. The maximum value of Von Mises stress found in the

simulation is higher than the yield strength because, after the welding process, ferrite and pearlite partially transform into martensite. The formation of martensite leads to a stronger weld bead.

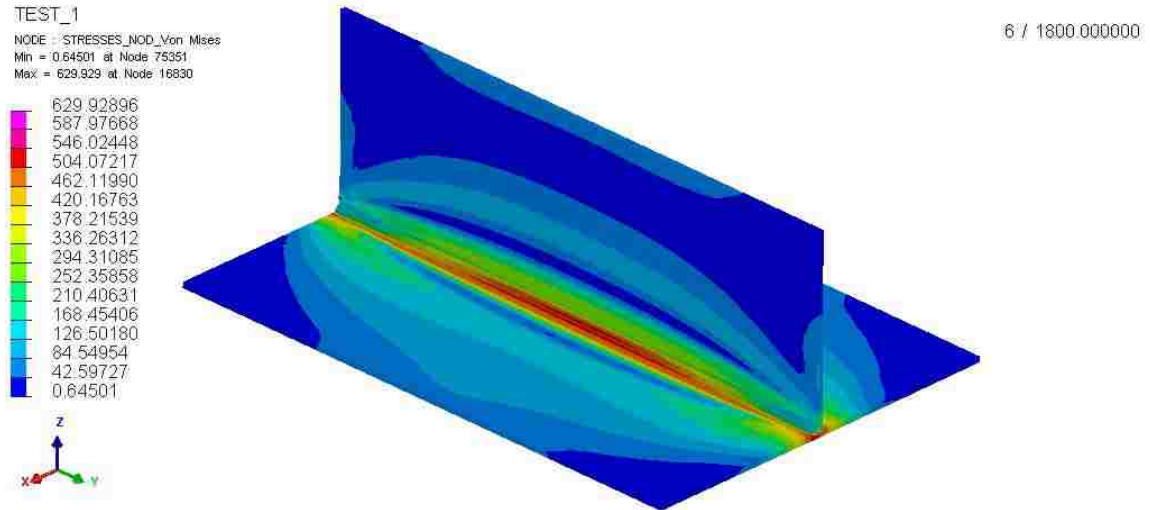


Figure 4.11-Von Mises stress [MPa] trend obtained with transient analysis for T-joint Test #1

As for T-joint Test #2, the following displacements in Table 4.7 have been found. The highest displacements are found in Line A and Line B.

Table 4.7- Simulation measurement [mm] and displacement [mm] results for T-joint Test #2

Test 2		
Distance #	Simulation distance measurement [mm]	Simulation Displacement [mm]
1	139.85	0.51
2	139.88	0.48
3	139.83	0.53
4	108.94	0.51
5	108.95	0.50
6	108.93	0.52
7	109.17	0.28
8	109.22	0.23
9	109.20	0.25
10	140.31	0.05
11	140.40	-0.04
12	140.35	0.01

Also in this case, the displacement in the z direction is higher on the side of Coupon #3 opposite to where the weld took place as shown in Figure 4.12. This displacement trend is very similar to the one found for Test #1

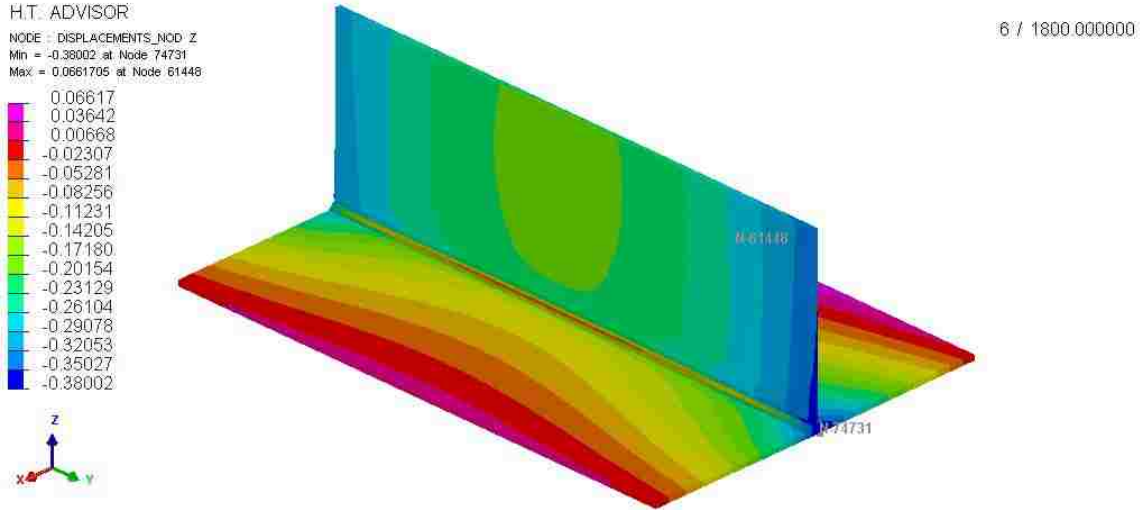


Figure 4.12- Displacement [mm] trend in z-direction obtained with transient analysis for T-joint Test #2

The maximum Von Mises stress found in the simulation for Test #2 is 627 MPa in the arc bead as shown in Figure 4.13.

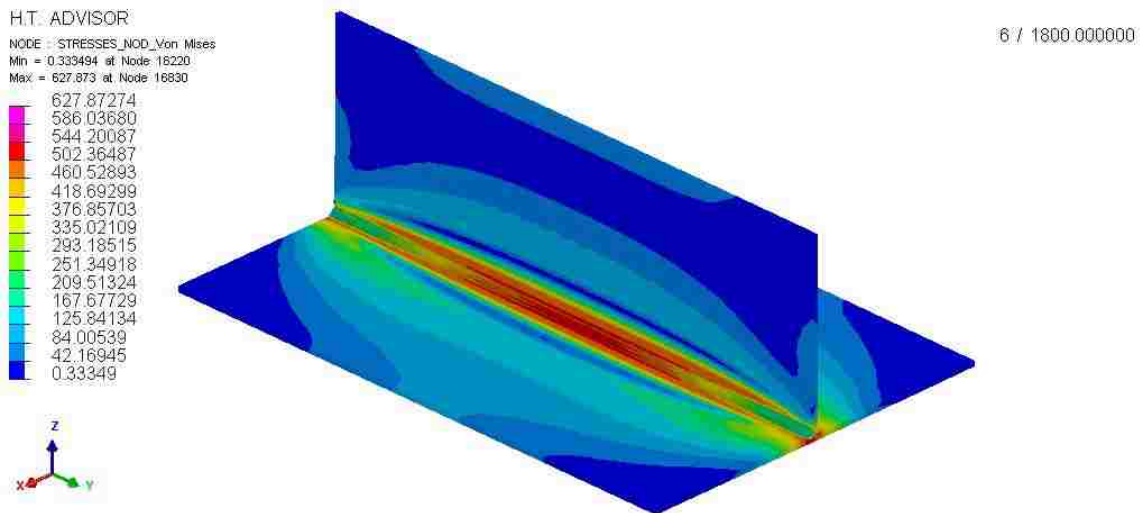


Figure 4.13- Von Mises Stress [MPa] trend obtained with transient analysis for T-joint Test #2

Displacement results from the simulation Test #3 are reported in Table 4.8. The maximum displacement has been recorded for Distance #10, whereas the minimum displacement has been found for Distance #6.

**Table 4.8- Simulation measurement [mm] and displacement [mm] results for T-joint Test #3**

Test 3		
Points	Simulation distance measurement [mm]	Simulation Displacement [mm]
1	139.69	0.67
2	139.72	0.64
3	139.71	0.65
4	108.83	0.62
5	108.84	0.61
6	109.15	0.30
7	108.81	0.64
8	108.92	0.53
9	108.97	0.48
10	139.66	0.70
11	139.84	0.52
12	139.91	0.45

The displacement trend in z-direction is shown in Figure 4.14. The displacement in Coupon #1 is completely different between Test #1 and Test #2 due to different clamping conditions.

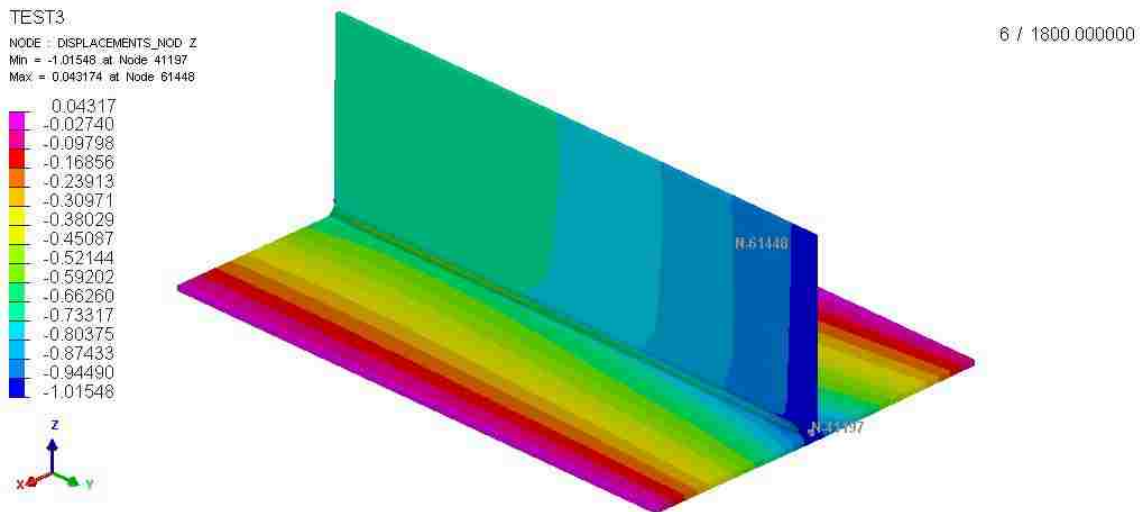


**Figure 4.14- Displacement [mm] trend in z-direction obtained with transient analysis for T-joint Test #3**

The maximum Von Mises stress is 632 MPa as shown in Figure 4.15. The lowest value of the stress can be found at the edge of each coupon.

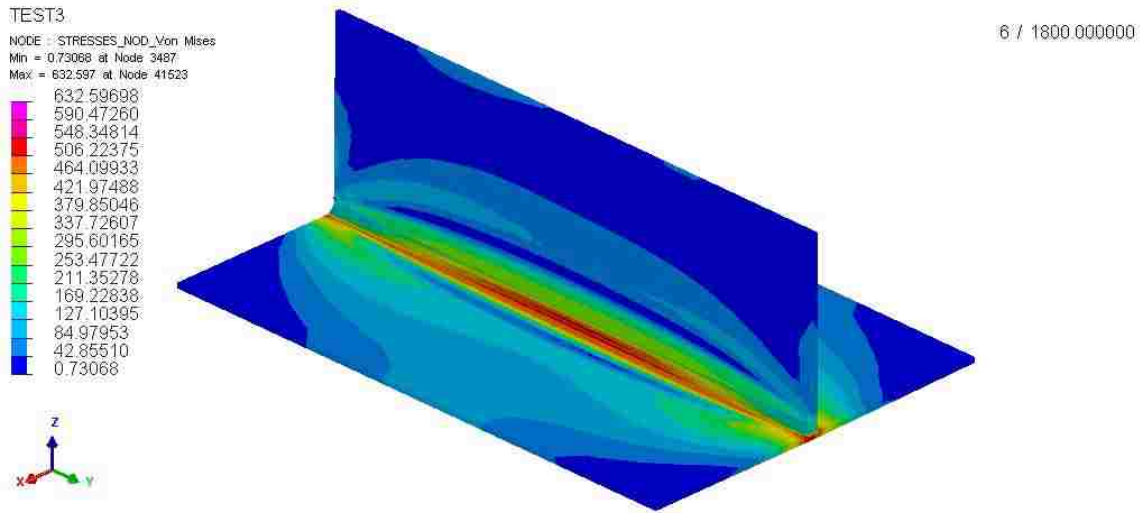


Figure 4.15- Von Mises Stress [MPa] trend obtained with transient analysis for T-joint Test #3

Simulation displacements for T-joint test #4 are reported in Table 4.9. The maximum values of displacement are found in Line D, which contains Distance #10-11-12. That side of the T-joint was not clamped during the welding process. The highest value of distortion among all the six tests is found in this simulation for Distance #10. The displacement trend in the z direction is shown in Figure 4.16.

Table 4.9- Simulation measurement [mm] and displacement [mm] results for T-joint Test #4

Test 4		
Distance #	Simulation distance measurement [mm]	Simulation Displacement [mm]
1	140.02	0.34
2	140.02	0.34
3	140.47	-0.11
4	109.04	0.41
5	109.03	0.42
6	109.00	0.45
7	108.40	1.05
8	108.63	0.82
9	109.00	0.45
10	138.95	1.41
11	139.34	1.02
12	139.52	0.84



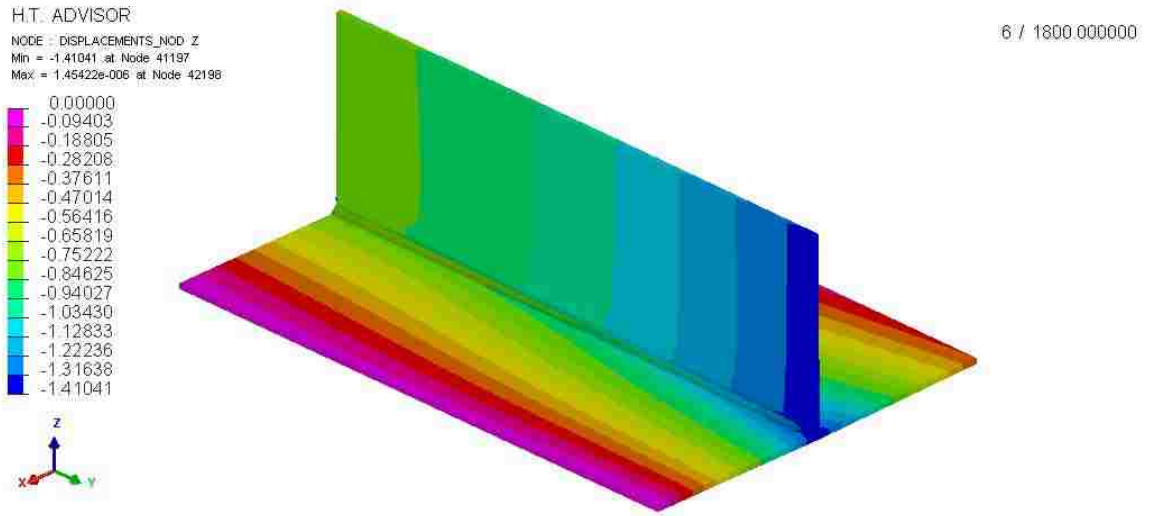


**Figure 4.16- Displacement [mm] trend in z-direction obtained with transient analysis for T-joint Test #4**

The Von Mises stress distribution for simulation Test #4 is shown in Figure 4.17. The maximum value recorded is 630 MPa.

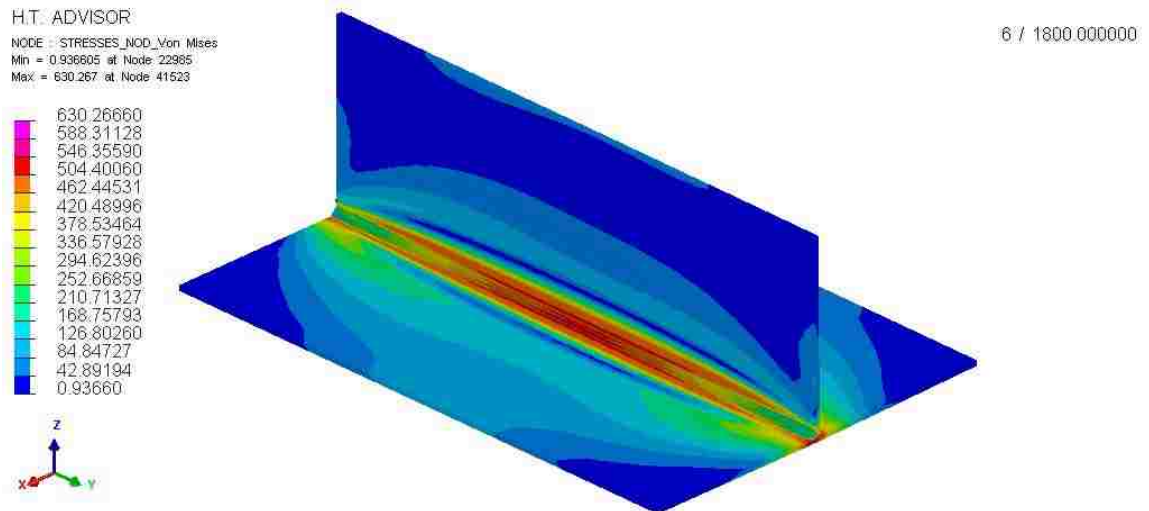


**Figure 4.17- Von Mises Stress [MPa] trend obtained with transient analysis for T-joint Test #4**

The simulation of T-joint Test #5 showed the displacements noted in Table 4.10. Also in this case the highest value of displacement is found in Line D; in particular the displacement of distance #10 is 0.74 mm.

**Table 4.10- Simulation measurement [mm] and displacement [mm] results for T-joint Test #5**

<b>Test 5</b>			
<b>Points</b>	<b>Simulation distance measurement [mm]</b>	<b>Simulation Displacement [mm]</b>	
<b>1</b>	139.72	0.64	
<b>2</b>	139.76	0.60	
<b>3</b>	139.72	0.64	
<b>4</b>	108.85	0.60	
<b>5</b>	108.87	0.58	
<b>6</b>	108.86	0.59	
<b>7</b>	108.76	0.69	
<b>8</b>	108.93	0.52	
<b>9</b>	108.96	0.49	
<b>10</b>	139.62	0.74	
<b>11</b>	139.86	0.50	
<b>12</b>	139.90	0.46	

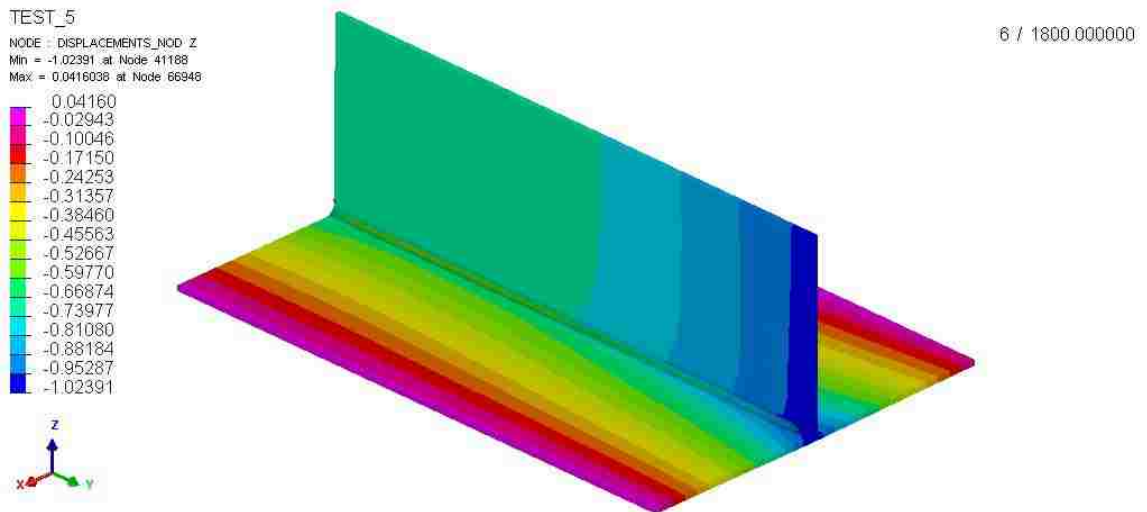


**Figure 4.18- Displacement [mm] trend in z-direction obtained with transient analysis for T-joint Test #5**

The maximum Von Mises stress in this test is 628 MPa after arc welding as shown in Figure 4.19. It is interesting to note that on the upper part of Coupon #1 there are some residual stresses due to the clamping condition on that part, similar to these in Test #1 and Test #2.

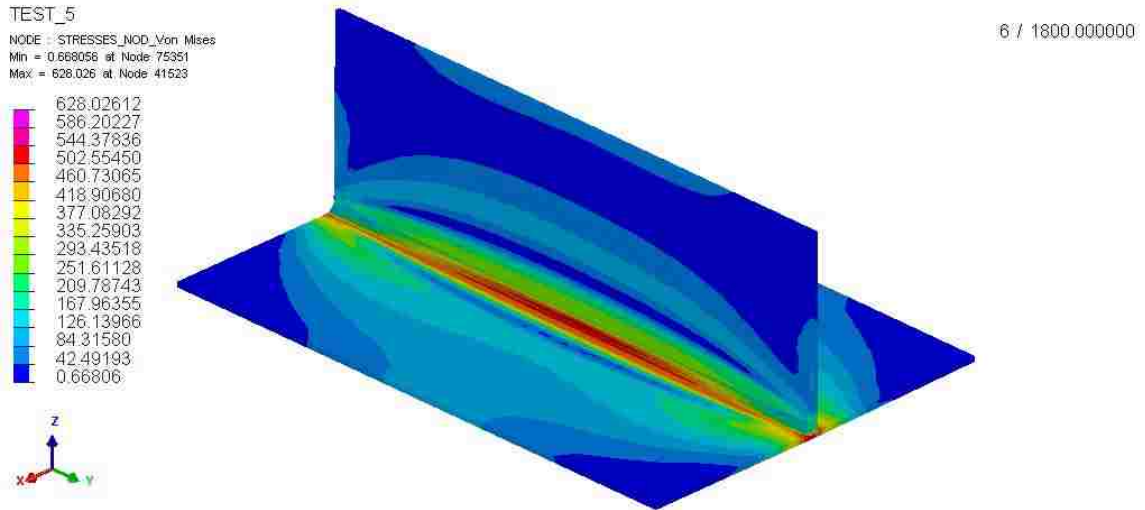


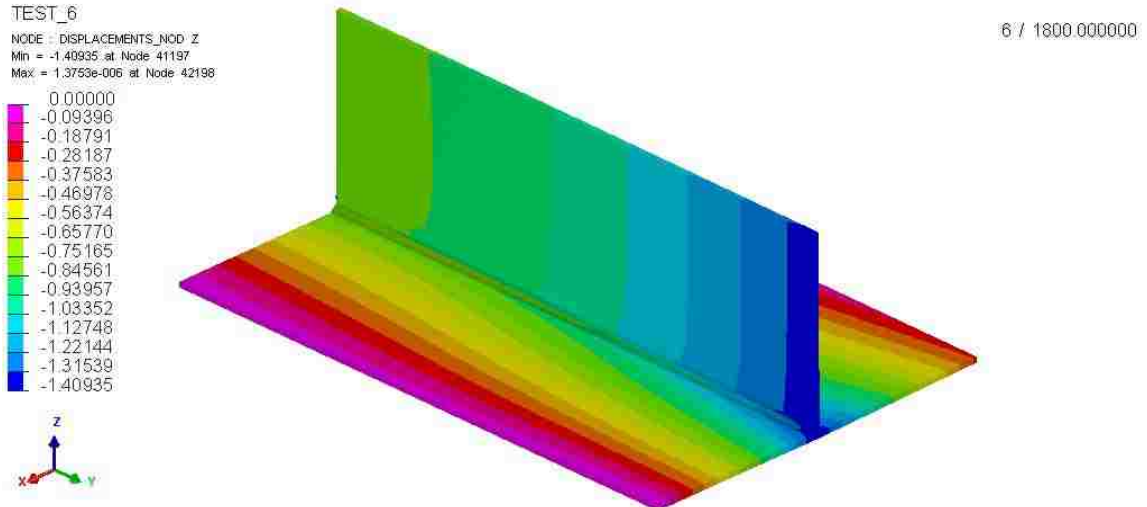
Figure 4.19- Von Mises Stress [MPa] trend obtained with transient analysis for T-joint Test #5

Table 4.11 shows the simulation measurements and displacements for Test #6. Maximum displacements are recorded, also in this case, in Line D and Line C.

Table 4.11- Simulation measurement [mm] and displacement [mm] results for T-joint Test #6

Test 6		
Points	Simulation distance measurement [mm]	Simulation Displacement [mm]
1	139.98	0.38
2	139.96	0.40
3	139.90	0.46
4	109.01	0.44
5	109.00	0.45
6	108.98	0.47
7	108.43	1.02
8	108.68	0.77
9	108.76	0.69
10	139.01	1.35
11	139.41	0.95
12	139.56	0.80

The displacement trend for the simulation of the T-joint in Test#6 is shown in Figure 4.20; the Von Mises stress distribution is displayed in Figure 4.21. The maximum value of stress is 624 MPa in proximity of the weld bead.



**Figure 4.20- Displacement [mm] trend in z-direction obtained with transient analysis for T-joint Test #6**

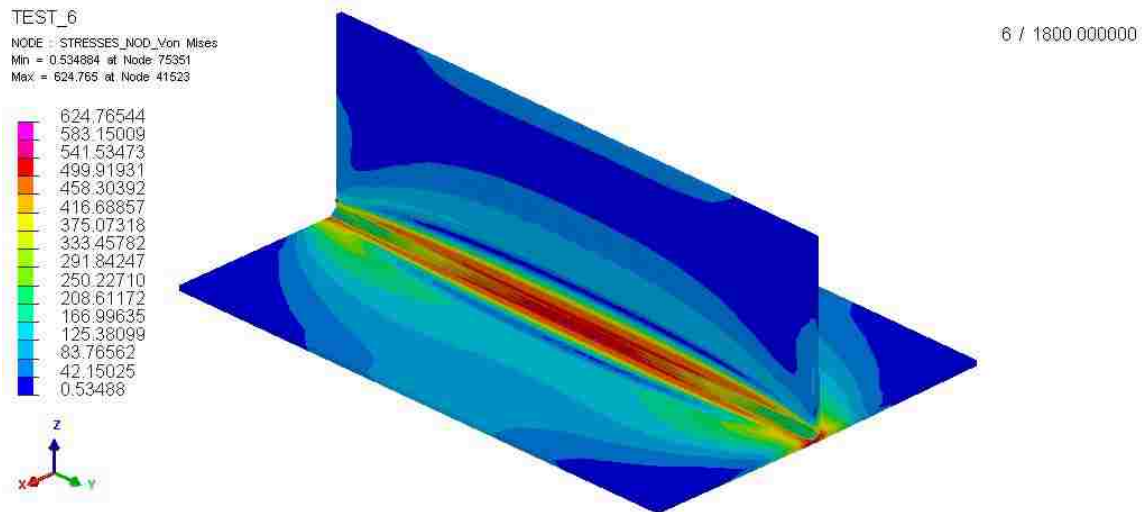


**Figure 4.21- Von Mises Stress [MPa] trend obtained with transient analysis for T-joint Test #6**

It is interesting to compare the displacements obtained with the simulation for the tests that had the same clamping condition but different Coupon #1 material. It can be observed from Figure 4.22, Figure 4.23 and Figure 4.24 that for Line A and B the distortion is higher in the tests that have structural steel as Coupon #3 and low carbon steel as Coupon #1. The opposite behavior can be found for Line C and Line D. It can be concluded that the difference in material has an impact on the final displacement for the same clamping condition. It reveals that thermal properties and final microstructure influenced the final distortion.

## Comparison between Test #1 and Test #2

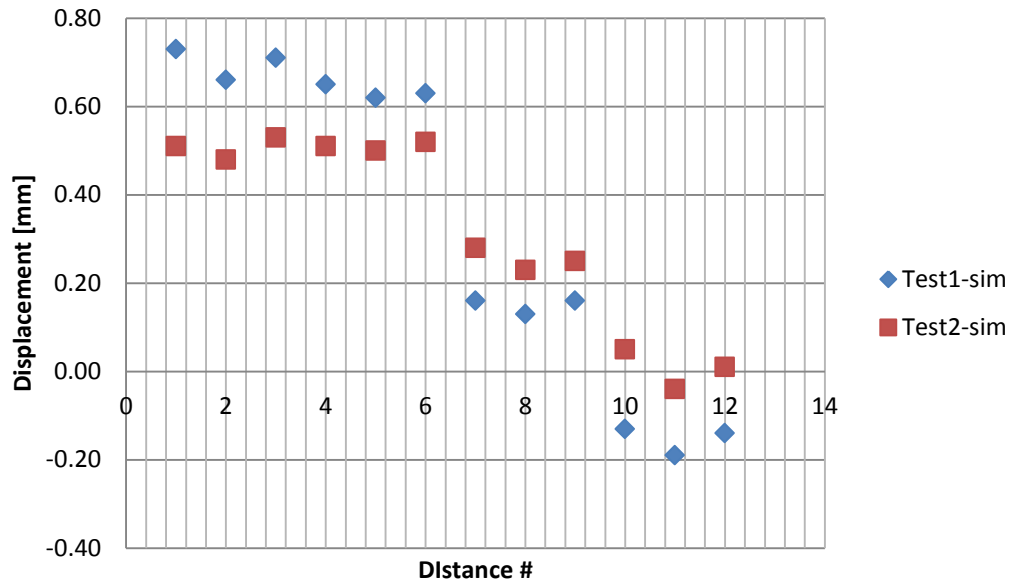


Figure 4.22-Comparison between simulation displacements between Test #1 and Test #2

## Comparison between Test #3 and Test #4

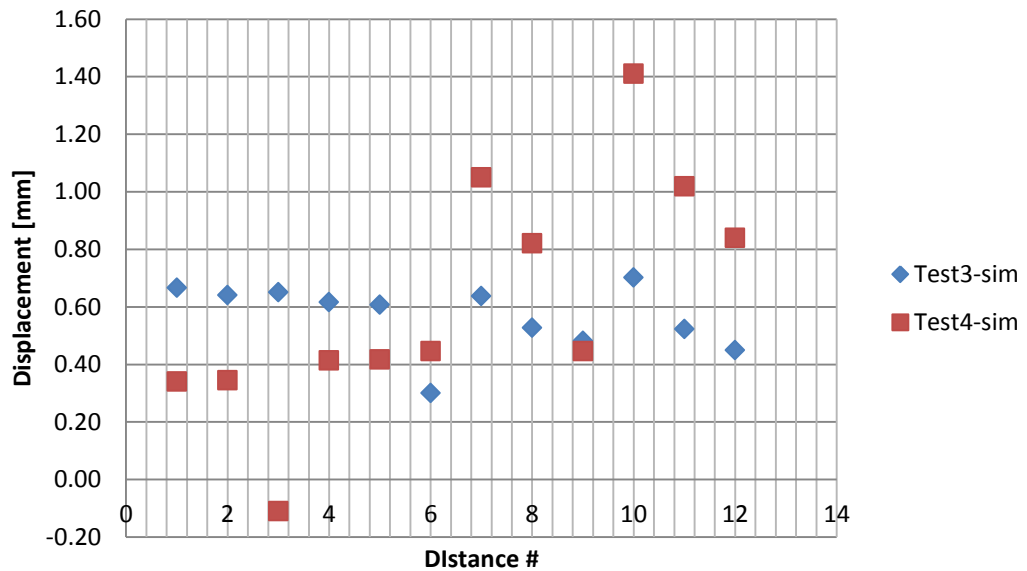


Figure 4.23- Comparison between simulation displacements between Test #3 and Test #4

## Comparison between Test #5 and Test #6

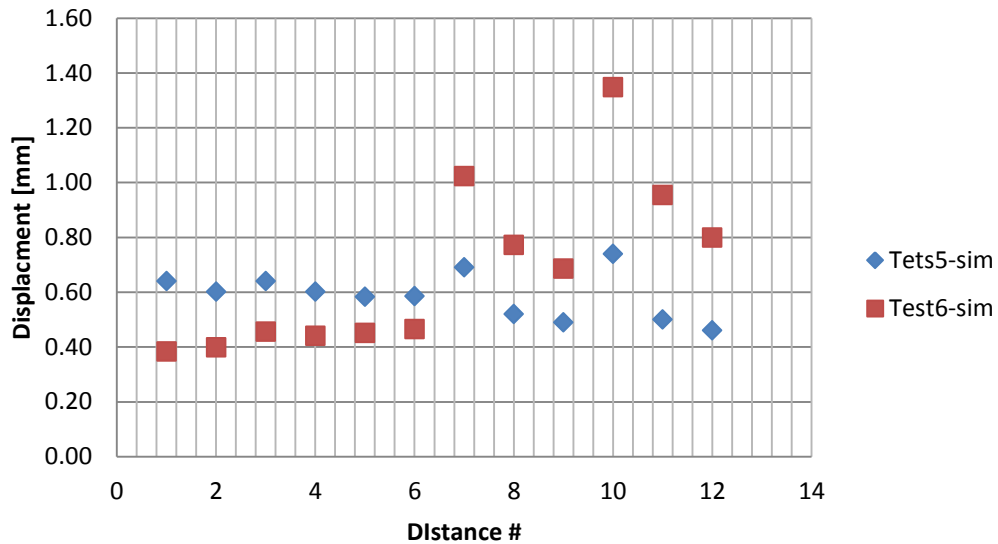


Figure 4.24- Comparison between simulation displacements between Test #5 and Test #6

After analyzing all the displacement results, the maximum value of Von Mises stress is studied among the six tests as shown in Table 4.12. The average maximum value of stress is 628.33 MPa and a standard deviation of 2.49 MPa.

Table 4.12- Von Mises stress [MPa] among the six tests and relative average value and standard deviation

	Test 1	Test 2	Test 3	Test 4	Test 5	Test 6	Average value	Standard deviation
<b>Von Mises Stress [MPa]</b>	629	627	632	630	628	624	628.33	2.49

### 4.4 Results and discussion for shrinkage method- WELD PLANNER

The main problem that has been encountered in WELD PLANNER is that not all clamping conditions can be simulated. In particular, the unclamped condition that characterizes the experimental tests could not be simulated properly by WELD PLANNER. This concern can be addressed to the fact that it is only possible to specify different steps in the weld plan, without the opportunity of specifying what happens when the clamps are released and the temperature is still pretty high. The results of the shrinkage methods for the six tests are shown in Figure 4.25, Figure 4.26 and Figure 4.27.

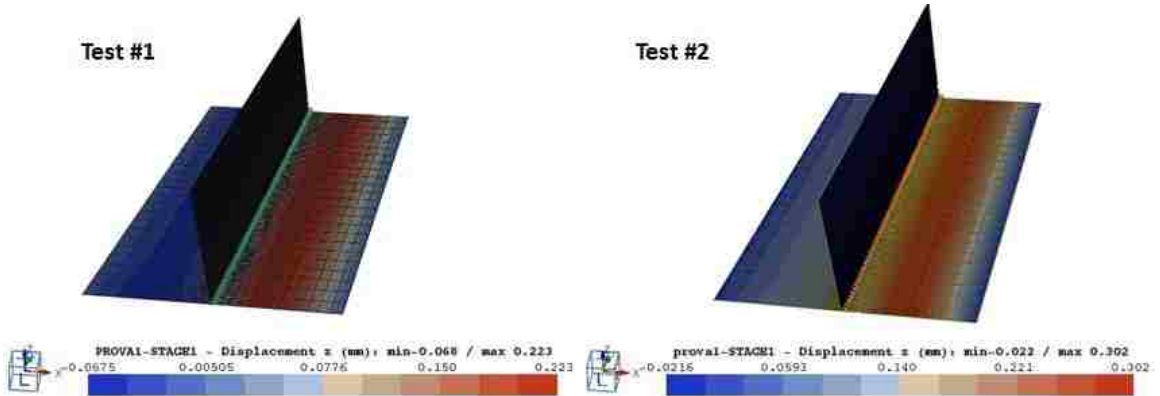


Figure 4.25- Distortion [mm] in z-direction [mm] for Test #1 and Test #2

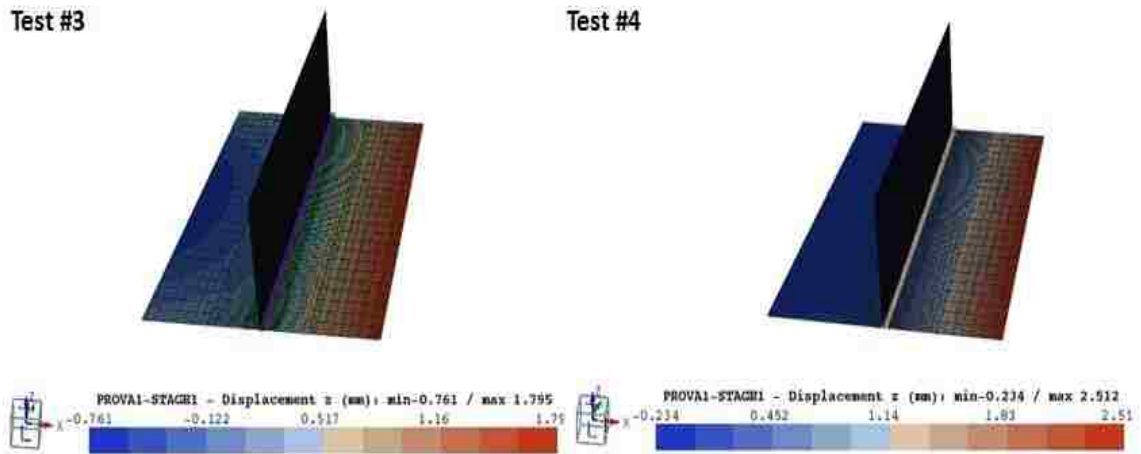


Figure 4.26- Distortion [mm] in z-direction [mm] for Test #3 and Test #4

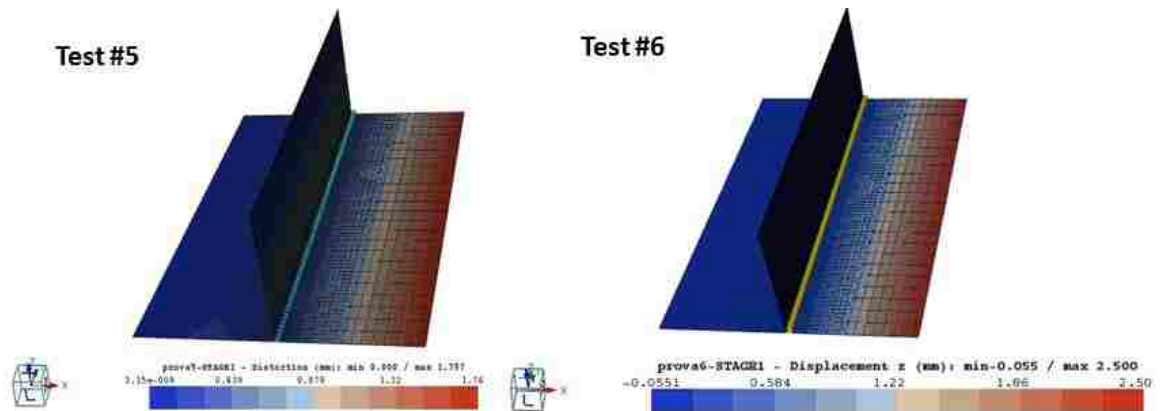


Figure 4.27- Distortion [mm] in z-direction [mm] for Test #5 and Test #6

From the above figures, it can be observed that in the positions where the clamps were held no distortion has been recorded. For example, in all six tests the left part of Coupon #3 has been always clamped and in fact no distortion can be observed.

This behavior is explained by the fact that it is not possible with WELD PLANNER to specify the time of clamping. Moreover, the software does not take into account any thermal behavior which has an important impact on the final distortion

#### 4.5 Validation of transient analysis and shrinkage method with data from the literature review

In order to validate the previous model, some simulations were carried both with the transient analysis and shrinkage method with data obtained by the paper “Simulation and experimental study on distortion of butt and T-joints using WELD PLANNER” [21]. In this research only the shrinkage method was used to simulate the experimental test, which consisted of a T-joint with a base plate of 100mm x 150 mm, and a stiffener of 50 mm x 150 mm. Both the base plates and the stiffener have a thickness of 4 mm. The welding parameters used in this research are listed in Table 4.13.

**Table 4.13-Welding parameters used in Sulamain et al. research**

Welding parameters	Tee-joint
Welding process	GMAW (Gas Metal Arc Welding)
Arc robot	ABB IRB 2400/16
Wire diameter (mm)	1.2
Filler wire	ER70S-6
Shielded gasses (Ar/CO2)	80%/20%
Current (A)	140-160
Voltage (V)	17-20
Travel speed (mm/s)	5
Wire feed speed (m/min)	3.4-4

The T-joint is clamped near the upper edges of the stiffener until the plates reach ambient temperature, Figure 4.28.





Figure 4.28- T-joint clamping condition [21]

The material used in their experimental test is a low carbon steel with material properties similar to S355J2G3. The previous material is the same one that has been used for the simulations in Section 4.1 and 4.2 and the related chemical composition and material properties have been already introduced in Section 4.1. The experiments showed the following angular distortions in Table 4.14.

Table 4.14-Experimental results of the validation test	
	Angular distortion (rad)
T-joint (1 <sup>st</sup> welded side)	0.028
T-joint (2 <sup>nd</sup> welded side)	0.013

#### 4.5.1 Model development and results for transient analysis-SYSWELD

For the transient analysis the same approach introduced in Section 4.1 has been used for the model development. For this reason, the deposition of the filler material was taken into consideration and the dimensions were reproduced using the data obtained from the test section (Figure 4.29). The geometry is composed by 16872 3D elements and is shown in Figure 4.29. The parameters for the heat source are listed in Table 4.15. The material used in this simulation the plate, the stiffener and the filler is S355J2G3.

**Table 4.15- Heat source parameters used in the simulation for validation**

<b>Parameter</b>	<b>Value</b>
Length	14.00 mm
Width	7.00 mm
Penetration	3.50 mm
Energy/length	555.00 J/mm

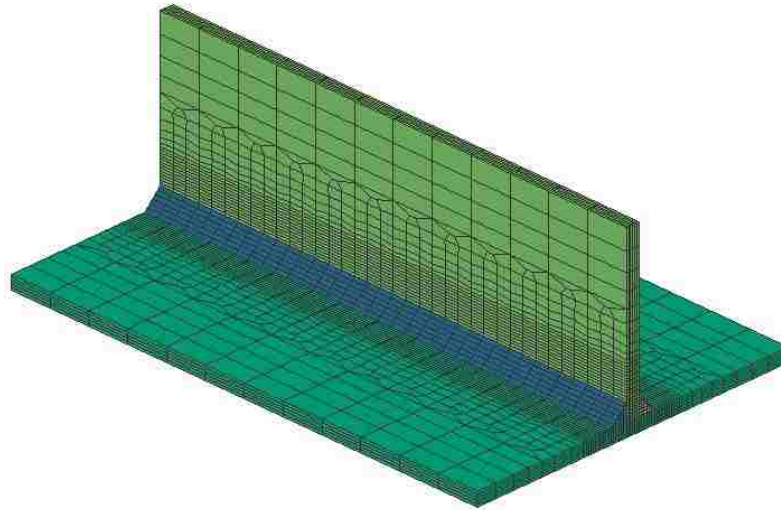


**Figure 4.29- T-joint mesh for the t-joint validation test**

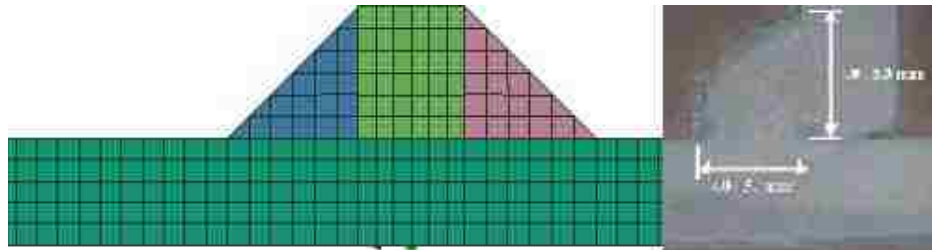


**Figure 4.30-Software section (left) and real section (right) of the T-joint validation test**

In the simulation, the clamps were held for 600 seconds and then the unclamped condition was set until for 3000 additional seconds. This large amount of time was needed for the plates to cool because the energy delivered by the welding process was very high. Figure 4.31 and Figure 4.32 display the distortion in z direction at 3600 seconds, after all the plates had reached ambient temperature. Higher displacements are observed in the first welded side compared to the second welded side. This can be

addressed to the fact the second side has been already influenced by the first weld, due to smaller variation of temperature.

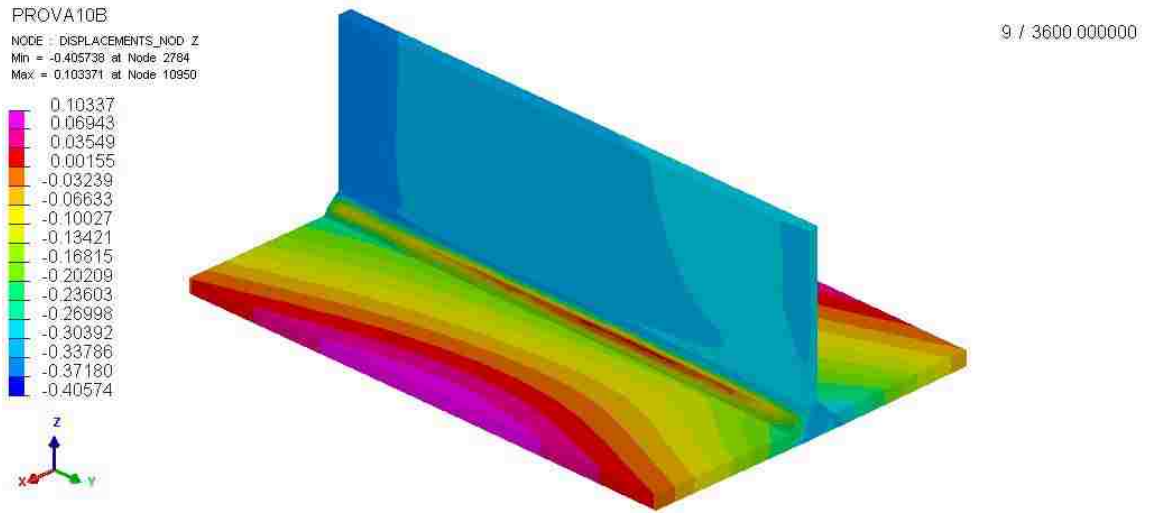


Figure 4.31- Displacement [mm] trend in z-direction for t-joint validation test at 3600s (view of the 1<sup>st</sup> welded side)

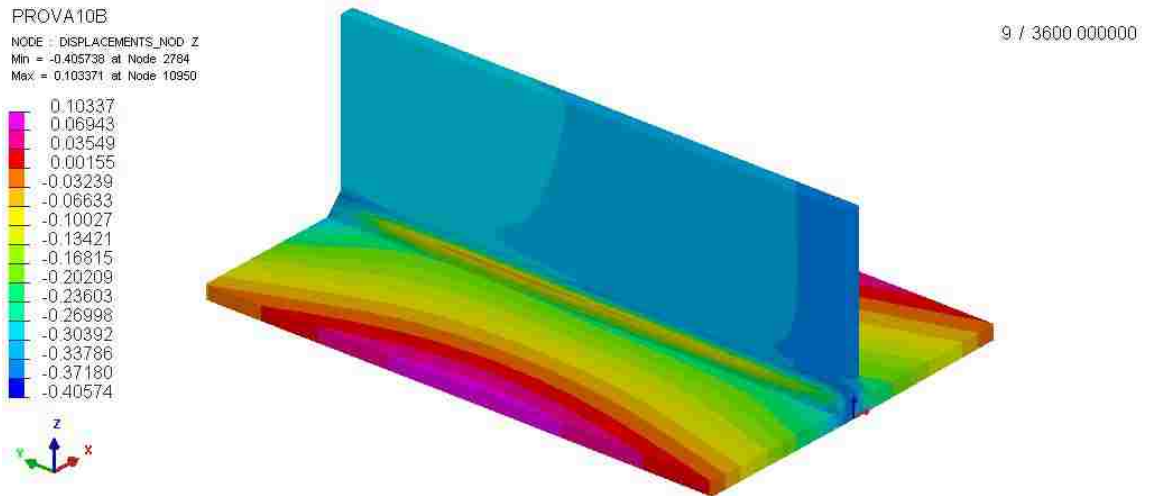
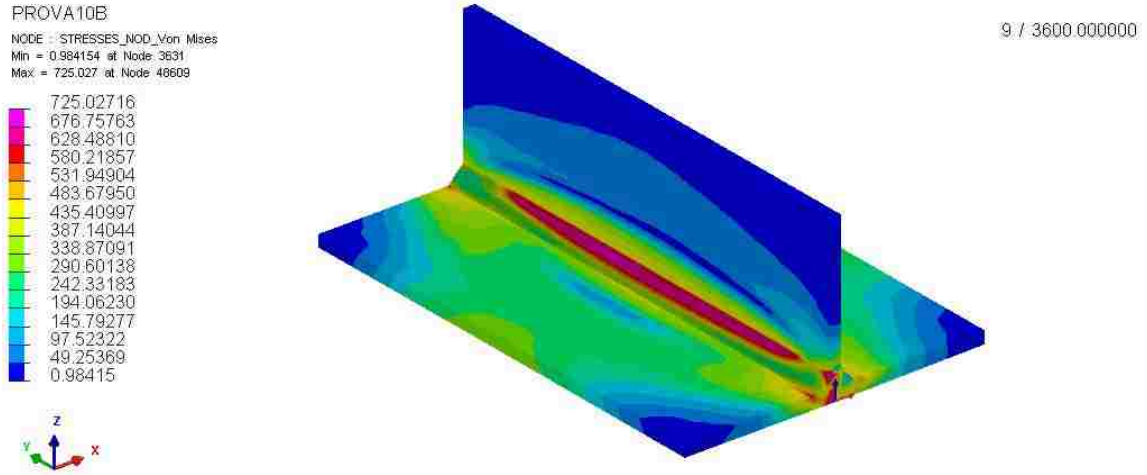


Figure 4.32- Displacement [mm] trend in z-direction for t-joint validation test at 3600s (view of the 2<sup>nd</sup> welded side)

The maximum value of Von Mises stress is 725 MPa as displayed in Figure 4.33



**Figure 4.33- Von Mises stress [MPa] for T-joint validation test at 3600s**

The results obtained from the transient analysis were compared to the experimental results, showing an error of 50 % in the first welded side and 43.1 % in the second welded side as reported in Table 4.16.

**Table 4.16-Comparison of Angular distortion results between simulation and experiment for t-joint validation test**

	Simulation [rad]	Experiment [rad]	Error
<b>T-Joint (1<sup>st</sup> welded side)</b>	0.014	0.028	50.0%
<b>T-Joint (2<sup>nd</sup> welded side)</b>	0.0074	0.013	43.1%

#### **4.5.2 Model development and results for shrinkage method-WELD PLANNER**

For the shrinkage method, the same approach introduced in Section 4.2 has been used for the model development. The T-joint geometry was modeled with 980 total shell elements (Figure 4.34). The material used in this simulation for the plate, the stiffener and the filler is S355J2G3.

A 4-mm thickness was assigned to all components, except for the second filler. This choice is addressed to the fact that the first welding pass influences the second one. For the previous reason, the thickness of the second filler pass was set to be 25% larger than the first filler pass. Moreover, the dimensions of the weld pool were modelled according to the cross section of a real weld pool as shown in Figure 4.35.

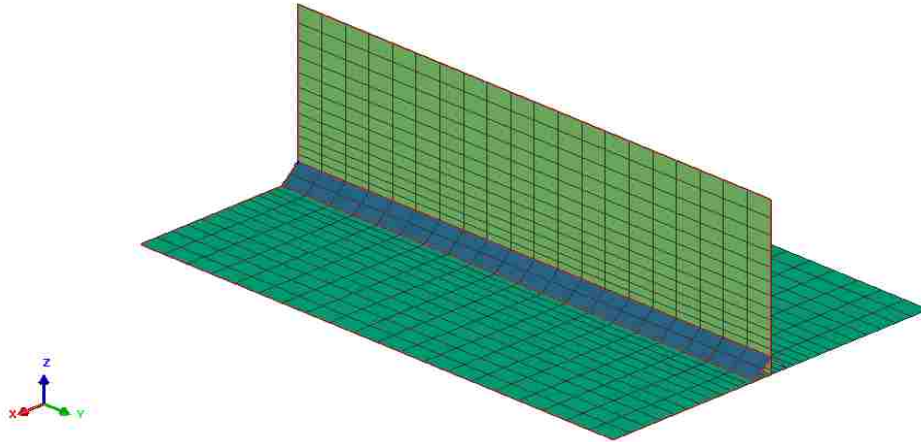


Figure 4.34-T-joint mesh validation test

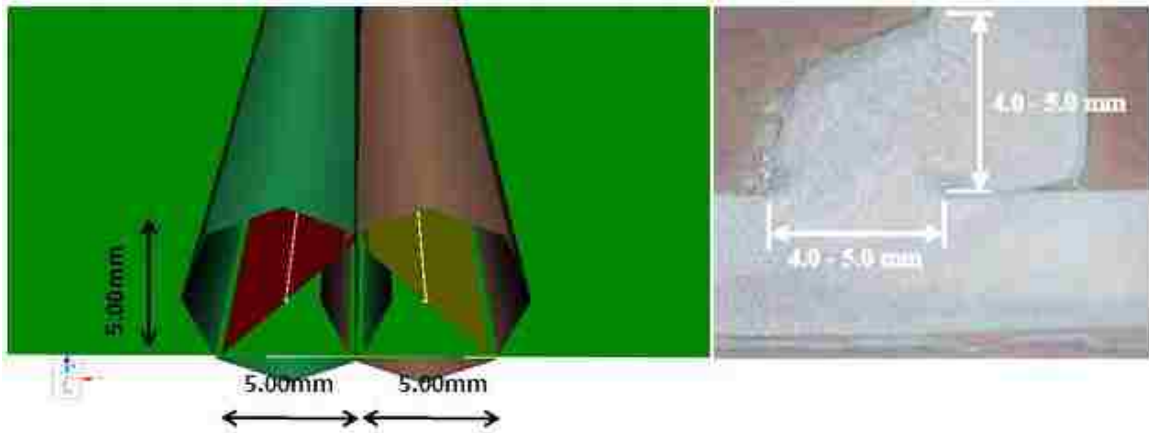


Figure 4.35-T-joint filler geometry-validation test

The clamping conditions are defined as in Figure 4.28. The collectors CLAMP\_01 and CLAMP\_02 represent the clamp that fixed the stiffener during the welding process until the plates are cooled.

The weld plan is divided into three steps. The first one is where the first weld takes place; and the second one is where the second weld takes place. The clamps are held for three consecutive steps. The weld plan for this condition is shown in the Figure 4.37.

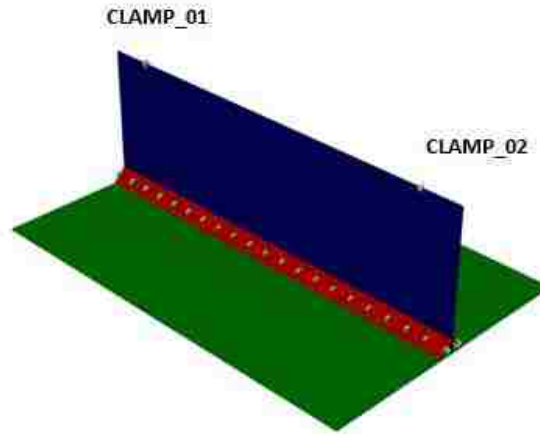


Figure 4.36-CLAMP\_01 and CLAMP\_02 position

		Steps					
		c	#	1	2	3	4
Objects				1	1	0	0
	JOINT_01		1				
	JOINT_02		1				
	CLAMP_01		3				
	CLAMP_02		3				

Figure 4.37-Weld Plan t-joint validation test

The displacement trend obtained with WELD PLANNER for this validation test is shown in Figure 4.38

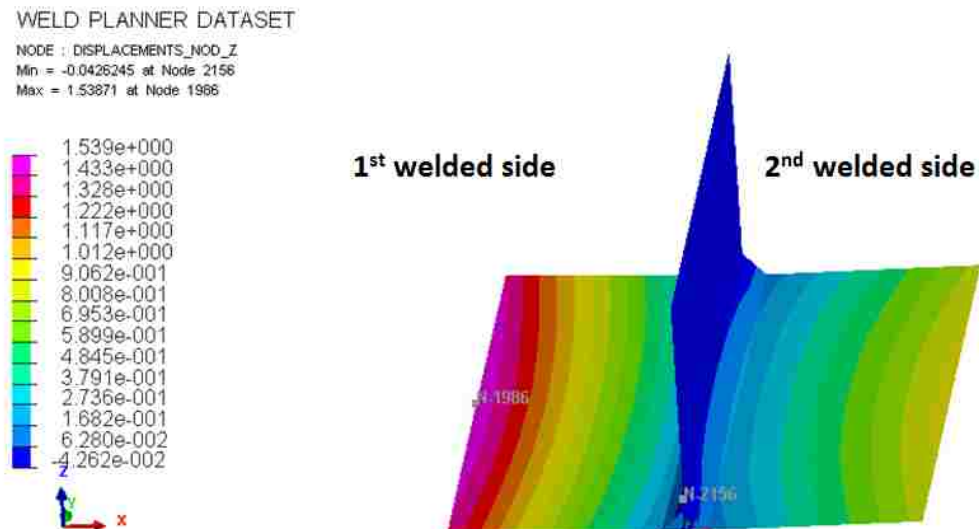


Figure 4.38-Displacement [mm] in z-direction t-joint validation test(WELD PLANNER)

Also in this case, the distortion was calculated taking into consideration the angular distortion. In the first welded side the angular distortion is 0.027 rad; whereas in the experimental test is 0.028 rad. For the second welded side, the angular distortion is 0.011 rad; whereas in the experimental test it is 0.013 rad. The comparison between the results from the simulation and the experimental test is shown in the Table 4.17.

**Table 4.17- Comparison of Angular distortion results [mm] between simulation and experiment for t-joint validation case (WELD PLANNER)**

	Simulation [mm]	Simulation [rad]	Experiment [mm]	Experiment [rad]	Error
<b>T-Joint (1<sup>st</sup> welded side)</b>	1.37	0.027	1.38	0.028	0.7%
<b>T-Joint (2<sup>nd</sup> welded side)</b>	0.79	0.011	0.67	0.013	15.1%

The results obtained from the simulation were slightly different compared to the simulation performed in the reference paper. This difference is due to the variation and lack of full information. For example, the exact location of the clamps has not been specified by the authors; for this reason an approximation of the clamp location was made. Moreover, as introduced before, the second filler pass of the T-joint was modeled with 25 % larger thickness as suggested from WELD PLANNER tutorial. If a different thickness was modeled, different results would have been found. The deformation of the T-joint for the validation can be visualized with a 10 x magnification in Figure 4.39.

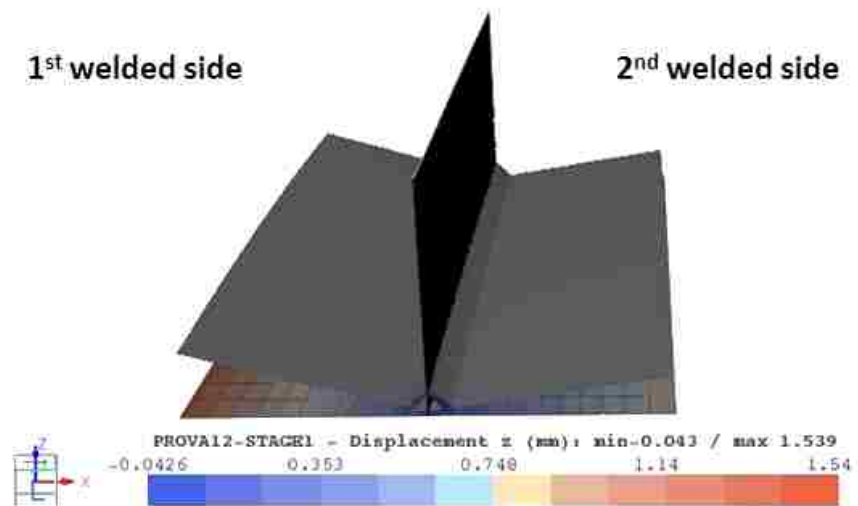


**Figure 4.39- Magnification 10x of the deformed T-joint validation case (WELD PLANNER)**

### 4.5.3 Comparison between transient and shrinkage analysis approach for the validation test

Table 4.18 shows the comparison between the results obtained in the transient analysis and in the shrinkage analysis. It can be observed that the shrinkage method better predicts the weld distortion compared to the transient analysis. This behavior can be addressed to the fact that less information are required in order to run the simulation in WELD PLANNER; and most of this information was provided by the authors of the paper taken into consideration. As for the transient analysis, more details are needed, such as the time between the first weld and the second weld, which in this case was assumed to be 15 seconds. Of course, the time between the two welds plays an important role in terms of final distortion, and it should be carefully recorded.

**Table 4.18- Comparison between transient analysis results and shrinkage analysis results for t-joint for the validation test**

T-joint	Angular distortion [rad]			Error %	
	Experiment	Sysweld	Weld Planner	Sysweld	Weld Planner
1 <sup>st</sup> welded side	0.028	0.014	0.027	50.0 %	0.7%
2 <sup>nd</sup> welded side	0.013	0.0074	0.011	43.1 %	15.1%

The transient analysis performed with Sysweld significantly underestimates the distortion, and it does not predict a remarkable difference in displacement between the first welded side and the second welded side. The shrinkage analysis is able to predict the different displacements between the two T-joint sides.

A qualitative comparison of the distortion trend between transient analysis and shrinkage method is shown in Figure 4.40 for the first welded side and Figure 4.41 for the second welded side.



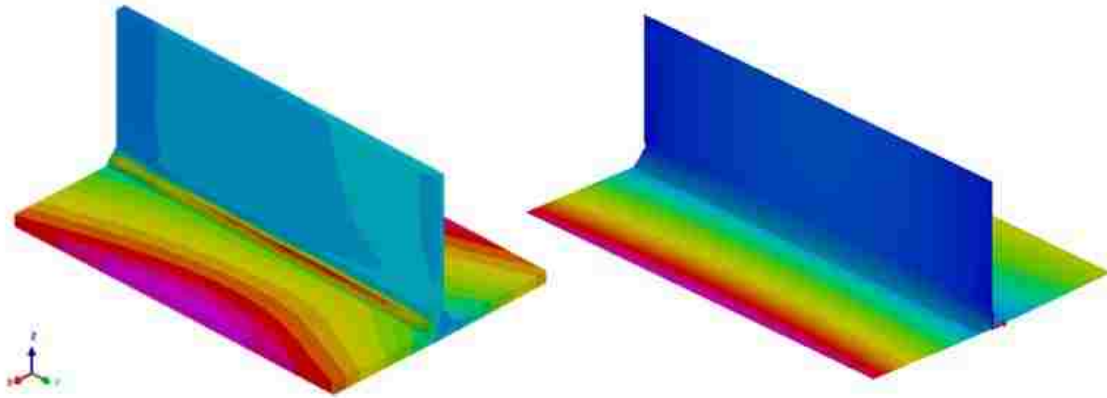


Figure 4.40- Qualitative distortion trend comparison between transient analysis (left) and shrinkage analysis (right) for the first welded side

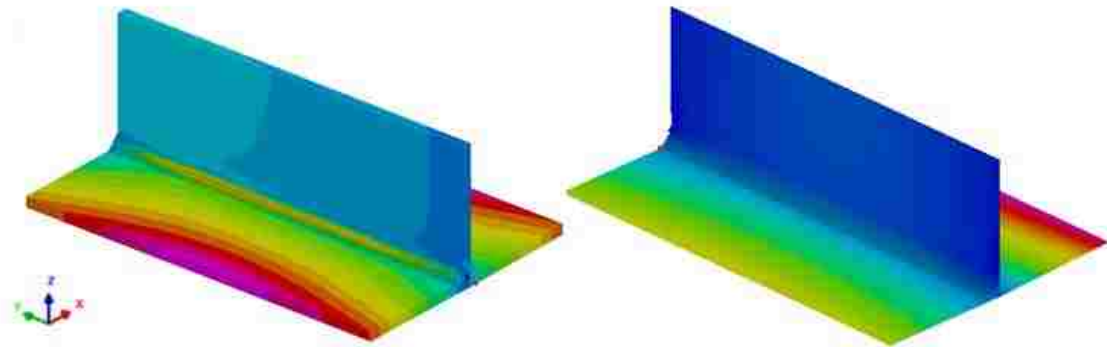


Figure 4.41- Qualitative distortion trend comparison between transient analysis (left) and shrinkage analysis (right) for the second welded side

## CHAPTER 5

### COMPARISON BETWEEN NUMERICAL RESULTS AND EXPERIMENTAL RESULTS

#### 5.1 Comparison between transient analysis results and experimental results

The comparison between the results of Test#1 obtained with SYSWELD and the experiment is shown in Table 5.1 Moreover, the average error along each Line is presented in Table 5.2.

**Table 5.1- Displacement results and error between simulation and experimental results for Test #1**

<b>Test 1</b>					
<b>Distance #</b>	<b>Experiment measurement [mm]</b>	<b>Simulation measurement [mm]</b>	<b>Experiment Displacement [mm]</b>	<b>Simulation Displacement [mm]</b>	<b>Error</b>
1	139.92	139.63	0.44	0.73	66%
2	139.88	139.70	0.48	0.66	38%
3	139.52	139.65	0.84	0.71	15%
4	108.96	108.80	0.49	0.65	33%
5	108.69	108.83	0.76	0.62	18%
6	108.83	108.82	0.62	0.63	2%
7	109.18	109.29	0.27	0.16	41%
8	109.36	109.32	0.09	0.13	44%
9	109.32	109.29	0.13	0.16	23%
10	140.65	140.49	-0.29	-0.13	55%
11	140.49	140.55	-0.13	-0.19	46%
12	140.52	140.50	-0.16	-0.14	13%

**Table 5.2- Average errors along the lines for Test #1**

<b>Line</b>	<b>Average error</b>
Line A	40%
Line B	18%
Line C	36%
Line D	38%

Test #1 shows an average value of 33 % calculated taking into consideration the error in each distance displacement. Line A presents an average error of 40 %. Moreover, the

simulated trend in this line appears to be different compared to the real one. As for Line B, the average error is 18 %, again the simulation is not able to predict the trend of the displacement. The trend for Line C has been reasonable predicted by the simulation, showing a 36 % of average error along the line. Line D presents an average error of 38 %, but this time the path of the distortion is not well predicted.

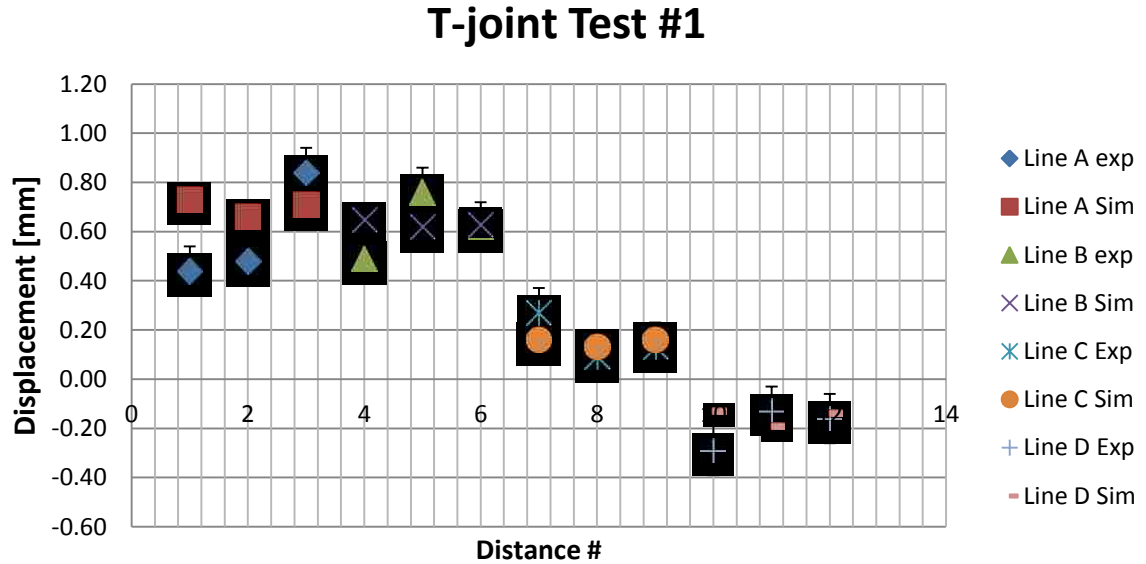


Figure 5.1- Displacements T-joint Test#1 for uncontrolled clamping condition

Comparison of the results for Test # 2 is shown in Table 5.3 and Table 5.4. From the following tables it can be calculated that in Test #2 the total average error of the simulation is 23 % compared to the experimental results.

The average errors for Line A, Line B and Line C are lower than for Test #1, with values included between 10 % and 24 %. Even though the average errors are reasonable for Line A and Line B, the results from the simulation exhibits a different trend in each of those lines compared with real values. On the other hand, Line C shows a good trend correlation. Line D presents an average error of 46 % even if the path has been successfully predicted by the software.

Table 5.3-- Displacement results and error between simulation and experimental results for Test #2- uncontrolled condition

Test 2					
Distance	Experiment measurement [mm]	Simulation measurement [mm]	Experiment Displacement [mm]	Simulation Displacement [mm]	Error
1	139.99	139.85	0.37	0.51	38%
2	139.73	139.88	0.63	0.48	24%
3	139.88	139.83	0.48	0.53	10%
4	108.97	108.94	0.48	0.51	6%
5	108.9	108.95	0.55	0.50	9%
6	108.76	108.93	0.69	0.52	25%
7	109.15	109.17	0.30	0.28	7%
8	109.19	109.22	0.26	0.23	12%
9	109.17	109.20	0.28	0.25	11%
10	140.33	140.31	0.03	0.05	67%
11	140.41	140.40	-0.05	-0.04	20%
12	140.34	140.35	0.02	0.01	50%

Table 5.4- Average errors along the lines for Test #2

Line	Average error
Line A	24%
Line B	13%
Line C	10%
Line D	46%

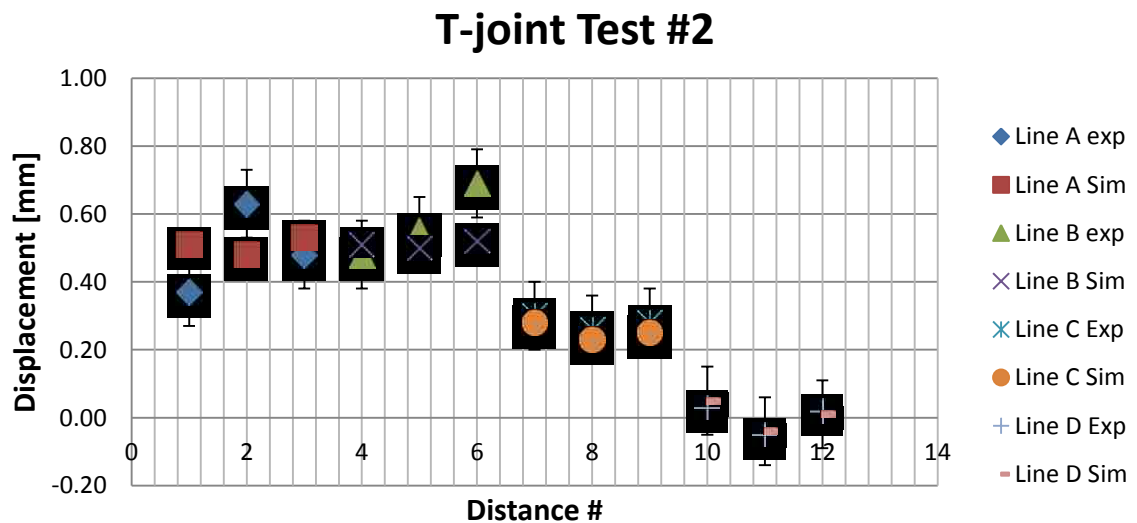


Figure 5.2- Displacements T-joint Test#2 for uncontrolled clamping condition

Simulation and experimental results for Test #3 are listed in Table 5.5.

**Table 5.5-- Displacement results and error between simulation and experimental results for Test #3- uncontrolled condition**

<b>Test 3</b>					
<b>Distance #</b>	<b>Experiment measurement [mm]</b>	<b>Simulation measurement [mm]</b>	<b>Experiment Displacement [mm]</b>	<b>Simulation Displacement [mm]</b>	<b>Error</b>
1	139.8	139.69	0.56	0.67	19%
2	139.84	139.72	0.52	0.64	23%
3	139.77	139.71	0.59	0.65	10%
4	108.96	108.83	0.49	0.62	26%
5	108.97	108.84	0.48	0.61	26%
6	108.98	109.15	0.47	0.30	36%
7	108.54	108.81	0.91	0.64	30%
8	108.7	108.92	0.75	0.53	30%
9	108.73	108.97	0.72	0.48	33%
10	139.33	139.66	1.03	0.70	32%
11	139.4	139.84	0.96	0.52	46%
12	139.81	139.91	0.55	0.45	18%

**Table 5.6- Average errors along the lines for Test #3**

<b>Line</b>	<b>Average error</b>
Line A	17%
Line B	29%
Line C	31%
Line D	32%

Simulation results for Test #3 exhibits a total average error of 27 %. Displacements along Line A have been simulated with a good correlation showing 17 % average error. In fact in this line, the lowest error can be found for Distance #3. The average errors in Line A, Line B and Line C found in the simulation results present values ranging from 29% to 32%. In Test #3 maximum displacements are observed in the lines which are on the same side where the weld took place. The displacement trend of each line has been successfully predicted (Figure 5.3), in a less precise way for Line B.

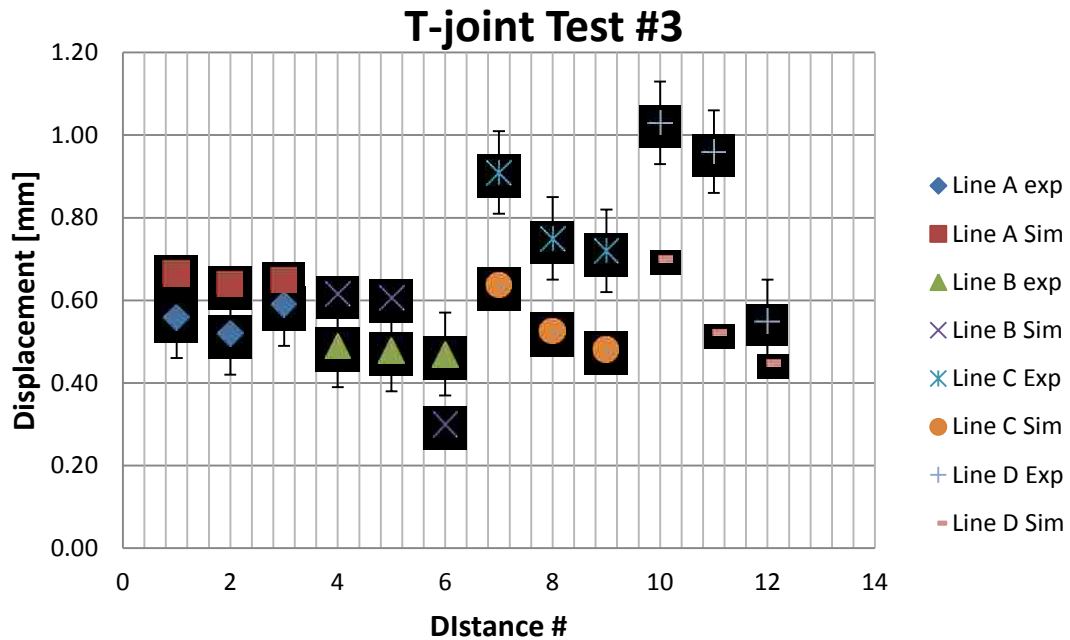


Figure 5.3- Displacements T-joint Test#3 for uncontrolled clamping condition

Displacement results from simulation and experimental data for Test #4 are reported in the following Table 5.7.

Table 5.7-- Displacement results and error between simulation and experimental results for Test #4- uncontrolled condition

Test 4					
Distance #	Experiment measurement [mm]	Simulation measurement [mm]	Experiment Displacement [mm]	Simulation Displacement [mm]	Error
1	140.13	140.02	0.23	0.34	48%
2	140.11	140.02	0.25	0.34	38%
3	140.52	140.47	-0.16	-0.11	31%
4	109.09	109.04	0.36	0.41	15%
5	109.06	109.03	0.39	0.42	7%
6	109.02	109.00	0.43	0.45	4%
7	108.63	108.40	0.82	1.05	28%
8	108.72	108.63	0.73	0.82	12%
9	108.94	109.00	0.51	0.45	13%
10	139.11	138.95	1.25	1.41	13%
11	139.01	139.34	1.35	1.02	25%
12	139.07	139.52	1.29	0.84	35%

Table 5.8- Average errors along the lines for Test #4

Line	Average error
Line A	39%
Line B	8%
Line C	18%
Line D	24%

The simulation results displays a total average error of 22%, which is the lowest error found among six tests. Line A presents an average error of 39%, and in this case the simulation tends to overestimate the distortion. This previous behaviour can be found in Line B, even though in this case the simulation correctly represents the real displacement with an average error of 8 %. Line C and Line D exhibit the highest values of displacement; these lines are located on the same side of the weld line. It is reasonable to expect higher displacement on the side more influenced by the welding process; moreover, that side was always unclamped.

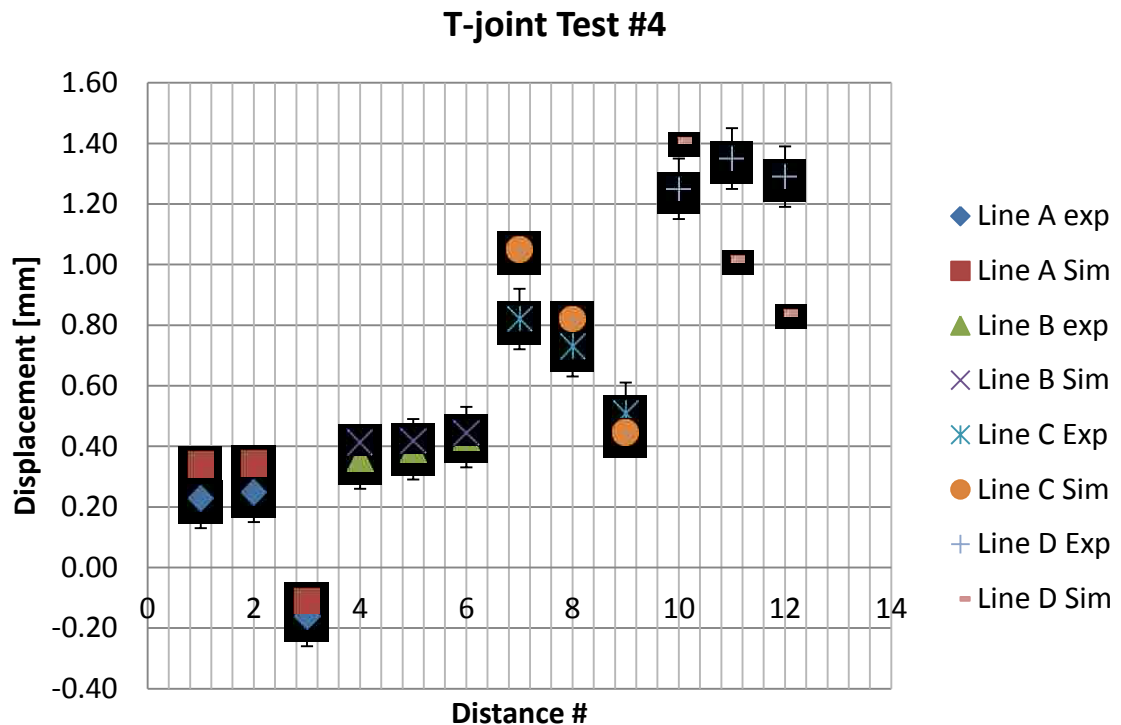


Figure 5.4- Displacements T-joint Test#4 for uncontrolled clamping condition

Test #5 for the uncontrolled clamping condition showed the following displacements in Table 5.9:

**Table 5.9-- Displacement results and error between simulation and experimental results for Test #5- uncontrolled condition**

<b>Test 5</b>					
<b>Distance #</b>	<b>Experiment measurement [mm]</b>	<b>Simulation measurement [mm]</b>	<b>Experiment Displacement [mm]</b>	<b>Simulation Displacement [mm]</b>	<b>Error</b>
1	139.85	139.72	0.51	0.64	25%
2	139.94	139.76	0.42	0.60	43%
3	139.87	139.72	0.49	0.64	31%
4	108.86	108.85	0.59	0.60	2%
5	108.99	108.87	0.46	0.58	27%
6	109.07	108.86	0.38	0.59	54%
7	108.67	108.76	0.78	0.69	12%
8	108.77	108.93	0.68	0.52	24%
9	109.11	108.96	0.34	0.49	44%
10	139.33	139.62	1.03	0.74	28%
11	139.78	139.86	0.58	0.50	14%
12	139.99	139.90	0.37	0.46	24%

**Table 5.10- Average errors along the lines for Test #5**

<b>Line</b>	<b>Average error</b>
Line A	33%
Line B	28%
Line C	26%
Line D	22%

Simulation for Test #5 showed a total average error of 27%. Line A presents an average error of 33%, which is the highest among all the lines taken into consideration in this test. However, the simulation is able to predict the trend along the line A. The experimental results differ in terms of trend compared to the simulation with an average error of 28%. Also in this case, high values of displacement are found in the side closest to the welded area and where no clamps were used. Line C and Line D presents average errors respectively of 26% and 22%. In both lines the software is reasonable able to predict the trend of the displacement.



## T-joint Test #5

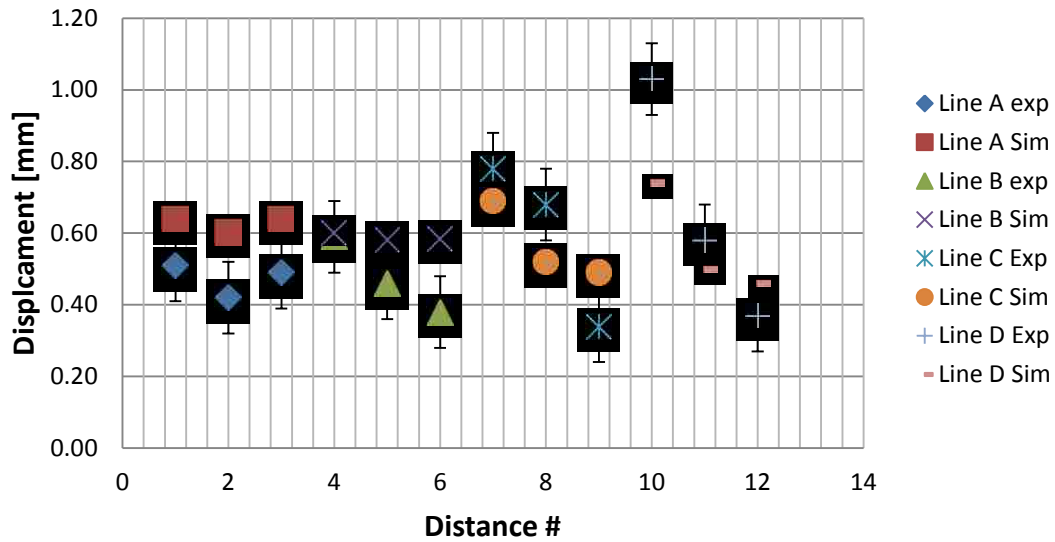


Figure 5.5 -Displacements T-joint Test#5 for uncontrolled clamping condition

Displacement results from simulation and experimental data for Test #6 are reported in the following Table 5.11.

Table 5.11-- Displacement results and error between simulation and experimental results for Test #6- uncontrolled condition

<b>Test 6</b>					
<b>Distance #</b>	<b>Experiment measurement [mm]</b>	<b>Simulation measurement [mm]</b>	<b>Experiment Displacement [mm]</b>	<b>Simulation Displacement [mm]</b>	<b>Error</b>
<b>1</b>	140.06	139.98	0.30	0.38	28%
<b>2</b>	140.03	139.96	0.33	0.40	21%
<b>3</b>	139.96	139.90	0.40	0.46	14%
<b>4</b>	109.12	109.01	0.33	0.44	33%
<b>5</b>	109.09	109.00	0.36	0.45	25%
<b>6</b>	109.08	108.98	0.37	0.47	26%
<b>7</b>	108.64	108.43	0.81	1.02	26%
<b>8</b>	108.73	108.68	0.72	0.77	7%
<b>9</b>	108.87	108.76	0.58	0.69	18%
<b>10</b>	139.16	139.01	1.20	1.35	12%
<b>11</b>	139.78	139.41	0.58	0.95	65%
<b>12</b>	139.94	139.56	0.42	0.80	90%

**Table 5.12- Average errors along the lines for Test #6**

Line	Average error
Line A	21%
Line B	28%
Line C	17%
Line D	56%

Simulation results for Test #6 shows a total average of 31%, calculated using the values in Table 5.11 and Table 5.12. The trend of Line A is well predicted by the simulation with an average error of 21 %. The same behavior can be observed for Line B and Line C with an average error along the line respectively of 28% and 17%. As for Line D, the highest value of average error (56%) has been found among all the lines,. It can be attributed to the fact the Distance #11 and Distance #12 significantly differ from the real values.

### T-joint Test #6

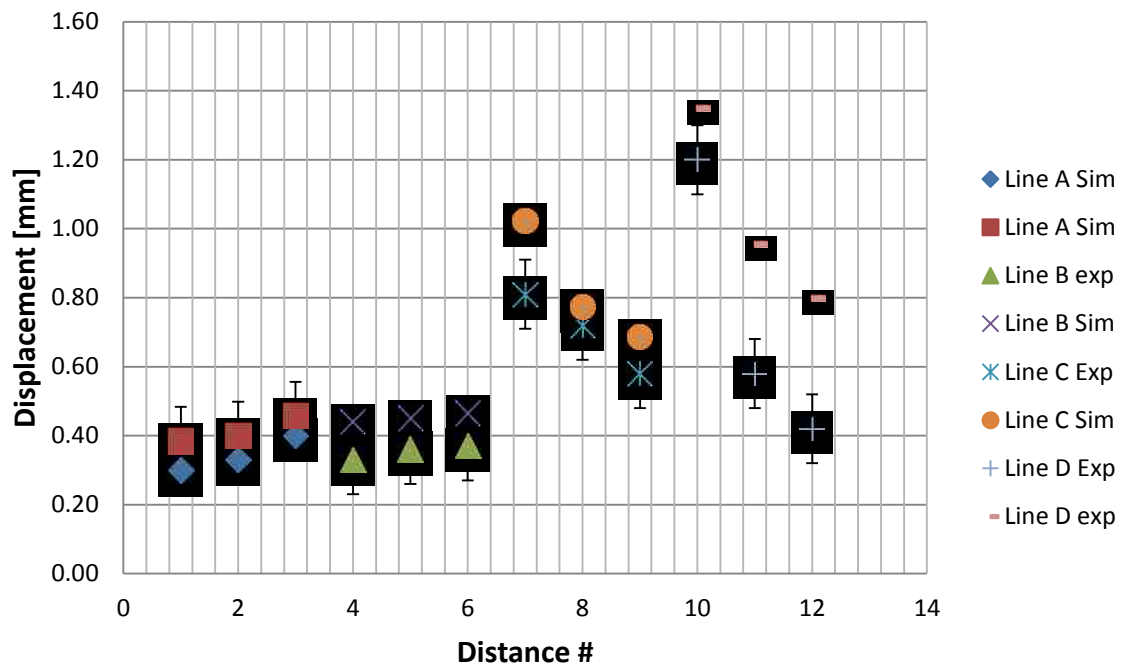


**Figure 5.6- Displacements T-joint Test#6 for uncontrolled clamping condition**

## 5.2 Comparison between shrinkage method and experimental results

A direct comparison between the shrinkage method and the experimental results cannot be performed. The main challenge arises from the lack of thickness, since just shell elements were modeled. Figure 5.7 shows different values of distance for T-joint models used in the transient analysis and in the shrinkage method. In WELD PLANNER the thickness of the material is not modelled but it is added as a parameter in the simulation. For this reason, it is pointless to calculate the twelve distances introduced in Section 3.2.

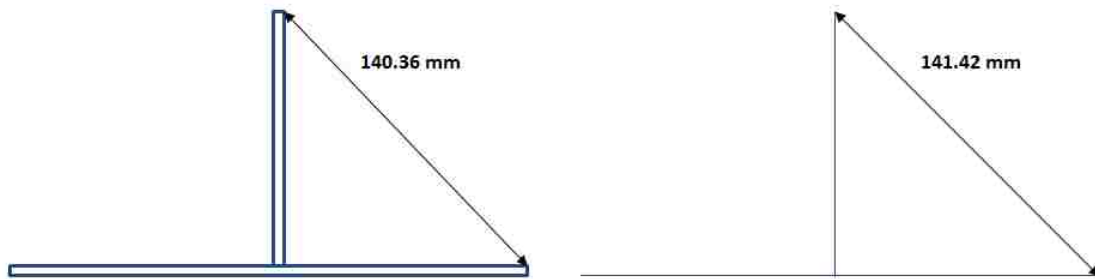


Figure 5.7-Example of distance for transient analysis model (left) and shrinkage analysis model (right)

Moreover, as introduced in section 4.4, the experimental clamping condition cannot be reproduced with WELD PLANNER. In fact the results obtained with the simulations presented no distortion were the clamps were positioned, whereas in the experimental tests distortion were recorded also in the position where the clamps were held. In conclusion, WELD PLANNER cannot model unclamped boundary condition.

## CHAPTER 6

### OPTIMIZATION WITH WELD PLANNER

The shrinkage method was not able to successfully predict the distortion for the experimental tests introduced in Chapter 3. This was due to the fact that the clamps were held for a very short time. Conversely, the shrinkage method was able to predict reasonably well the distortion in the case where the clamps were held until the plates reached ambient temperature (long clamping time), as discussed in Section 4.5.2. Thus, using the latter clamping conditions, additional simulations were performed using different welding parameters and material thicknesses.

The T-joint was modeled with the same dimensions used in the experimental tests and with only one weld pass on one side. The geometry and the dimensions of the T-joint are reported in the following Figure 6.1.

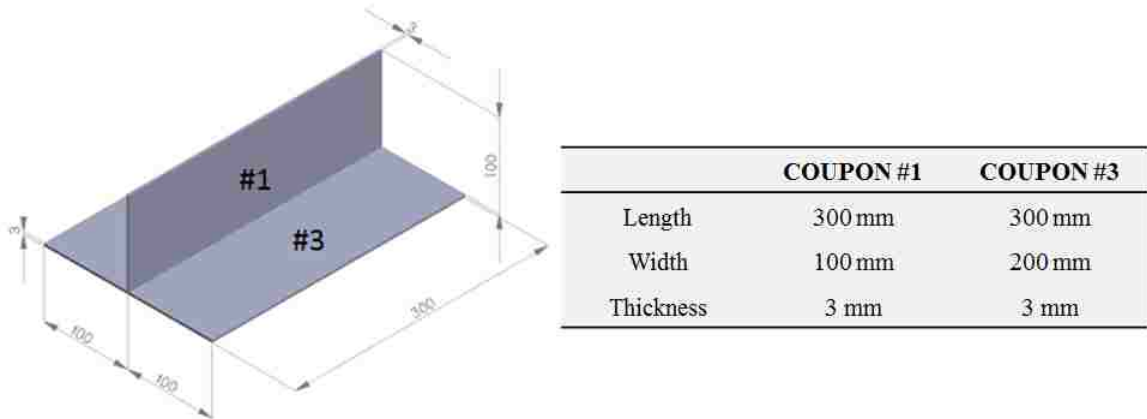


**Figure 6.1-Geometry and dimensions of the T-joint used for the optimization**

Two cases were exploited with the following material combinations (Table 6.1). Chemical composition and minimum mechanical properties of these materials have already been introduced in Section 4.1.

**Table 6.1-Material combination for Case #1 and Case #2**

	Case #1	Case #2
<b>Coupon #1</b>	DC_04	S355J2G3
<b>Coupon #2</b>	S355J2G3	S355J2G3

Moreover, the two cases had the same clamping condition (Base configuration) comprised of two clamps on one side of coupon #3 and two clamps near the edges of Coupon #1 constraining all directions, as shown in Figure 6.2.

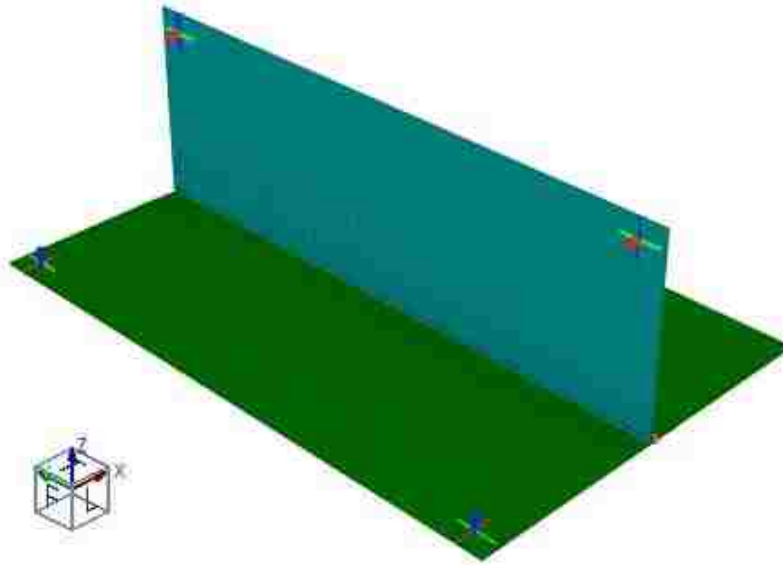


**Figure 6.2-Base Clamping configuration for both Case #1 and Case #2**

Different arc bead widths were simulated with value of 5mm, 6 mm and 6.8 mm. The relative geometries of the filler are shown in Figure 6.3. In arc welding, high values of arc bead width correspond to high values of energy input.

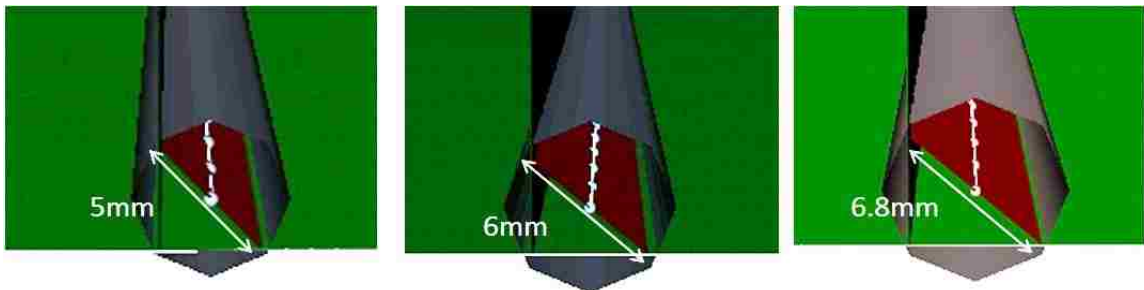


**Figure 6.3-Different arc bead widths used in the simulations**

Different material thicknesses were used in the simulations: 1mm, 2mm, 3 mm and 4 mm. Simulation results for Case #1 and Case #2 with different arc bead widths and different thicknesses are reported in Table 6.2, Table 6.3 and Table 6.4.

It can be observed that the maximum displacement in the z direction is obtained for T-joint Case #2 with 1 mm material thickness and a 6.8 mm width arc bead width. the

Lowest displacement is recorded for T-joint Case #2 with 1-mm material thickness and 5-mm arc bead width.

**Table 6.2-Influence of thickness on the maximum displacement in case of arc bead width of 5 mm**

<b>Arc bead 5 mm</b>		
<b>Material Thickness [mm]</b>	<b>Case #1 Max Displacement [mm]</b>	<b>Case #2 Max Displacement [mm]</b>
1	2.54	3.98
2	1.81	2.73
3	1.37	1.93
4	1.09	1.43

**Table 6.3- Influence of thickness on the maximum displacement in case of arc bead width of 6 mm**

<b>Arc bead 6 mm</b>		
<b>Material Thickness [mm]</b>	<b>Case #1 Max Displacement [mm]</b>	<b>Case #2 Max Displacement [mm]</b>
1	2.98	4.16
2	2.25	3.37
3	1.77	2.50
4	1.43	1.91

**Table 6.4- Influence of thickness on the maximum displacement in case of arc bead width of 6.8 mm**

<b>Arc bead 6.8 mm</b>		
<b>Material Thickness [mm]</b>	<b>Case #1 Max Displacement [mm]</b>	<b>Case #2 Max Displacement [mm]</b>
1	3.10	4.70
2	2.41	3.75
3	1.98	2.90
4	1.65	2.31

For all the three values of arc bead width, Case # 2 showed higher values of displacement. In particular, in the tests run with 5 mm and 6 mm arc bead width, Case #2 presented an average increase of maximum displacement among all the material thickness configuration of approximately 44 % compared with the results obtained in Case #1. Whereas, the simulation run with 6.8 arc bead width showed an increase among all the thickness configuration of about 48 % compared to simulations run for Case #1.

Figure 6.4 introduces the influence of different arc bead widths on the maximum displacement in z-direction found in the simulations. It can be noticed that an approximate linear relation exists between the maximum displacement and the arc bead width. Furthermore, 6.8 mm arc bead width led to higher displacement in each simulation with various thicknesses. This behaviour can be addressed to the fact that the arc bead width is a function of the heat input. Higher heat inputs equal more distortion.

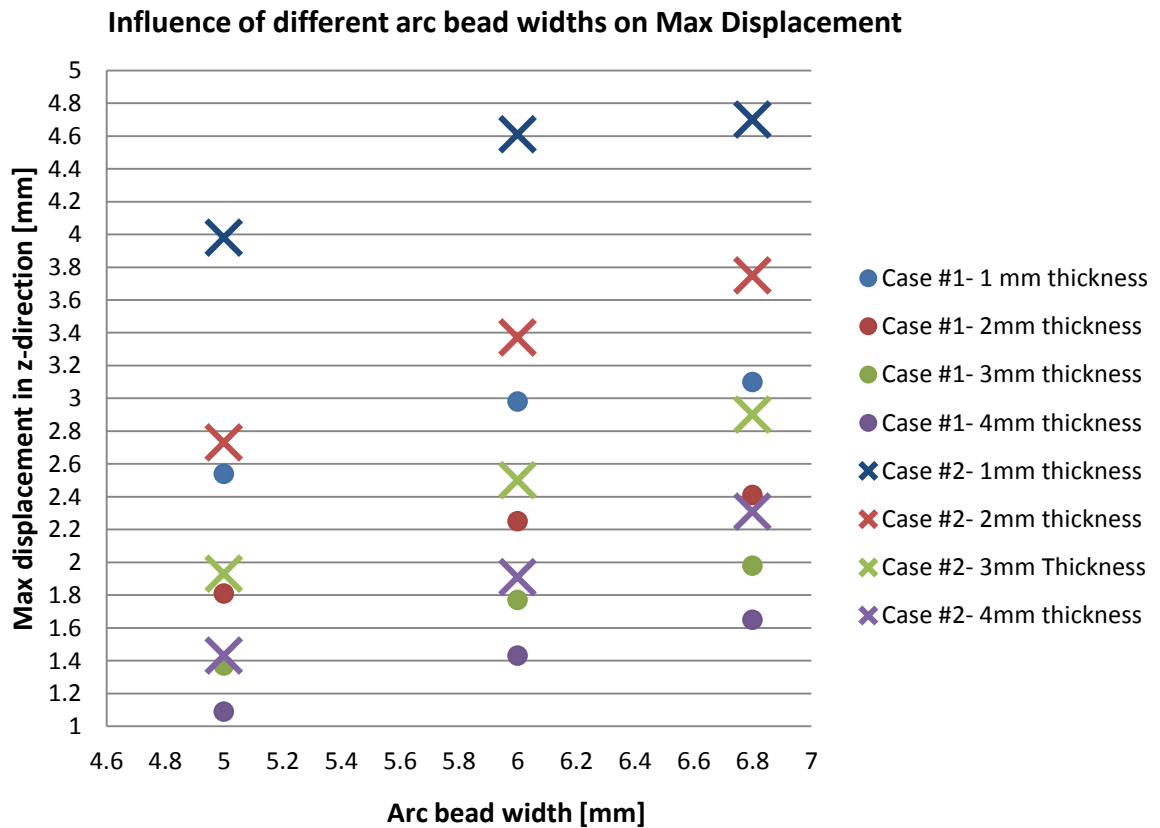


Figure 6.4-Influence of different arc bead width on Max Displacement

In Figure 6.5, the influence of different material thicknesses on the maximum displacement is presented. It can be observed that an increase in thickness lead to a decrease in the maximum displacement in z-direction obtained in the simulation.

The results for Case #1 with a 6.8 mm arc bead width and 1 mm thickness showed an increase in maximum displacement in the z direction approximately of 22 % compared to

Case #1 with 5 mm arc bead width and 1 mm thickness. For the same conditions Case #2 showed an increase in displacement of 18 %.

Considering simulations with a 4 mm thickness, Case #1 with a 6.8 mm arc bead presented an increase of displacement of 51% compared to Case #1 with 5 mm thickness. Given the same combination of parameters, Case #2 showed a displacement increase of 61%. Thus, high values of thickness lead to a higher displacement increase in percentage when the arc bead width changes from 5 mm to 6.8 mm; yet overall the effect of increasing plate thickness was to lower the maximum displacement. It is attributed to increasing the structural constraint.

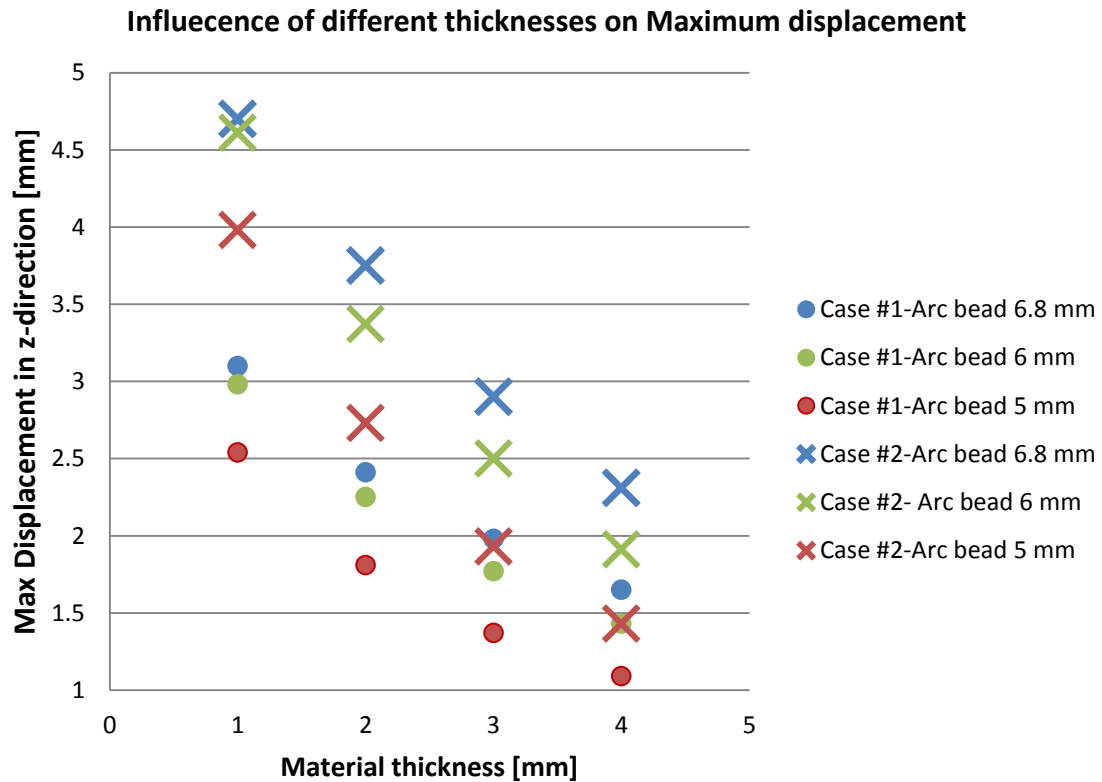


Figure 6.5-Influence of different material thicknesses on maximum displacement

As noticed before, Case #2 exhibits higher displacement compared to Case #1 in all the simulations. This behavior can be explained taking into consideration Equation 2.19 and 2.20 introduced in Section 2.2. The shrinkage value is proportional to the shrinkage force. The shrinkage force is proportional to the elastic modulus, heat input and the thermal



expansion, whereas it is inversely proportional to the heat capacity and the material density. Among all the above parameters, the only one that changes between DC\_04 and S355J2G3 is the thermal expansion (from WELD PLANNER database). This could be the reason of the different final displacement between the two steels.

Further simulations were run in order to understand the influence of the clamping positions on the maximum displacement. For those simulations a 6 mm arc bead width has been simulated. The first clamping condition exploited is Configuration A. This configuration differs from the base configuration because the clamps were moved in y-direction as shown in Figure 6.6.

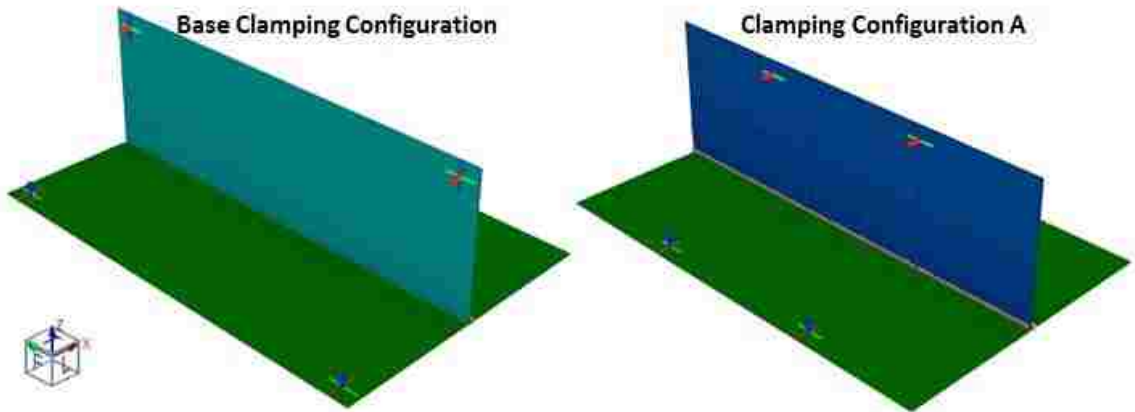


Figure 6.6- Difference between base clamping configuration and clamping configuration A

The maximum displacements in z-direction obtained by the simulations were compared to the results found with the Base clamping configuration as shown in the following Table 6.5.

Table 6.5-Maximum displacement results for base clamping configuration and configuration A

	Arc bead width 6 mm			
	Base Clamping Configuration		Clamping configuration A	
	Max displacement [mm]		Max displacement [mm]	
Thickness	Case#1	Case #2	Case#1	Case #2
1 mm	2.98	4.61	2.97	4.66
2 mm	2.25	3.37	2.24	3.40
3 mm	1.77	2.50	1.76	2.50
4 mm	1.43	1.91	1.43	1.92

The second clamping condition exploited is Configuration B. In this configuration the clamps are moved in x-direction from the position in the base configuration as shown in Figure 6.7.

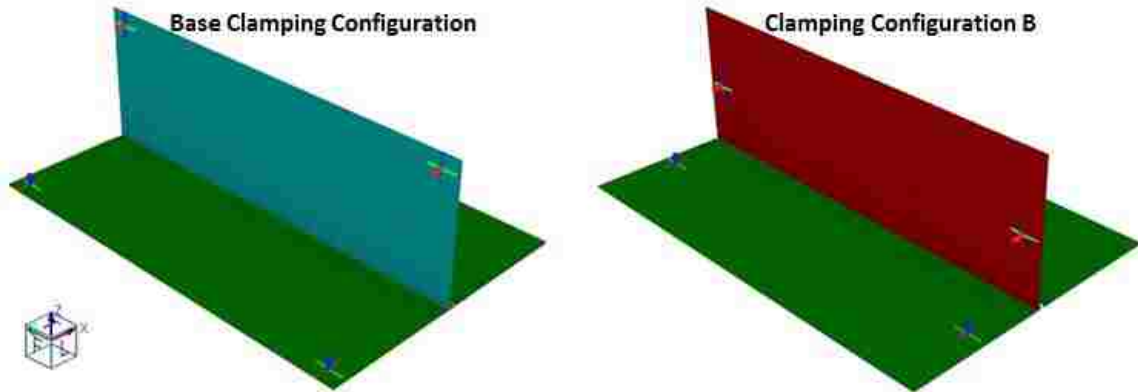


Figure 6.7- Difference between base clamping configuration and clamping configuration B

Table 6.6 shows the maximum displacement results for the base clamping configuration and the results for the clamping configuration B.

Table 6.6-Maximum displacement results for base clamping configuration and configuration A

	Arc bead width 6 mm			
	Base Clamping Configuration		Clamping configuration B	
	Max displacement [mm]		Max displacement [mm]	
Thickness	Case#1	Case #2	Case#1	Case #2
1 mm	2.98	4.61	2.98	4.61
2 mm	2.25	3.37	2.27	3.38
3 mm	1.77	2.50	1.80	2.51
4 mm	1.43	1.91	1.46	1.93

The above Table 6.5 and Table 6.6 show that the different position of the clamps had a negligible influence on the maximum displacement.

After analyzing the results of the simulations, it has been observed that large dimensions of the arc bead and low material thickness value lead to an increase of the maximum displacement in the T-joint in one pass on one side. Again, this is due to the effect of high heat input and low material constraint.

## CHAPTER 7

### CONCLUSIONS AND RECOMMENDATIONS

#### 7.1 Conclusions

According to the data and results provided in the previous chapters, the following conclusions can be drawn:

1. Arc welding modeling consists in a complex coupling between the mechanical, thermal and materials analysis. The mechanical behaviour of the weld is strictly correlated to the heat transfer. Thus, thermal history plays an important role and the welding process and the heat source should be carefully studied.
2. Different methods are available to predict weld distortion. Three main categories have been found: numerical approach, statistical approach and empirical approach. Numerical approach has been widely used in the past decades in order to predict the weld distortion and three main categories are found, including transient analysis, shrinkage approach and local global analysis. Transient analysis uses phase transformation and thermal material properties in order to better simulate the welding thermal history. The shrinkage method is based on linear elastic analysis and no metallurgical analysis is performed. Local global analysis predicts distortion with the use of transient analysis for large parts.
3. After analyzing all the available methods used for the distortion prediction, transient analysis and shrinkage method were found to be the most reliable and easy to use. The research focuses on the arc welding model of a T-joint. The shrinkage simulations were built and solved using the WELD PLANNER, whereas the transient simulations were solved with Sysweld.
4. The displacement results from the simulations obtained with Sysweld were compared with the results obtained with experimental test. Higher displacement values were observed in the tests that had the same material for each coupon compared to the tests that had different coupon materials. In particular high strength steels show higher displacement compared to mild steel. This behaviour can be attributed to the fact the microstructure and composition of the weld pool change with the use of different

- materials. The microstructure of the weld pool plays an important role in the weld distortion and it represents one of the main problems. Transient analysis was able to predict the distortion with an average error of 27 %. Transient analysis allowed the Von Mises stress computation. High stress values were found in proximity of the arc.
5. WELD PLANNER was not able to predict the distortion obtained with the experimental tests. The welding process can be divided into steps but clamping time cannot be specified. For this reason, WELD PLANNER is not able to predict weld distortion in case of an unclamped condition.
  6. Validation of the transient analysis and the shrinkage method was also performed using data obtained from the literature. Transient analysis performed with Sysweld showed an error of 50% in the first welded side and 43.1% in the second welded side. In comparison, the shrinkage method performed with WELD PLANNER presented an error of 0.7% in the first welded side and 15.1% in the second welded side. In this case it is observed that WELD PLANNER better predicts the weld distortion compared to Sysweld.
  7. The computational time for each T-joint simulation was approximately 8-9 hours for the transient analysis and 2-3 minutes for the shrinkage methods. Thus, shrinkage method presented significantly shorter computational time compared to the transient analysis.
  8. In Chapter 6 it is possible to observe that high value of arc bead width and low thickness value lead to high displacement. Arc bead width is strictly correlated to the amount of energy delivered during the welding process. Wide arc bead equals high energy input. Simultaneously, the temperature reached in the process depends on the energy input. Furthermore, in case of thin plates, the stiffness of the structure decreases and the gradient temperature increases during the welding process. For these reasons high displacements are found in thin plates.

## **7.2 Future work and recommendations**

One of the main challenges in this research was to find an appropriate way to bring into comparison the experimental and the simulated distortions. In order to overcome this problem and obtain adequate results, more precise measuring tools should be used, such as white light scanner and CMM. Further experimental tests should be performed with a

wider material selection in order to match the automotive interest toward the joining of lightweight materials. In general, shrinkage method should be applied just during the design stage and in case of long clamping conditions, for this reasons application in automotive field results to be difficult. In general, transient analysis is recommended for weld distortion prediction in automotive application. Additionally, because of the complexity of use of Sysweld, other transient analysis software should be considered. In automotive companies, employers are already specialized in using transient analysis software, so it would be easier for them to implement a way of simulating welding instead of learning new software.

Future work should focus on the simulation of different geometries that better reflect actual automotive components. Additional efforts should be put forward to evaluate the software for resistance welding process. Measurement of the actual residual stresses in welded parts could be compared to the simulated values.

## 8. APPENDICES

### Appendix A - A guide to welding process in Sysweld Environment

The SYSWELD simulation includes three main stages:

1. Modeling with Visual-Mesh,
2. Analyzing welding process with the use of Visual-WELD
3. Post-processing with Visual Viewer.

The main stages are showed in the Figure 8.1.

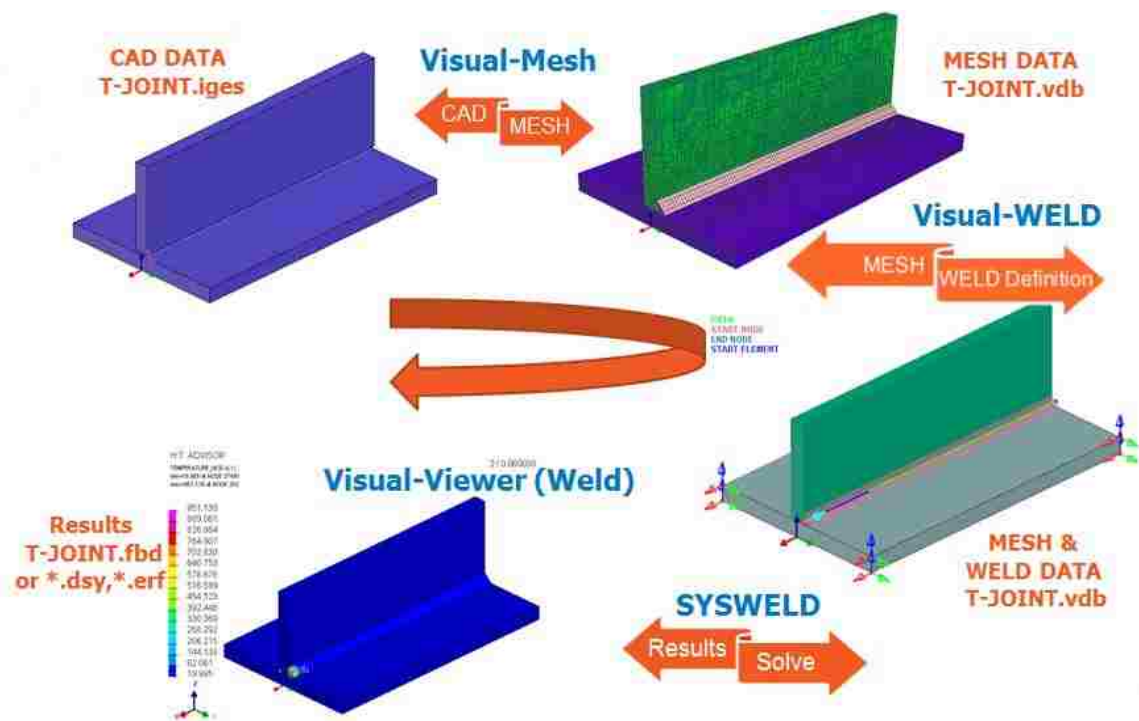


Figure 8.1-Example of Sysweld Workflow [59]

### Modeling with Visual Mesh 9.5

The first step includes the development of the model geometry. This step can be accomplished with the use of the Visual Mesh 9.5 included in the SYSWELD package. This tool allows building the geometry with different types of meshes. In addition collectors can be created such as the load of the heat input and the position of the clamps. Once the geometry has been created, a file (filename\_DATA1000.ASC) is generated.

## **Analyzing and simulation of welding process with Visual-WELD 9.5**

The file (filename\_DATA\*.ASC) generated in the previous stage can be imported in Visual-Mesh 9.5. Stage 2 can be accomplished with the dedicated tool "Welding Advisor" included in Visual-WELD 9.5. Different steps need to be accomplished in order to insert the minimum amount of parameters:

1. Project description
2. Global parameter
3. Component properties
4. Welding process
5. Cooling condition
6. Clamping condition
7. Loads and deformations
8. Contact definition
9. Solution parameter

In Step 1 it is possible to specify the project name and the directory; moreover the entire results file will be stored in that directory as shown in Figure 8.2.

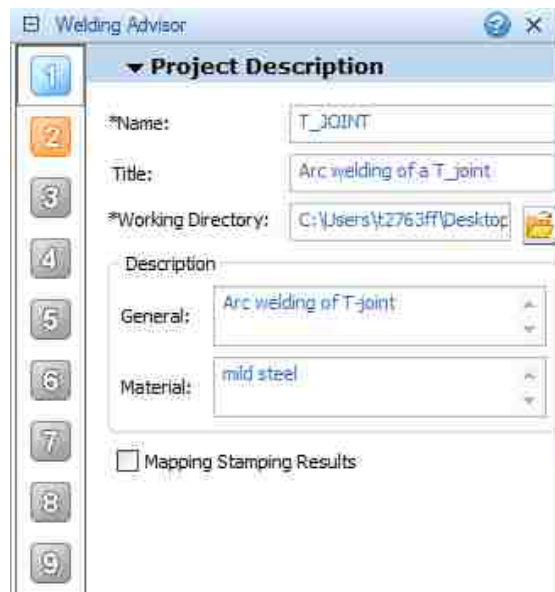


**Figure 8.2-Example of Step1-Project description**

In the global parameter step (Step 2) the computational alternative for the project can be chosen such as solid, shell-solid, shell, 2D Cross Section, 2D In-Plane and 2D Rotational. In most of the cases the alternative is automatically recognized.

In Step 3 (Component properties), material definition can be applied to every single component present in the model. Materials are assigned using a designated database provided by the solver. Moreover, different materials can be assigned for the component and the filler.

In Step 4 , the welding process type can be chosen among different welding process as shown in Figure 8.3. For all the simulations taken into consideration General arc has been used.



Figure 8.3-Different types of welding processes included in Welding Advisor

In addition the trajectory of the weld line need to be specified and a dedicated tool Called WELD LINE is available in Visual-Weld 9.5. In order to compute the path of the moving heat source, two curves showed in Figure 8.4 need to be defined:

- **Trajectory curve** : group of 1D elements, linked to the mesh, along the welding path [28]



- **Reference curve** : provides information to compute the local frame at the centre of the heat source [28]

The welding start node has to be chosen as first and it has to be coincident with the start of the welding process.

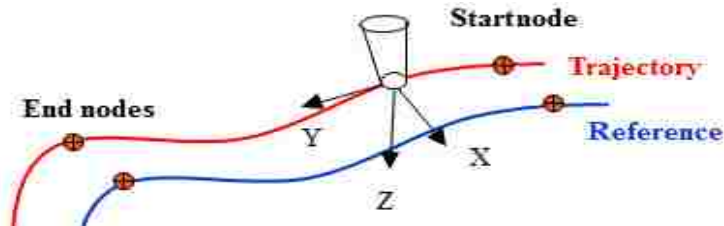


Figure 8.4- Trajectory and reference path using for the moving heat source

In Step 4 of the Welding Advisor it is necessary to define the parameters of the mathematical description of heat source, time and velocity of the welding process.



Figure 8.5-Parameters require for the welding process (Step 4)

The estimated length, width and penetration of the heat source can be deduced from weld pool study of a section of the welded part. The heat energy per unit length delivered by the welding process can be calculated using the following equation:

$$E = \frac{I * V}{v}$$

Where I is the current, V is the voltage,  $v$  is the welding speed and E is the energy per unit length. The efficiency of the welding process can be added as well.

The length, width and penetration of the heat sources are compliant with the Goldak double ellipsoid introduced in Section 2.1.2.1, the software provides also a short description of those parameters showed in Figure 8.6.

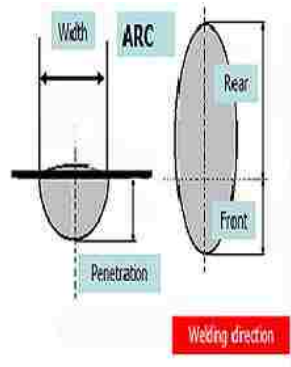


Figure 8.6- Penetration, width and length of the heat source

Step 5 focuses on cooling condition. Welding advisor allows creating cooling condition creating a 3D skin on the geometry that can be cooled down by forced cooling or free cooling. It is possible to specify the initial ambient temperature as shown in Figure 8.7.

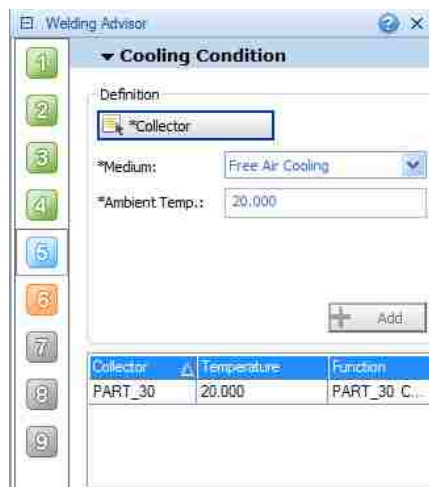


Figure 8.7-Example of cooling condition (Step 5)

In Step 6, Clamping conditions need to be specified choosing the clamping collectors, previously created in Visual-Weld, and choosing for how long the clamps are held. Different types of Clamp definition can be defined such as Elastic, Rigid, Symmetric, Stops and unclamped.

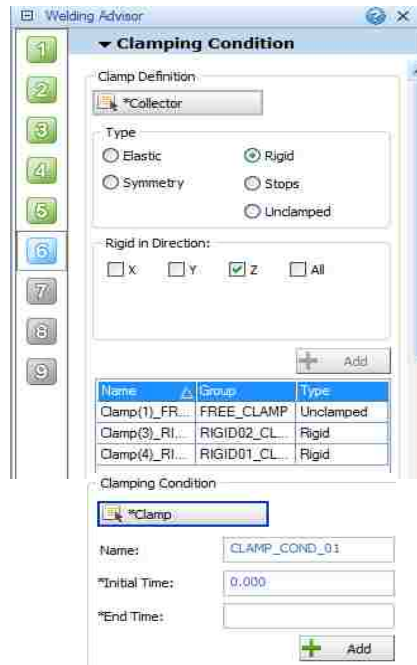


Figure 8.8-Example of Clamping Condition (Step 6)

Step 7 focuses Loads and deformations, whereas Step 8 defines the contact definition. Details are reported in

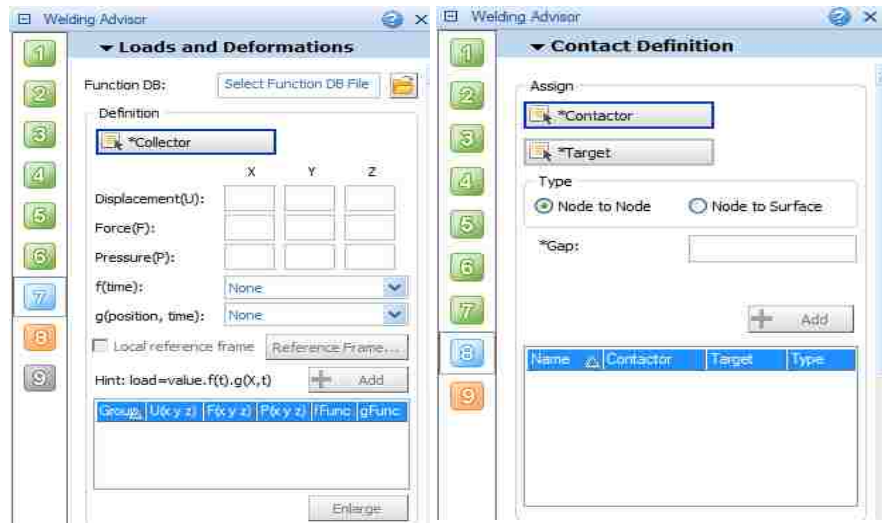


Figure 8.9-Example of Step 7 and Step 8

In this Step 8, ambient condition is defined and also the type of solution. It is possible to choose just a Thermo-Metallurgical analysis or the coupling between Thermo-Metallurgical analysis and mechanical analysis. Advanced solution parameters can be added in order to specify the desired post-processing files and the disk spaced as shown in the following Figure 8.10.

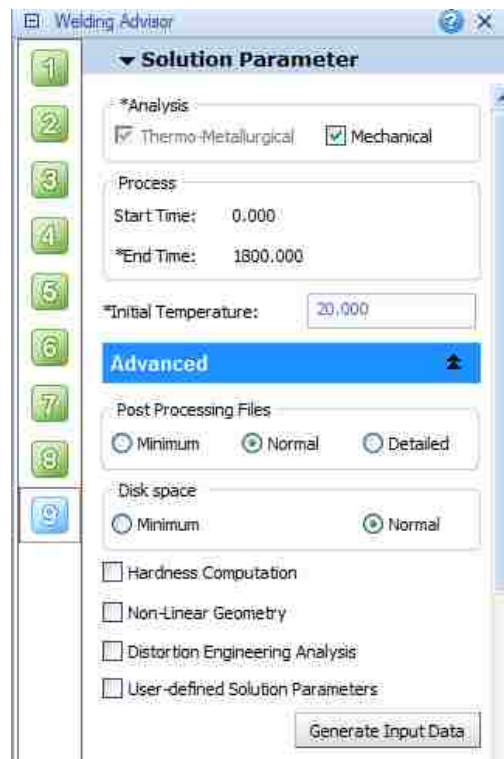


Figure 8.10-Example of Solution Parameter (Step 9)

### **Post-Processing with Visual-Viewer**

As soon as the simulation ends new result files are created and they contain the thermal and mechanical results. With the use of Visual-Viewer is possible to interpret the results with different types of contours and with the use of curves. For example the user can choose between different types of results such as displacement, phase proportion, strain, yield stress, Von Mises stress and so on, as described in Figure 8.11.

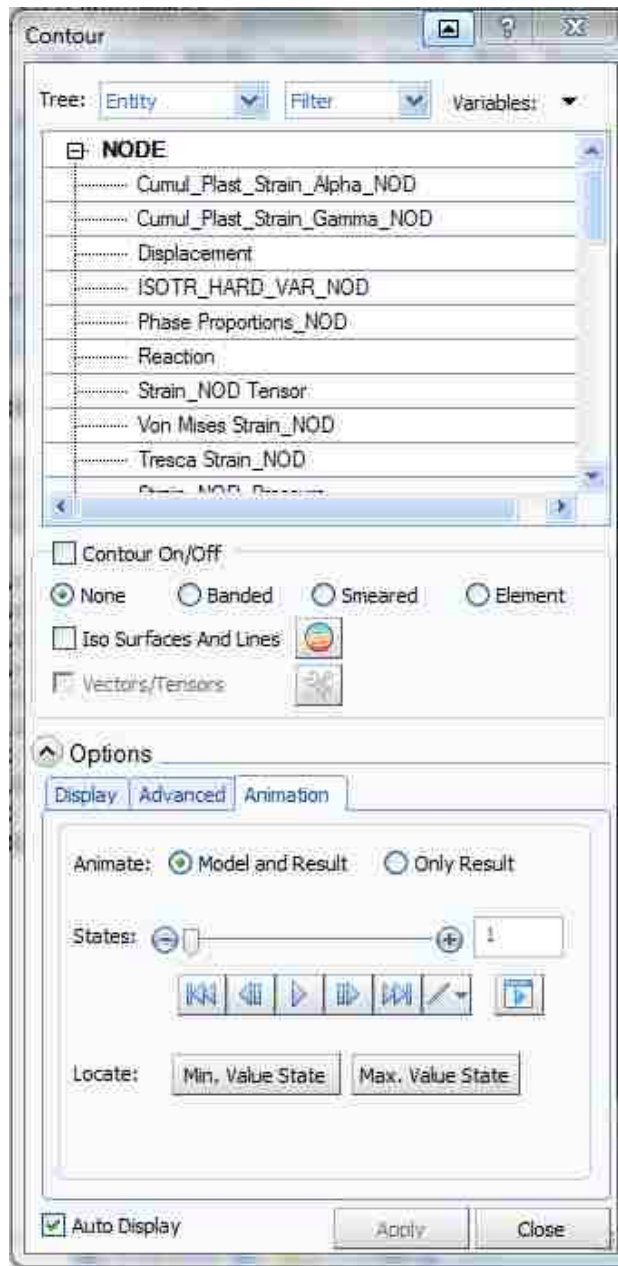


Figure 8.11-Contours definition

## Appendix B - A guide to welding process in WELD PLANNER

Weld Planner workflow is introduced in the following Figure 8.12.

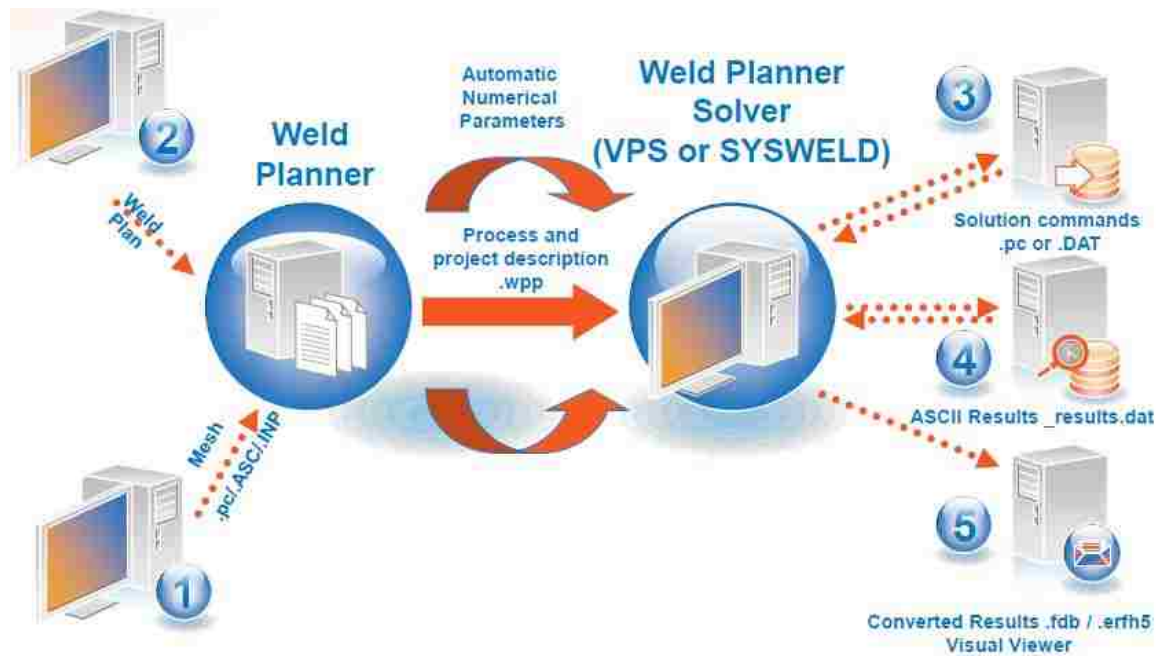


Figure 8.12-Weld Planner workflow [60]

The WELD PLANNER workflow is divided into the following steps:

1. Preparation of the geometry;
2. Weld Plan introduction ;
3. Analysis of the results.

### Preparation of the Geometry

In the first step the geometry is built with the use of Visual mesh in the same way introduced in Appendix A. the geometry can be built with shell elements or with hexa elements. In addition it is necessary to specify the collectors for the components, filler material (if present) and the weld path. Once the geometry has been created, a file (*filename\_DATA1000.ASC*) is generated.

### Analyzing and simulation

The file (*filename\_DATA\*.ASC*) generated in the previous step is then imported into WELD PLANNER. All the materials of the components and their relative thickness need to be assigned from a dedicated list already present in the software as shown in Figure 8.13.

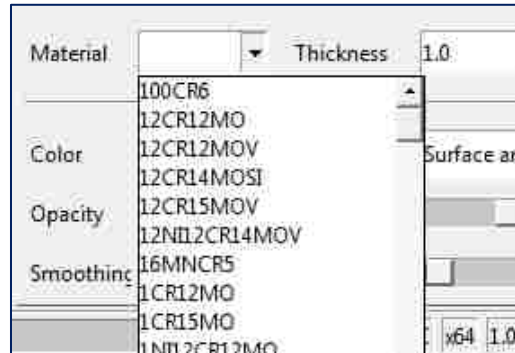


Figure 8.13-Example of material database in Weld Planner

It is necessary to specify for each collector the object type, in case of the joint the object type is the “Welds”. Moreover, the user has to specify the weld technique and the bead width (equal to half of the total bead width) as shown in Figure 8.14.

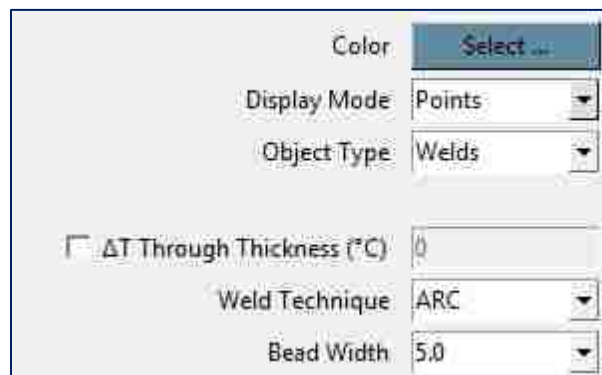


Figure 8.14-Example of weld parameters in Weld Planner

By clicking on one of the clamp collector previously created, it is possible to define the right parameters for each clamp such as the directions of movement to be blocked. Moreover, the user can also define the clamp to be applied to initial geometry or applied to deformed geometry. By default the clamping condition will be applied to deformed geometry.

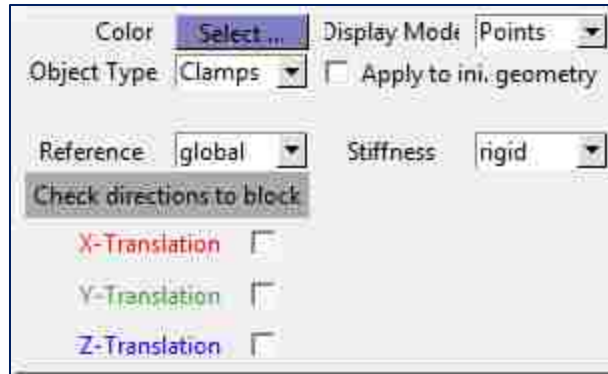


Figure 8.15-Example of clamping definition in Weld Planner

By clicking in “Process Definition”, the weld plan can be defined and a step can be assigned to each weld and clamp. An example of a Weld Plan is shown in the following Figure 8.16.

		Steps		
		1	2	3
Objects		c	#	
			1	0
			0	0
	JOINT_01	1		
	CLAMP_01	1		
	CLAMP_02	2		
	CLAMP_03	2		
	CLAMP_04	2		

Figure 8.16-Example of weld plan definition in Weld Planner

In Weld Planner two types of simulation can be performed: linear geometry and non-linear geometry. The linear geometry should be used for small displacements. The non-linear geometry is an option for large displacements, rotations and stress stiffening. Moreover it is slower because each load has to be divided in at least 4 other steps and this causes an increase in computational time against the linear geometry analysis. As soon as the computation option (linear geometry and non-linear geometry) is defined, it is possible to generate the input file for the solution. After the simulation two results files are generated: *filename.dat* and *filename\_RESULT.erfh5*.

### Analysis of the results

The post-processing can be performed both with Weld Planner and Visual-Viewer. The file *filename.dat* can be loaded directly in WELD PLANNER for a preliminary analysis.



In WELD PLANNER it is possible to apply the final deformed geometry with a customized magnification as shown in the following Figure 8.17.

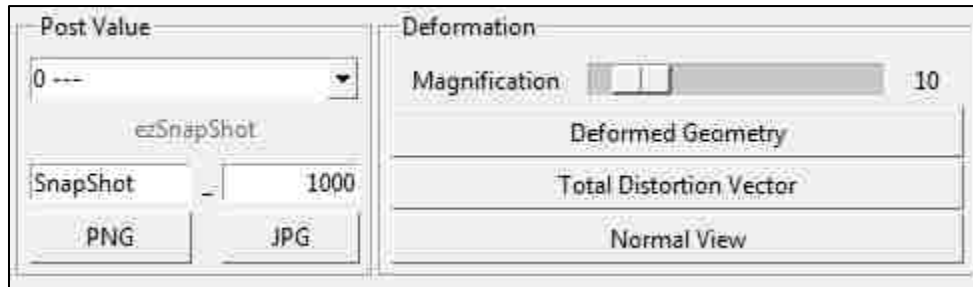


**Figure 8.17- Result analysis panel in Weld Planner**

In addition, the file *filename\_RESULT.erfh5* can be imported in Visual-Viewer for a more detailed analysis (see Appendix A for more details about post-processing in Visual-Viewer).

## Appendix C- Wire filler properties

The following tables describe the properties of the welded joints used for the T-joint tests fabCOR F6 as provided by the manufacturer. Due to the varying levels of dilution with single or multipass, and due to the effect of shielding gas on characteristics that can affect the dilution, there is no chemical specification for the wire.

Weld	Shielding Gas	UTS (ksi)	YS (ksi)	% Elong.	CVN @ -4°F (ft-lbs)	CVN @ -40°F (ft-lbs)
1	75% Ar/ 25% CO <sub>2</sub>	106.4	94.5	20.2	38, 42, 48, 42, 48 (44 avg.)	28, 32, 30, 28, 35 31
2	90% Ar/ 10% CO <sub>2</sub>	106.5	96.5	22.8	38, 40, 43, 48, 47 (45 avg.)	40, 37, 33, 31, 37 (36 avg.)

	C	Mn	Si	P	S	Cu	Cr	Ni	Al	Ti
75% Ar/ 25% CO <sub>2</sub>	0.13	1.65	0.92	0.008	0.020	0.07	0.07	0.03	0.03	0.03
90% Ar/ 10% CO <sub>2</sub>	0.11	1.62	0.75	0.007	0.014	0.06	0.05	0.03	0.009	0.03

## REFERENCES

- [1] W. Perret, R. Thater, U. Alber, C. Schwenk and M. Rethmeier, "Approach to asses a fast welding simulation in an industrial enviroment-Application for an automotive welded part," *International Journal of Automotive Technology*, vol. 12, no. 6, pp. 895-901, 2011.
- [2] Simula, "www.3ds.com," April 2013. [Online]. Available: <http://www.3ds.com/fileadmin/PRODUCTS/SIMULIA/PDF/tech-briefs/cross-multi-pass-pipe-welding-analysis-abaqus-welding-interface-13.pdf>. [Accessed 24 01 2014].
- [3] A. R. Kohandehghan and S. Serajzadeh, "Arc welding induced residual stress in butt-joints of thin plates under constraints," *Journal of manufacturing processes*, vol. 13, pp. 96-103, 2011.
- [4] H. Long, D. Gery, A. Carlier and P. Maropoulos, "Prediction of welding distortion in butt joint of thin plates," *Material and Design*, vol. 30, pp. 4126-4135, 2009.
- [5] P. Michaleris and A. DeBiccari, "http://www.me.psu.edu/," [Online]. Available: <http://www.me.psu.edu/michaleris/Pubs/wj97a.pdf>. [Accessed 14 03 2014].
- [6] M. Shubert, F. Pandheeradi, F. Arnold and C. Habura, "http://www.simulia.com/," 2010. [Online]. [Accessed 14 3 2014].
- [7] C. Simion, C. Manu, S. Baset and J. Milliard, "www.ansys.com," [Online]. Available: <http://www.ansys.com/staticassets/ANSYS/staticassets/resourcelibrary/confpaper/2006-Int-ANSYS-Conf-335.pdf>. [Accessed 24 01 2014].
- [8] W.-f. Zhu, C. Xu and L. Zeng, "Couple finite element analysis of MIG welding assembly on auto-body hohg-strength steel panel and door hinge," *Int J Adv Manuf Technol*, vol. 51, pp. 551-559, 2010.
- [9] I. Sattari-Far and Y. Javadi, "Influence of welding sequence on welding distortions in pipes," *Internaltional Journal of Pressure Vessels and Piping*, vol. 85, pp. 265-274, 2008.
- [10] J. Goldak and M. Asadi, "Challenges in Validation of Computational Weld Mechanics Code to Compute Residual Stress and Distortion in Welds," *Journal of*

*Pressure Vessel Technology*, vol. 136, pp. 011201-1-7, 2013.

- [11] K. Masabuchi, Analysis of welded structures, Pergamone press, 1980.
- [12] K. Jackson and R. Darlington, "Advanced Engineering Methods for Assessing Welding Distortion in Aero-Engine Assemblies," *Trends in Aerospace Manufacturing 2009 International conference*, 2009.
- [13] E. G. SYSWELD,  
"http://www.elitecrown.com.tw/down.php?url=upload/2011/01/20110119105209.pdf," Engineerign simulation Solution for heat treatment, welding and welding assembly. [Online]. [Accessed 24 02 2014].
- [14] E. Feulvarch, V. Robin and M. Bergheau, "Thermometallurgical and mechanical modeling of welding-application to multipass dissimilar metal girth welds," *Science and Technology of Welding and Joining*, vol. 16, no. 3, pp. 221-226, 2011.
- [15] N. Nazemi, F. Ghrib and J. Sokolowski, "The HAZ in Aluminum Welding Revisited," *3rd spciality conference on Engineering Mechanics and Materials*, 2013.
- [16] C. Heinze, C. Schwenk and M. Rethmeier, "Effect of heat source configuration on the result quality of numerical calculation of welding-induced distortion," *Simulation Modelling Prectice and Theory*, vol. 20, pp. 112-123, 2012.
- [17] R. N. Lidam, Y. H. Manurung, E. Haruman, M. Redza, M. R. Rahim, M. S. Sulaiman, M. Zakaria, G. Tham, S. Abas and C. Y. Chau, "Angulur distortion analysis of the multipass welding process on combined joint types using thermo-elastic-plastic FEM with experiemental validation," *Int J Adv Manuf Technol*, vol. 69, pp. 2373-2386, 2013.
- [18] T. PadmaKumari and S. VenkataSairam, "Finite Element Analysis of EBW welded joint using SYSWELD," *International Journal of Emerging Technology and Advances Engineering*, vol. 3, no. 2, pp. 335-340, 2013.
- [19] A. Bachorski, M. Painter, A. Smailes and M. Wahab, "Finite element prediction of distortion during ga metal arc welding using the shrinkage of volume approach," *Journal of materials processing technology*, pp. 405-409, 1999.
- [20] E. GROUP, "www.esi-group.com," Virtual welding & assembly suite 2012, 2012. [Online]. [Accessed 20 02 2014].

- [21] M. S. Sulaiman, Y. H. Manurung, E. Haruman, M. R. A. Rahim, M. R. Redza, R. N. A. Lidam, S. K. Abas, G. Tham and C. Y. Chau, "Simulation and experimental study on distortion of butt and T-joints using WELD PLANNER," *Journal of Mechanical Science and Technology*, vol. 25, no. 10, pp. 2641-2646, 2011.
- [22] Y. Duan, Y. Vincent, F. Boitout, J. Leblond and J. Bergheau, "Prediction of welding residual distortions of large structures using a local/global approach," *Journal of Mechanical Science and Technology*, vol. 21, pp. 1700-1706, 2007.
- [23] J. A. Goldak and M. Asadi, "Combinatorial optimization of weld sequence by using a surrogate model to mitigate a weld distortion," *Int J Mech Mater Des.*, vol. 7, pp. 123-129, 2011.
- [24] J. E. R. Dhas and S. Kumanan, "Weld residual stress prediction using artificial neural network and Fuzzy logic modeling," *Indian Journal of Engineering & Materials Science*, vol. 18, pp. 351-360, 2011.
- [25] L. Tian, Y. Luo, Y. Wang and X. Wu, "Prediction of transverse and angular distortions of gas tungsten arc bead-on-plate welding using artificial neural network," *material and design*, vol. 54, pp. 458-472, 2014.
- [26] O. Benyounis. [Online]. Available: [http://doras.dcu.ie/17608/1/Final\\_Version,\\_Review\\_paper.pdf](http://doras.dcu.ie/17608/1/Final_Version,_Review_paper.pdf). [Accessed 24 01 2014].
- [27] W. Spraragen, "Shrinkage distortion in welding," *Welding journal*, vol. 29, no. 6-7, pp. 292s-294s 323s-335s, 1950.
- [28] D. White, "Residual stresses in large stiffed tubular structures," *CUED Report*, Vols. C-Struct/TR67, 1978.
- [29] Verhaeghe, Predictive formulae for weld distortion- a critical review, United Kingdom: Woodhead Publishing Ltd, 1999.
- [30] R. Heuss, N. Müller, W. van Sintern, A. Starke and A. Tschiesner, "www.mckinsey.com," 02 2012. [Online]. Available: <http://www.mckinsey.com/Search.aspx?q=lightweight%2C%20heavy%20impact%20->. [Accessed 10 02 2014].
- [31] T. Huang, P. Dong, L. A. Decan and D. D. Harwing, "Residual stresses and distortions in lightweight ship panel structures," *Technol. Rev. J.*, vol. 11, pp. 1-26,

2003.

- [32] E. Group, "www.esi-group.com," Fall 208. [Online]. Available: <http://www.esi-group.com/sites/default/files/resource/other/805/pt36-final.pdf>. [Accessed 10 02 2014].
- [33] Liu, Methodologies study and corresponding software development for knowledge-driven auto-body structure design., Jilin, China: Doctoral dissertation of Jilin University, 2007.
- [34] N. Mandal, Welding and distortion control, Pangbourne: Narosa Publishing House, 2004.
- [35] M. Groover, Fundamentals of modern manufacturing-Material, Process and Systems, John Wiley & Sons, Inc., 4th edition-2010.
- [36] "lincolnelectric," [Online]. Available: <http://www.lincolnelectric.com/en-us/support/process-and-theory/pages/arc-welding-detail.aspx>. [Accessed 1 2 2014].
- [37] American Welding Society, Welding Handbook-Part 1-Volume 2, American Welding Society, Ninth edition.
- [38] L. Jeffus, Welding Principles and Applications, Delmar Publishers Inc, 2011.
- [39] J. A. Goldak and M. Akhalaghi, Computational welding mechanism, Springer, 2005.
- [40] N. R. Mandal, Welding and distortion control, Alpha science, 2004.
- [41] D. Rosenthal, "The theory of moving sources of heat and its application to metal treatments," *ASME*, vol. 68, pp. 849-89, 1946.
- [42] W. F. Hess, L. L. Merrill, E. F. Nippes and A. P. Bunk, "The Measurement of Cooling Rates Associated with Arc Welding and Their Application to the Selection of Optimum Welding Conditions," *Welding Journal*, vol. 22, no. 9, pp. 377s-422s, 1943.
- [43] V. Pavelic, R. Tanbakuchi, O. Uyehara and P. Myers, "Experimental and computed temperature histories in gas tungsten arc welding of thin plates," *Welding Journal Research Supplement.*, vol. 48, pp. 295s-305s, 1969.
- [44] J. Godak, A. Chakravarti and M. Bibby, "A finite element model for welding heat sources," *Metallurgical Transactions*, vol. 15B, no. 2, pp. 299-305, 1984.

- [45] M. M. Rathore and R. R. Kapuno, Engineering heat transfer, Jones & Barlett Learning, 2nd edition-2011.
- [46] D. Deng and S. Kiyoshima, "FEM analysis of residual stress distribution near weld start/end location in thick plates," *Computational Materials Science*, vol. 50, pp. 2459-2469, 2011.
- [47] X. Zhu and Y. Chao, "Effects of temperature dependent material properties on welding simulation," *Computer & Structures*, vol. 80, no. 11, pp. 967-976, 2002.
- [48] F. Boitout, D. Dry, Y. Goroochurn, P. Mourgue and H. Porzner, "Transient Simulation of Welding Processes. Thermal ,metallurgical and Structural Model. 'The welding simulation solution'," ESI GROUP, 2012.
- [49] W. D. Callister, Materials Science and Engineering- An introduction, United States of America: John Wiley & Sons, 2007.
- [50] K. Easterling, Introduction to the physical metallurgy of welding, 1992.
- [51] W. s. service, "www.wilhelmsen.com," [Online]. Available: [http://www.wilhelmsen.com/services/maritime/companies/buss/BUSS\\_Pressroom/Documents/Hydrogen%20cracking.pdf](http://www.wilhelmsen.com/services/maritime/companies/buss/BUSS_Pressroom/Documents/Hydrogen%20cracking.pdf). [Accessed 23 6 2014].
- [52] A. Pahkamaa and J. Pavasson, *A new welding method approach in simulation driven design*, Lulea University of technology, 2009.
- [53] A. Lundback, *Finite element modelling and Simulation of Welding of Aerospace Components*, Sweden: Lulea University of technology, 2003.
- [54] L.-E. Lindgren, H. Runnemalm and M. O. Näsström, "Simulation of multipass welding of a thick plate," *International Journal for Numerical Methods in Engineering*, vol. 44, no. 9, pp. 1301-1316, 1999.
- [55] K. Ogawa, D. Deng, S. Kiyoshima, N. Yanagida and K. Saito, "Investigations on welding residual stresses in penetration nozzles by means of 3D thermal elastic plastic FEM and experiment," *Computational Materials Science*, vol. 45, pp. 1031-1042, 2009.
- [56] N. Instrument, "National Instrument," 28 10 2013. [Online]. Available: <http://www.ni.com/white-paper/3642/en/>. [Accessed 12 12 2013].
- [57] A. international, "<http://www.astm.org/>," [Online]. Available:

- <http://www.astm.org/Standards/A572.htm>. [Accessed 17 06 2014].
- [58] ASM, "<http://www.asminternational.org/>," 2012. [Online]. Available: <http://products.asminternational.org.ezproxy.uwindsor.ca/hbk/index.jsp>. [Accessed 17 06 2014].
- [59] E. GROUP, *VISULA WELD v6.5 training presentation*, ESI GROUP, 2010.
- [60] E. GROUP, *Welding distortion simulation with Weld Planner*, ESI GROUP, 2013.
- [61] T. Schenk, *Modelling welding distortion-Influence of clamping and sequencing*, Freiburg, Germany: Albert-Ludwig-Universität , 2011.
- [62] E. Group, "[www.esi-group.com](http://www.esi-group.com/)," Fall 2008. [Online]. Available: <http://www.esi-group.com/sites/default/files/resource/other/805/pt36-final.pdf>. [Accessed 10 02 2014].



## VITA AUCTORIS

NAME: Francesca Folchi

PLACE OF BIRTH: Lanciano, Chieti, Italy

YEAR OF BIRTH: 1990

EDUCATION: Politecnico di Torino, B.Sc. in Automotive Engineering, Torino, Piemonte, Italy, 2009

Politecnico di Torino, MAS – Automotive Engineering, Torino, Piemonte, Italy, 2014

University of Windsor, MAS - Mechanical Engineering, Windsor, ON, Canada, 2014.